PHYSICS AND NUMERICS OF SPRAY ATOMIZATION SIMULATIONS

By

Arpit Agarwal

A dissertation submitted in partial fulfillment of
the requirements for the degree of

Doctor of Philosophy
(Mechanical Engineering)

at the

UNIVERSITY OF WISCONSIN - MADISON

2020

Date of final oral examination: 07/17/2020

The dissertation is approved by the following members of the Final Oral Committee:
Mario Trujillo (Thesis Advisor), Associate Professor, Mechanical Engineering
Riccardo Bonazza, Professor, Engineering Physics
Tom Krupenkin, Associate Professor, Mechanical Engineering
Alejandro Roldán-Alzate, Assistant Professor, Mechanical Engineering
Shiva Rudraraju, Assistant Professor, Mechanical Engineering

© Copyright by Arpit Agarwal 2020

All rights reserved.

Acknowledgements

I would like to thank Professor Trujillo for his thorough guidance over the duration of my Ph.D. This work would not have been possible without his guidance. His inputs have been pivotal in shaping this work.

I would also like to thank my thesis committee members, Professor Bonazza, Professor Krupenkin, Professor Roldán-Alzate, and Professor Rudraraju for making the time to serve on my committee and for providing valuable feedback.

My thanks are also due to Direct-injection Engine Research Consortium (DERC) for providing consistent support for our work. I would also like to thank the Center for High Throughput Computing (CHTC) for providing the computational resources, which have enabled much of this work. I would also like to sincerely thank Joshua Leach for providing all the computational support required in my work. He made working with all the computational resources very stress-free. The Engine Research Center (ERC) and the Department of Mechanical Engineering have also been very helpful throughout the course of my degree.

I have benefited greatly from my time in Madison and in graduate school. This would not have been possible without my lab members and my friends in Madison. My friends outside of Madison have also played a big part in supporting me through this journey. I would like to thank them as well.

My parents and my family have made countless sacrifices to make me the person I am today. They have provided me all the support I need through my life and I cannot thank them enough.

Preface

This thesis broadly describes work that has been published in the form of two journal publications and some work that is yet to be published. I have also been involved in some collaborative work in the research group where I was not the lead researcher. This work has not been included in this thesis but is listed here.

Here I summarize contributions by other researchers to the work done over my Ph.D.:

1. **Publication 1**: Arpit Agarwal, and Mario F. Trujillo. "A closer look at linear stability theory in modeling spray atomization." International Journal of Multiphase Flow (2018) [3]

   This work forms a majority of Chapter 1 of this thesis. Contributions from group members:

   (a) Code for processing intact liquid core length: This code has been written and edited by Suraj Deshpande, Lakshman Anumolu, Soumil Gurjar, Michael Mason and Chia-Wei Kuo

   (b) Code for semi-analytical solution of linear stability problem: This solver has been written by Suraj Deshpande

2. **Publication 2**: Arpit Agarwal, and Mario F. Trujillo. "The effect of nozzle internal flow on spray atomization." International Journal of Engine Research (2020) [4]

   This work forms a majority of Chapter 2 of this thesis. Contributions from group members:

   (a) Code for processing intact liquid core length: This code has been written and edited by Suraj Deshpande, Lakshman Anumolu, Soumil Gurjar, Michael Mason and Chia-Wei Kuo

   Much of the work presented in Chapter 1 and Chapter 2 of this thesis has been written along with Professor Mario F. Trujillo.

3. **Publication under preparation**: "Evaluating Surface Tension Schemes with Respect to High-Fidelity Atomization Simulations." (Chapter 3)
   (a) The code for constructing interface from liquid fraction fields was developed by Douglas Ryddner [60] (and modified later by Michael Mason). This code forms an integral part of the solver developed here.
   (b) Code for processing intact liquid core length: This code has been written and edited by Suraj Deshpande, Lakshman Anumolu, Soumil Gurjar, Michael Mason and Chia-Wei Kuo
   (c) Code for semi-analytical solution of linear stability problem: This solver has been written by Suraj Deshpande
   (d) Code for generating initial fields in the shear-layer problem: This solver has been written by Suraj Deshpande
   (e) Some case setup files have been provided by Soumil Gurjar, Suraj Deshpande and Raunak Bardia

4. **Publication 3 (not part of thesis)**: Mario F. Trujillo, Soumil Gurjar, Michael Mason, and Arpit Agarwal. "Global characterization of the spray formation process." Atomization and Sprays (2018) [69]

   Most of the work in this publication was performed by the other authors, I assisted in running some cases and performing some analysis, I also provided some figures and participated in discussions that shaped the work.

Abstract

Liquid sprays appear in a wide range of engineering systems, for example internal combustion engines, irrigation sprays, printing, food processing and others. The spray formation process, i.e., the process that converts the injected liquid into a cloud of fine droplets, is also known as atomization. This process is a multi-dimensional, multi-scale, turbulent process, with complex topology of the interface.

Fully resolved atomization computations are challenging and computationally expensive. Therefore, most engineering studies, where this process is completely unresolved, depend on lower-order models to describe relevant physics. In the present study, however, we leverage accurate numerical methods along with high spatio-temporal resolution simulations to revisit atomization theory. High fidelity simulations of atomization have only recently become feasible. We have access to spatially resolved data about the liquid and gas distribution along with the velocity field. We are using this data towards developing a better understanding of the atomization mechanisms. A better understanding of the underlying physics ultimately leads to better engineering models.

We also investigate the numerical methods themselves, specifically the surface tension computation. Accurate representation of surface tension depends on the accurate computation of local curvature. This continues to a weakness in the popular simulation methods. This work tries to identify promising curvature schemes in the context of complex flow problems.

The current work is presented as three chapters of this document:

1. A closer look at linear stability theory in primary atomization modeling

In Chapter 1 we look at dominant breakup models. These models are based in the idea that interfacial instability leads to the primary atomization. Here, the underlying assumptions in this theory are outlined and the extent of their validity is established. It is then examined whether these most violent perturbations are actually responsible for the fragmentation of the jet or if there is

some other mechanism leading to the breakup.

A main finding from the work shows that while the most unstable modes are captured in the simulations and agree with theoretical predictions which inform the present models, these modes are *not* directly responsible for fragmenting the liquid core or causing primary atomization. Their action is limited to breaking up the surface of the jet, while the liquid core of the jet remains intact for another 20 jet diameters downstream.

2. Effect of internal nozzle flow on primary atomization

In Chapter 2 we study the physics of internal nozzle flow. The focus is the effect of nozzle asymmetries and imperfections on primary atomization. This is done by adopting three representative geometries, namely two scans of a real injector nozzle, and a canonical configuration with purely external flow.

We find that primary atomization is sensitive to internal nozzle flow; small changes to the nozzle geometry ($O(1\mu\text{m})$) affect bulk atomization characteristics ($O(1000\mu\text{m})$). Here we explore the underlying mechanism for the same. We find that in spite of more pronounced atomization for the rougher geometry, the magnitude of the turbulent liquid kinetic energy is roughly the same as the smoother geometry. This highlights the important role of mean field quantities, in particular, non-axial velocity components, in precipitating primary atomization.

3. Evaluating Surface Tension Schemes with Respect to High-Fidelity Atomization Simulations

In complex multi-phase flows like atomization, surface tension is expected to play a vital role in some of the dynamics. Accurate representation of the surface tension force is challenging as it directly tied to the accuracy of the interface curvature calculation. In Chapter 3, we consider two aspects, first we analyze three different curvature computation schemes for two phase flow simulations, and then we evaluate the level of influence these differences in the numerical schemes have on problems

of practical interest.

The differences in the accuracy of the three methods is first analyzed through simpler static and dynamic test cases that are common in numerical methods literature. We find that the signed distance based computation of curvature performs significantly better in these test problems. However, this difference plays a small role in more complex simulations like the retraction of a liquid column. A key finding here is that increasing complexity of the curvature scheme may only lead to marginally better performance in realistic flow problems.

Contents

List of Figures

List of Tables

Chapter 1

Linear Stability Theory in Primary Breakup Modeling

1.1 Background & Motivation

Primary atomization in sprays, defined as the complete fragmentation of a liquid jet, has been the subject of a large number of research efforts [27, 41, 42] due in part to its practical relevance in fuel injection [58]. Apart from some recent DNS-type studies [7, 21, 31, 39, 65–67] that resolve and sharply capture the liquid-gas interface, atomization computations have relied on models to describe relevant physics. Among the most widely used treatment of sprays is the Lagrangian-Eulerian (LE) modeling approach, which is employed extensively in applications such as internal combustion engines, environmental spraying, printing, food processing, and various others. Since the atomization process is completely under-resolved in this approach, the near nozzle liquid field is described using breakup models.

A common procedure for developing breakup models is based on the linear stability theory [10, 57]. Its combination with the LE approach has continued to dominate spray modeling for the last 20-30 years [2, 14, 16, 36, 46, 68, 74, 77]. This is partly due to the ease of integration with other relevant models describing drop-drop collision, wall impingement, vaporization, and other droplet phenomena. The popularity of linear-theory-based breakup models, simply referred to as breakup models hereafter, has grown beyond academic research as they have been incorporated into commercial engine CFD codes including CONVERGE CFD, STAR-CD, and AVL-FIRE.

In the derivation of these breakup models, perturbations on the liquid jet are interpreted to develop under the action of the Kelvin-Helmholtz (KH) instability. Growth of KH-unstable surface waves is assumed to cause liquid to break off, and cause fragmentation of the liquid jet. Computationally, the liquid jet is initially treated as Lagrangian blobs. Formation of new drops and changes in their diameter are determined through numerical solutions of linearized stability equations (KH and/or Rayleigh-Taylor instabilities), along with modeling constants. Lin and Reitz [42] provide qualitative commentary on the success and shortcomings of linear theory used in jet breakup descriptions, and call attention to the significance of internal nozzle flow on surface instability. High resolution (spatial and temporal) flow descriptions are required for studying these effects, which were not computationally feasible until recently.

The present chapter is composed of three initiatives. First, we are interested in investigating the extent of the validity of the underlying linear stability assumptions using highly-resolved simulations based on an algebraic Volume of Fluid (VoF) [20] methodology. Explicitly, in a linearized analysis of liquid injection, the velocity perturbations are assumed to be small, the base velocity is assumed to be completely axial and fully developed, and the liquid surface is described by a superposition of sinusoidal modes. To the best of our knowledge, no such quantitative analysis of the models' assumptions has been conducted to date. The second initiative is estimating whether the most unstable modes originating from the linear regime and calculated via Orr-Sommerfeld agree with the more detailed VoF simulations. And for the third initiative, it is examined whether these most violent perturbations are actually responsible for the fragmentation of the jet. This is a more fundamental question, since depending on the results, it can confirm or call to question the applicability of existing approaches for modeling breakup or atomization. To accurately capture the effects of nozzle imperfections and surface roughness, the Engine Combustion Network's[1] (ECN) Spray A nozzle configuration is employed with a fine, boundary-fitted grid. This is in contrast to external-only simulations [21, 39, 65–67] and simulations with idealistic inflow conditions [31].

The chapter is organized as follows. In Section 1.2, a description of the VoF methodology employed is given. Section 1.3 describes the flow setup used in this work. The nozzle geometries are examined in detail in Section 1.4. The computational methodology is validated in Section 1.5 against X-ray radiography measurements. In Section 1.6, the derivation of the linearized system that forms the basis of the breakup models is summarized and the assumptions in the theory are formally introduced. The results are then presented in Section 1.7 beginning with the analysis of the extent of the linear region, the comparison of linear stability theory with VoF simulations, and the implications for primary atomization. The findings of this part of the work and some concluding thoughts are discussed in Section 1.8.

1.2 Numerical Method

The Volume-of-Fluid (VoF) simulations reported in this paper are performed with an algebraic solver, `interFoam`, which is based on a compressive interface capturing methodology advanced by Ubbink & Issa [70] and Rusche [59] with contributions from Henry Weller. `interFoam` is part of a larger open-source distribution of computational mechanics solvers and C++ libraries of OpenFOAM®[2]. The solver is based on a finite volume discretization on collocated grids for the solution of two-phase incompressible flows. A thorough evaluation of solver performance with respect to a broad range of two-phase flows is reported by Deshpande et al. [20]. The evaluation was based on the performance with respect to kinematics of advection, dynamics in inertia dominated regime, and dynamics in the surface tension dominated regime. An abbreviated description is provided here; a more detailed explanation can be found in Ref. [20].

---

[1] `https://ecn.sandia.gov/`

[2] `http://www.openfoam.com`

The first part of the solution consists of advancing the liquid fraction field, α, by solving the following conservation equation,

$$\frac{\partial \alpha}{\partial t} + \nabla \cdot (\tilde{\mathbf{U}} \alpha) = 0, \tag{1.1}$$

where $\tilde{\mathbf{U}}$ is the velocity field. The liquid fraction represents the volume fraction of liquid occupying a given computational cell, Ω_i, $i \in [1, N_{cells}]$. The discrete version of this equation is

$$\frac{\alpha^{n+1} - \alpha^n}{\Delta t} + \frac{1}{|\Omega_i|} \sum_{f \in \partial \Omega_i} (F_u + \lambda_M F_c) = 0, \tag{1.2}$$

where the fluxes are defined as

$$F_u = \phi_f^n \alpha_{f,\text{upwind}}^n \quad \text{and} \quad F_c = \phi_f^n \alpha_f^n + \phi_{rf}^n \alpha_{rf}^n (1 - \alpha_{rf}^n) - F_u. \tag{1.3}$$

Here n denotes time level, subscript f refers to a cell-face quantity, $\phi_f^n = \tilde{\mathbf{U}}_f^n \cdot \mathbf{S}_f$, and $\mathbf{S}_f$ is the outward normal vector corresponding to a given cell (not normalized). Since velocity (as well as α) are cell-centered quantities, $\tilde{\mathbf{U}}_f^n$ is obtained by weighted-averaging from cells sharing the given face. In the flux term, F_u, the upwind value for the liquid fraction is denoted by $\alpha_{f,\text{upwind}}^n$. With respect to F_c, α_f^n is determined from the second order vanLeer scheme [73]. The remaining quantities represent the compressive flux, i.e. $\phi_{rf}^n \alpha_{rf}^n (1 - \alpha_{rf}^n)$, where

$$\phi_{rf}^n = \min_{f' \in \Omega_i} \left(\frac{|\phi_{f'}^n|}{|\mathbf{S}_{f'}|}, \tilde{U}_{rf,\max} \right) (\mathbf{n}_f \cdot \mathbf{S}_f), \quad \text{and} \quad \tilde{U}_{rf,\max} = \max_{f \in \Omega} \left[\frac{|\phi_f^n|}{|\mathbf{S}_f|} \right]. \tag{1.4}$$

This compressive flux is used to mitigate the effects of numerical diffusion that would occur as a result of the sharp gradients in α in the interfacial region. Lastly, the variable α_{rf}^n is obtained using the `interfaceCompression` scheme native to OpenFOAM [1, 20]. In numerical tests concerning the advection of a discontinuous profile, such as the α-field, the treatment given above performs noticeably better than TVD schemes with regards to the preservation of the sharpness of the discontinuity.

With respect to momentum, the following equation is solved

$$\frac{\partial \rho \tilde{\mathbf{U}}}{\partial t} + \nabla \cdot (\rho \tilde{\mathbf{U}} \otimes \tilde{\mathbf{U}}) = -\nabla p_d + \left[\nabla \cdot (\mu \nabla \tilde{\mathbf{U}}) + \nabla \tilde{\mathbf{U}} \cdot \nabla \mu \right] - \mathbf{g} \cdot \mathbf{x} \nabla \rho + \int_{\Gamma(t)} \sigma \kappa \delta(\mathbf{x} - \mathbf{x}_s) \mathbf{n} d\Gamma(\mathbf{x}_s), \tag{1.5}$$

where the surface tension coefficient is given by σ, local curvature by κ, the gas-liquid interface by $\Gamma(t)$, the 3D Dirac Delta function by $\delta(\mathbf{x} - \mathbf{x}_s)$, and $\mathbf{x}_s$ is the integration variable over $\Gamma(t)$. The Continuum Surface Tension model [13] is employed, namely

$$\int_{\Gamma \cap \Omega_i} \sigma \kappa \delta(\mathbf{x} - \mathbf{x}_s) \mathbf{n} d\Gamma(\mathbf{x}_s) = \int_{\Omega_i} \sigma \kappa \nabla \alpha dV. \tag{1.6}$$

In the predictor step, the density and viscosity fields are regularized according to

$$\rho = \rho_l \alpha + \rho_g (1 - \alpha) \quad \text{and} \quad \mu = \mu_l \alpha + \mu_g (1 - \alpha). \tag{1.7}$$

The solution of the momentum equation is obtained via a PISO [29] iteration procedure. A predictor velocity is first constructed and then corrected to ensure momentum balance and mass continuity. Explicit formulation of the predictor velocity is a two step process, where first the viscous, advective and temporal terms in the momentum equation are used to generate a cell centered vector field, which is then projected to cell faces using a second order scheme. Contributions from surface tension and gravity terms are then added, concluding the predictor formulation. This procedure enforces a consistent discretization of surface tension and pressure gradient [20, 25].

Within the correction procedure, the pressure contribution is added to the flux of predictor velocity, and mass conservation is invoked to yield a Poisson equation for pressure. The linear system is then solved using a Preconditioned Conjugate Gradient method, with Diagonal Incomplete Cholesky as the preconditioner. In the present work we have used three PISO steps to arrive at predictions for $(\tilde{\mathbf{U}}^{n+1}, pd^{n+1})$.

1.3 Simulation Setup

An overview of the simulation setup, including the nozzle configurations, the external flow domain and the flow conditions is provided here. Three configurations are described in this section, but only the first configuration is used in this chapter, the other two configurations are employed in Chapter 2. However, all three configurations are presented together here to avoid repetition later.

Three different spray configurations are being considered in this thesis as illustrated in Fig. 1.1. The first two configurations (Fig. 1.1a and Fig. 1.1b) employ two variations of the ECN Spray A (serial# 210675) nozzle. It is a single-hole, $90\,\mu$m diameter injector nozzle. The two variations of the nozzle are called ‘Unprocessed Spray A’ and ‘Educated Spray A’ through this study. The difference between the two nozzle variations is minute, and hence not visible at the scale of Fig. 1.1; the differences are discussed in depth in Section 1.4. The third configuration (Fig. 1.1c) is a canonical setup where only external flow from a circular orifice is simulated. This external-only flow configuration is frequently used in fundamental studies of spray atomization [65–67, 69].

In each of these setups the boundaries of the external flow domain (grey and green faces in Fig. 1.1) are treated as being open to a larger atmosphere (inflow and outflow are allowed). The nozzle walls, colored red in Fig. 1.1, are treated as no-slip walls, and the inlet faces, shown in blue with the arrows, are prescribed a uniform and constant inlet velocity.

Details of the computational domain are shown in Fig. 1.2. For the internal flow region, the grid boundaries coincide with the surface file for the nozzle and more importantly the surface imperfections are included in the numerical grid. This implies that their effect is captured in the simulations. For the internal flow region, a hexahedral, boundary-fitted grid is employed. The surface of the internal nozzle grid is examined in detail in Section 1.4. The external flow region is divided into two parts, near the spray axis (region highlighted in Fig. 1.2a) and away from the spray

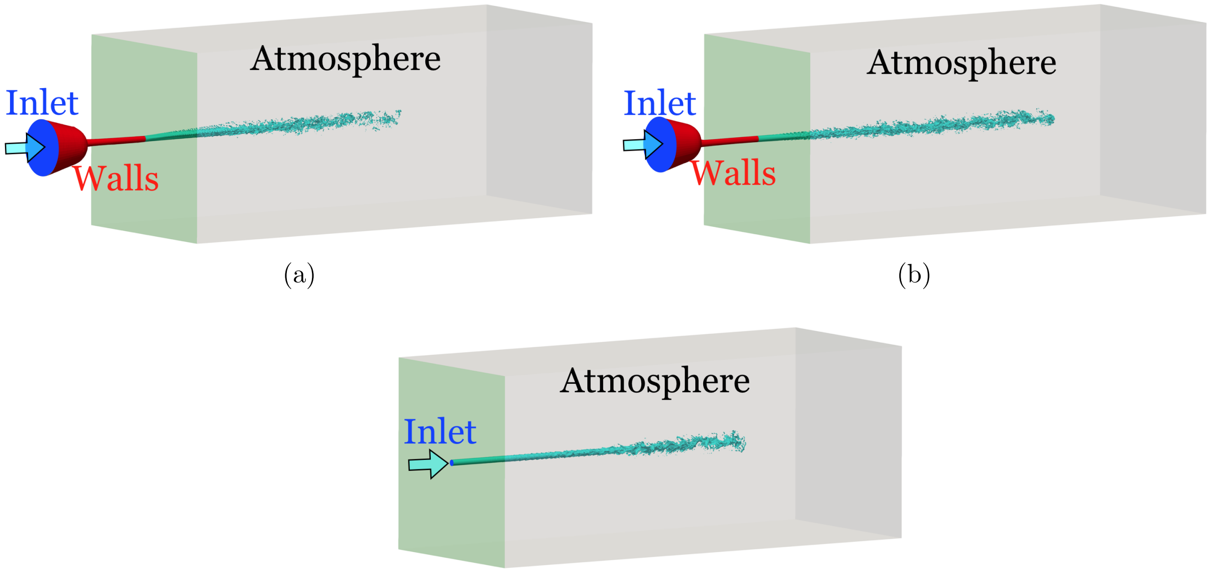

(a)

(b)

(c)

Figure 1.1: Illustrations of the three spray configurations used in this study

axis. A cross section of the near-axis region is shown in Fig. 1.2b. All computational cells within this region are hexahedral as this provides much better numerical performance than tetrahedral cells for the algebraic VoF scheme used here [20]. Away from the spray axis unstructured tetrahedral cells are used that grow larger in size as we move further away from the spray axis to reduce computational cost.

For all of the metrics being reported here, results from three different grid resolutions are considered for each of the three configurations to get an insight into the level of variation with respect to changing grid sizes. Since the grids used here are not uniform due to the boundary fitted geometry, there is a small level of spatial variation in the cell sizes for each of the simulations. The cell-size distribution for the 'Educated Spray A' configuration is displayed in Fig. 1.3 and shows that the cell sizes are closely distributed around their respective mean values. As a representative number for each of the cases we report the average cell size in the near-spray region. The case matrix presented in Table 1.3 shows this average Δx value in the near field region for each of the cases.

In all calculations presented, the x coordinate is aligned with the jet axis as per ECN specifica-

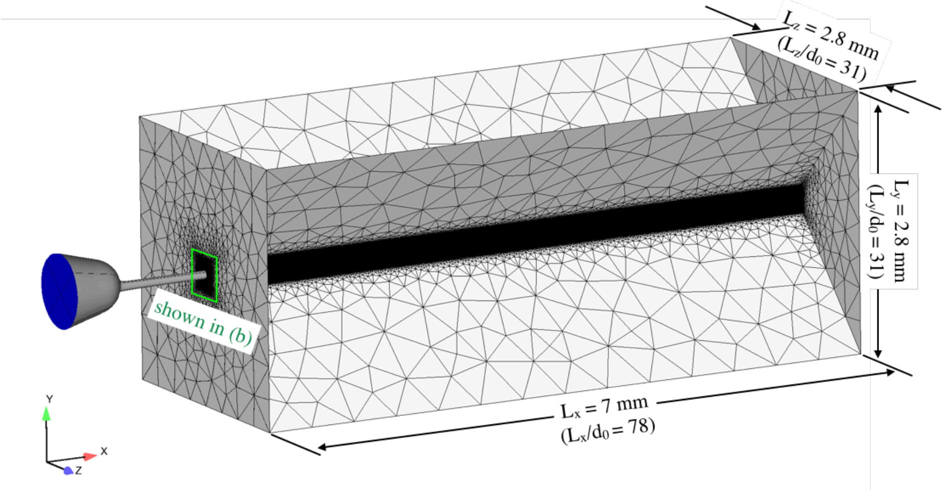

(a)

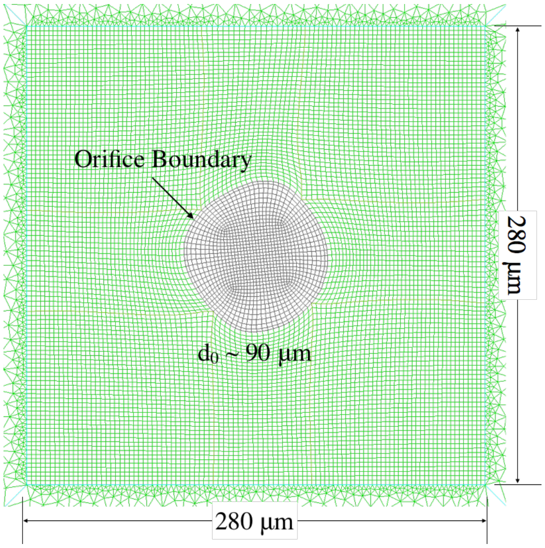

(b)

Figure 1.2: A visualization of the entire domain and grid is shown in (a) with the nozzle included on the left. The plane coinciding with the nozzle orifice is shown in (b), clearly portraying the asymmetry of the orifice.

tions and the origin is placed at the centroid of the orifice opening. The y axis is aligned with the transverse direction and the z axis is aligned with the spanwise direction as depicted in Fig. 1.2.

In Fig. 1.4, a representative result from the simulation is displayed showing the first 40 diameters from the injector nozzle. The nozzle is visible in the top-left corner, with the liquid jet coming out and then disintegrating into ligaments and droplets towards the bottom-right.

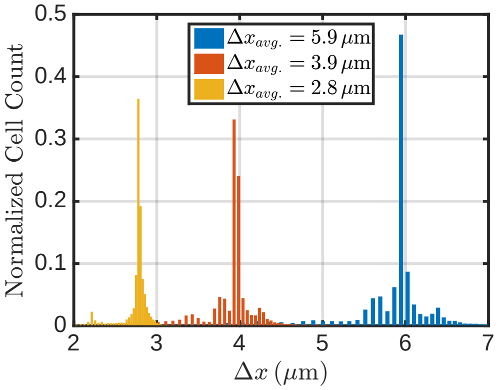

Figure 1.3: The near-field cell-size distribution for the 'Educated Spray A' configuration. Three different grid resolutions are considered here.

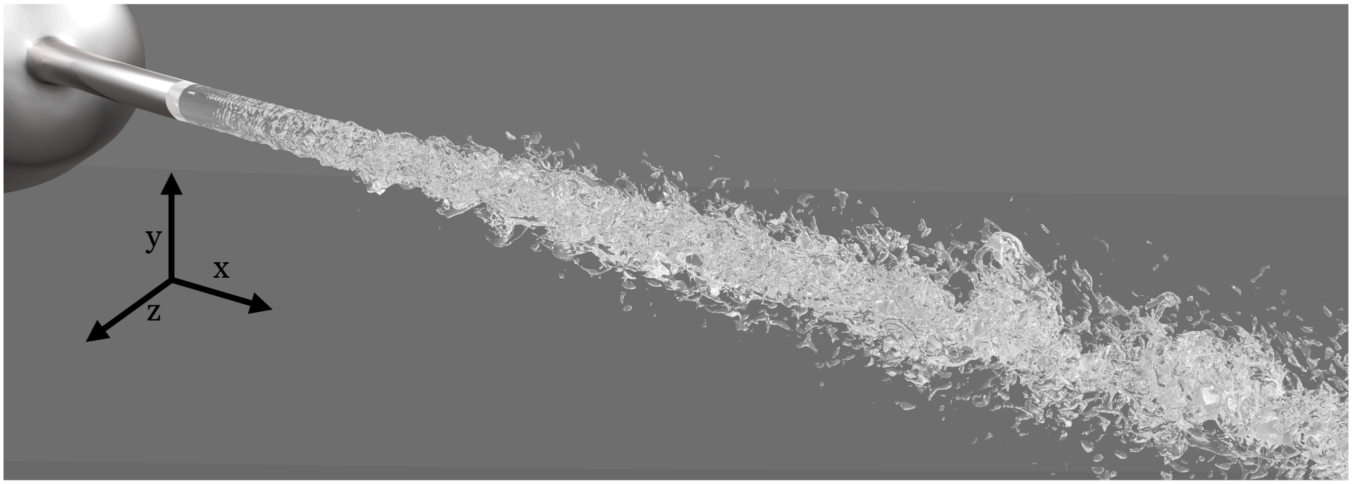

Figure 1.4: Visualization of the jet atomization for a typical simulation using the Spray A geometry.

For this study, all simulations have been performed at experimental conditions reported by [34], which adhere to the ECN specifications[3]. The ambient gas is N_2 at 343 K, and the fuel is n-dodecane at 303 K. Table 1.1 summarizes the fluid and flow properties used, and key non-dimensional quantities are listed in Table 1.2. In the present simulations the inlet flow velocity (at the blue inlet faces in Fig. 1.1) is specified such that the jet velocity at the orifice opening matches the experimentally estimated value of 412 m/s [34].

---

[3] `https://ecn.sandia.gov/diesel-spray-combustion/target-condition/spray-ab/`

Table 1.1: Fluid properties

ρ_l (kg/m^3)	ρ_g (kg/m^3)	ν_l (m^2/s)	ν_g (m^2/s)	σ (N/m)	U_{inj} (m/s)
715	22.8	1.007×10^{-6}	1.79×10^{-5}	0.021	412

Table 1.2: Values for relevant non-dimensional numbers

Re_l $(U_{inj.}D/\nu_l)$	We_l $(\rho_l U_{inj.}^2 D/\sigma)$	Oh_l $(We_l^{1/2}/Re_l)$	ρ_l/ρ_g -
$36,822$	5.2×10^5	1.9×10^{-2}	31.36

1.4 Injector Nozzle Geometry

A single-hole, 90 μm diameter, Bosch injector named Spray A by the Engine Combustion Network[4] (ECN) collaboration, is used for the present study as it has been characterized extensively [34, 35], particularly in the near field. In the present work, the nozzle surface file[5] for the ECN Spray A nozzle (serial# 210675) has been used for generating the computational grid. The nozzle geometry including details of its asymmetry and nozzle alignment are displayed in Fig. 1.5a. The surface file reconstructed from X-ray tomography measurements, shown in Fig. 1.5a, clearly reveals the offset of the nozzle hole from the sac centerline (dashed line). Additionally, the inlet turning angles, for instance θ_1 and θ_2 are not the same [35]. Furthermore, the diameter of the nozzle hole decreases along the streamwise direction.

In this section we examine the difference between the two Spray A nozzle geometries that are used in the study. We quantify the surface roughness for both the geometries and examine the level to which the simulation grids capture the surface features.

Kastengren et al. [35] point out that due to the manufacturing challenges associated with the small dimensions of the nozzles the actual nozzle profiles deviate from the nominal specifications. They present measurements for four different Spray A nozzles and note that the orifices in all the

---

[4] `https://ecn.sandia.gov/`

[5] `https://ecn.sandia.gov/diesel-spray-combustion/computational-method/meshes/`

Table 1.3: Average cell size values for the different spray configurations and grid resolution levels.

Geometry	Coarse	Medium	Fine
Spray A (Educated)	5.9 μm	3.9 μm	2.8 μm
Spray A (Unprocessed)	5.8 μm	4.5 μm	2.9 μm
Only External	5.4 μm	4.4 μm	3.1 μm

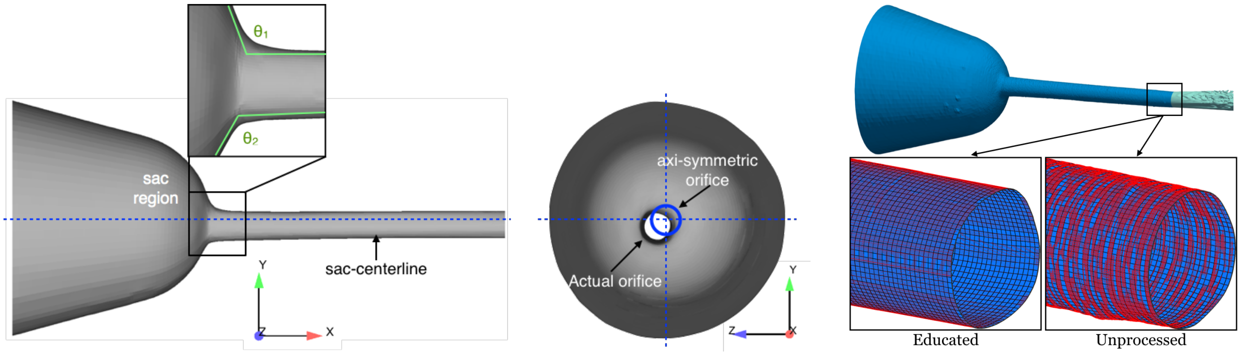

(a) Asymmetries of the ECN SprayA nozzle are depicted. The actual alignment of the orifice superimposed on the axi-symmetric location is displayed. The dashed lined highlights the offset between the sac and the nozzle conduit. The variation in internal turning angles is emphasized in the inset where $\theta_1 \neq \theta_2$.

(b) Details of the near-exit portion of the Unprocessed Spray A nozzle are presented here. A comparison between the STL data (red) and the VoF grid (blue) employed for the study is shown.

Figure 1.5: Details of the two Spray A nozzle variations are shown

nozzles have an offset with respect to the sac region, which creates an asymmetry. The offset and hence the level of asymmetry varies nozzle-to-nozzle. Also, the holes are angled with respect to the injector axis by 0.3° to 0.4°. The measured value of the nozzle K-factor, which is a measure of the taper of the orifice, vary from 1.3 to 1.8 as opposed to the nominal value of 1.5[6][35]. There is also notable surface roughness in these nozzle geometries.

In the present study we attempt to incorporate the asymmetries and imperfections in the nozzle gometries and study their effects. Therefore, surface stereolithography (STL) files based on scans of a real nozzle are used here to generate the computational domains. As mentioned in Section 1.3, two variations of the Spray A nozzle are used here. The corresponding STL files are both based on

---

[6] `https://ecn.sandia.gov/diesel-spray-combustion/target-condition/spray-a-nozzle-geometry/`

reconstructions of raw X-ray tomography measurements that have been processed and converted into usable STL files. The STL files used in this study come from two different sources and differ in the way the raw data has been processed. These differences between the two geometries are highlighted below.

(a) The first surface file, referred to as the 'Educated Geometry', has been provided by Georgia Institute of Technology[7]. This surface file is a spline-reconstructed representation of a collection of multiple X-ray tomography measurements. While this processing is aimed at removing artificial experimental artifacts, it also makes the surface finish smoother.

(b) The second surface file has been provided by CNRS France[8]. This is based on high-resolution X-ray tomography data that was smoothed to create the STL file. This geometry is relatively unprocessed and is simply referred to as 'Unprocessed Spray A' in this study.

Fig. 1.5b shows the near-orifice region for the two nozzle geometries. On the left is the educated geometry and on the right is the unprocessed geometry. In both images, the STL geometry is shown in red while the VoF grid is shown in blue. The difference between the surface finish of the two geometries is evident through this image.

The surfaces for both nozzle surfaces exhibit deviations from a purely cylindrical geometry, which are quantified by

$$\epsilon_{cyl}(\theta_i, x_j) = |r(\theta_i, x_j) - R_0|, \tag{1.8}$$

where R_0 ($= D_0/2 = 45\,\mu$m) is the nominal radius of the Spray A nozzle, and (θ_i, x_j) are discrete azimuthal and axial coordinates, respectively. Each point in Fig. 1.6 represents a distinct value for the aforementioned coordinates and are colored by the magnitude of $\epsilon_{cyl}(\theta_i, x_j)$. An average

---

[7] `https://ecn.sandia.gov/diesel-spray-combustion/computational-method/meshes/`

[8] `https://ecn.sandia.gov/cvdata/targetCondition/CNRS675correct.stl`

deviation of the STL surface from the cylindrical shape is evaluated as,

$$\overline{\epsilon_{cyl}} = \frac{\sum_{i,j}^{n_x, n_\theta} \epsilon(\theta_i, x_j)}{n_x n_\theta}. \tag{1.9}$$

The values for $\overline{\epsilon_{cyl}}$ are reported in Table 1.4. It is observed that the level of overall departure from cylindrical shape is similar among Educated and the Unprocessed Spray A nozzle. However, a closer inspection of Fig. 1.6 reveals that the variations along the streamwise (x) direction are much smaller for the Educated Spray A geometry. Since the strongest component of the flow is its x-component, we are particularly interest in surface roughness encountered along this coordinate. To quantify this variation we first compute an axial average surface location, defined by,

$$\overline{r}(\theta_i) = \frac{\sum_{j=1}^{n_x} r(\theta_i, x_j)}{n_x}. \tag{1.10}$$

Fig. 1.6 shows nozzle surface profiles, $r(\theta_i, x_j)$ at 6 different axial locations. The black curve represents the mean profile, $\overline{r}(\theta_i)$. As observed in Fig. 1.6, while the level of variation along θ is comparable between the two geometries, the level of axial variation is significantly higher in the Unprocessed geometry.

To quantity the degree of surface variation in the x-direction, the local deviation of the STL surface from its axially average is evaluated as,

$$\epsilon_x(\theta_i, x_j) = |r(\theta_i, x_j) - \overline{r}(\theta_j)|, \tag{1.11}$$

which can be subsequently averaged yielding,

$$\overline{\epsilon_x} = \frac{\sum_{i,j}^{n_x, n_\theta} \epsilon_x(\theta_i, x_j)}{n_x n_\theta}. \tag{1.12}$$

The corresponding values are also reported in Table 1.4, where it is confirmed that the Unprocessed geometry is significantly rougher in the x-direction in comparison to the Educated geometry.

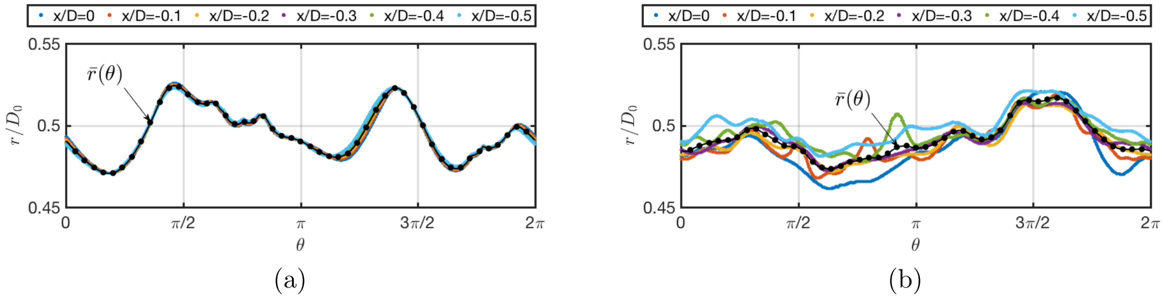

Figure 1.6: The nozzle surface r is presented as a function of θ at 6 different axial locations for the two geometries. The black curves represent $\overline{r}(\theta)$ as given by Eq. (1.10).

The material up to this point has considered the axial and azimuthal surface variations of the STL surface file; however, in the computations it is the computational or VoF grid that is employed, not the STL surface. While the nodes of the VoF grid lie on the STL surface by construction, the linear edges and the planar faces of the grid may not exactly coincide with the arbitrary STL surface. Therefore, it is entirely possible that a small discrepancy exists between the VoF surface and the STL surface. To quantify this discrepancy, the shortest distance between each of the STL points and the VoF grid is computed

$$\epsilon_{grid}(\theta_i, x_j) = |r_{grid}(\theta_i, x_j) - r_{STL}(\theta_i, x_j)| \tag{1.13}$$

and shown in Fig. 1.7. The mean value of this discrepancy between the STL points and the different VoF grids corresponding to different levels of resolution are reported in Table 1.4. Clearly, for the finest resolved cases the reported level of discrepancy is approximately two orders of magnitude smaller than the departure from cylindrical shape, and significantly smaller than $\overline{\epsilon_x}$.

In summary, both Spray A nozzle geometries exhibit a noticeable departure from a perfectly cylindrical nozzle, although the $\overline{\epsilon_{cyl}}$ values are much smaller than the nominal nozzle diameter. The level of surface variations along the azimuthal direction are comparable between the two geometries,

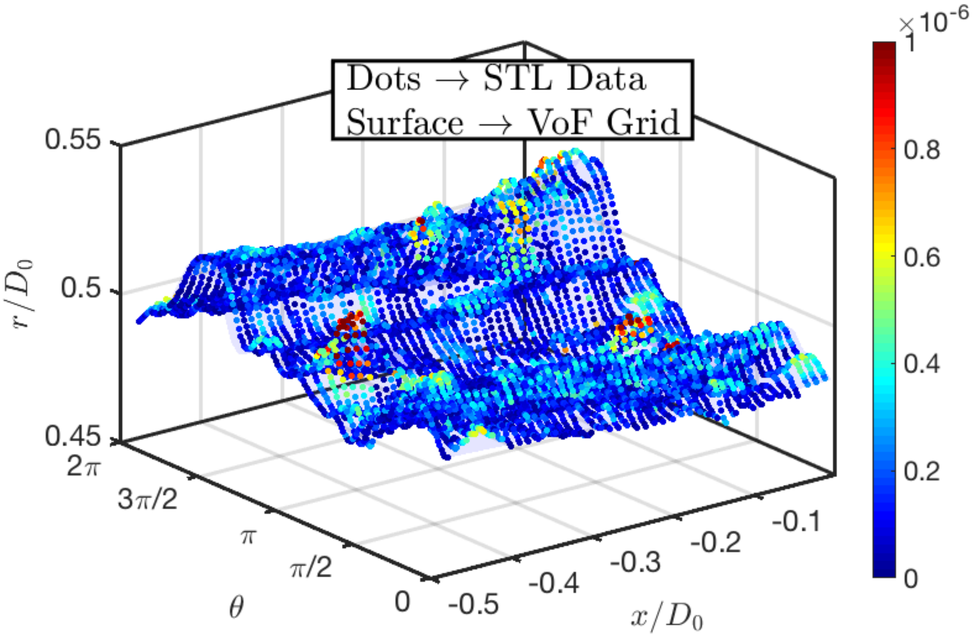

Figure 1.7: Evaluation of the degree of agreement between the STD surface data and the corresponding VoF grid in the near-exit portion of the Unprocessed Spray A nozzle. The STL data are shown as dots and the VoF grid as a blue surface with black edges. The colors shown in the color bar represent the distance between the STL data and the VoF grid.

but the level of surface variations in the streamwise direction differ significantly between the two nozzles with the Unprocessed geometry have much larger axial variation. As documented below this level of increased $\overline{\epsilon_x}$ leads to significant changes in both the mean and fluctuation velocity components of the fluid emanating from the nozzle. With respect to the degree of fidelity of the VoF grids in capturing the detailed surface features present in the STL files, the highest resolved case is able to accurately represent these features. The only exception is perhaps the $\overline{\epsilon_x}$ for the Educated geometry, but this value is already minute, i.e. 61.1 nm.

1.5 Spray A validation

Deshpande et al. [20] have presented a thorough evaluation of `interFOAM` performance with respect to kinematics of advection, dynamics in inertia dominated regime, and dynamics in the surface

Table 1.4: Roughness values for the two Spray A geometries used here. Average clearance between the VoF grids and the STL nozzle geometries for the different grid sizes.

Geometry	STL Characterization		Mean clearance between STL data and VoF grid		
	$\overline{\epsilon_{cyl}}$ (Eq. (1.9))	$\overline{\epsilon_x}$ (Eq. (1.12))	Coarse	Medium	Fine
Educated Spray A	1.35 μm	61.1 nm	668.0 nm	198.5 nm	41.4 nm
Unprocessed Spray A	1.21 μm	393.3 nm	165.2 nm	128.1 nm	89.0 nm

tension dominated regime. Validation tests have also been previously presented for two-phase mixing layers and co-flow atomization [21]. In this section results for the Educated Spray A configuration are compared with results for the Unprocessed Spray A configuration.

The metric for comparison is the Projected Mass Density (PMD), which is denoted as Φ. PMD is the line integrated liquid mass, and represents the projection of the 3D liquid mass distribution on a 2D plane. PMD computed along the y and z axes is respectively given by

$$\Phi_y(x,z) = \rho_l \int_{-\infty}^{\infty} \langle \alpha(x,y,z) \rangle \, \mathrm{d}y, \tag{1.14a}$$

$$\Phi_z(x,y) = \rho_l \int_{-\infty}^{\infty} \langle \alpha(x,y,z) \rangle \, \mathrm{d}z. \tag{1.14b}$$

All computational data is reported in the form of temporally-averaged values, recognizing the fact that beyond the initial transient the process is statistically stationary. The time integration for α is given by,

$$\langle \alpha(x,y,z) \rangle = \frac{1}{t_f - t_i} \int_{t_i}^{t_f} \alpha(x,y,z,t) \, \mathrm{d}t, \tag{1.15}$$

where $t_i = 25\,\mu$s and $t_f = 50\,\mu$s to ensure statistical convergence.

Quantitative comparisons of computed PMD against streamline centerline experimental [76] and transverse [34] measurements are presented in Fig. 1.8. From the data in these plots, it is clear that the Educated Spray A results are closer to the experiments than the results from the Unprocessed Spray A. The external-only data is the furthest away from the experiments and consistently over-predicts the PMD. This is particularly the case for the centerline Φ_z profile. For both the Spray A configurations shown here, there is a reasonable degree of numerical convergence with grid refinement, which is examined in Section 2.2.5. The results also reveal a considerable measure of spray asymmetry, particularly for the Unprocessed configuration. This feature has also been reported in experimental findings by Kastengren et al. [34]. The asymmetry is the lowest in the external-only configuration, as expected.

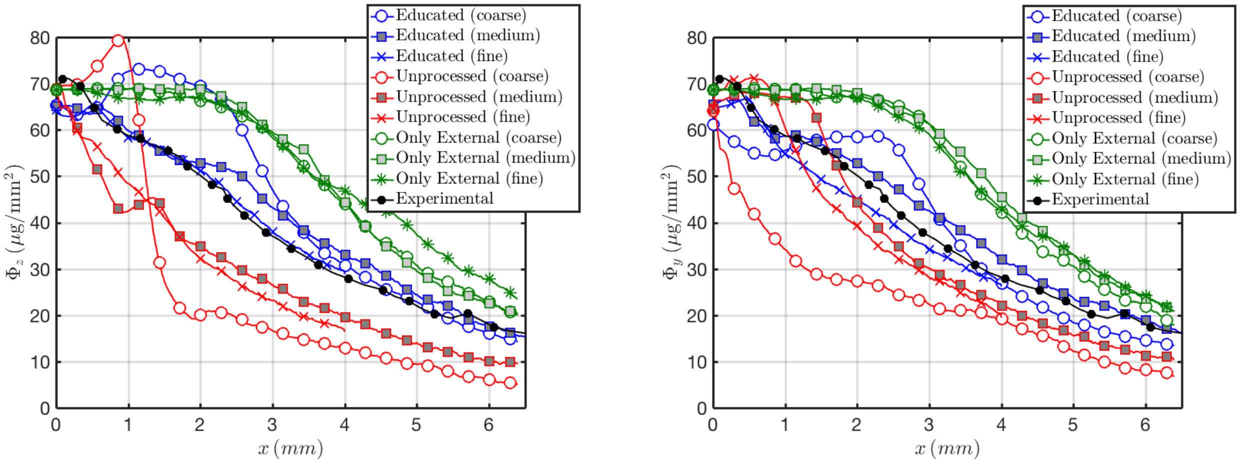

(a) Φ_z (b) Φ_y

Figure 1.8: The projected mass density, Φ, along the spray centerline for two different projection axes: (a) projection along z direction, Φ_z, (b) projection along y direction, Φ_y.

To inspect the radial distribution of liquid mass at different axial locations, Fig. 1.9 and Fig. 1.10 include plots of Φ_z and Φ_y, respectively, for the 3 spray nozzle geometries. As noted in Section 1.4, the spray axis is offset from the injector axis. The choice of the origin in the experimental setup may not be exactly consistent with the origin in the simulations. To correct for this offset, the experimental spray axis has been shifted by 0.018 mm to match with the measured peak at $x = 0.1\,\text{mm}$ in the comparisons shown. Moreover, the spray from the Unprocessed geometry is highly asymmetrical and the orientation (i.e., orientation in terms of the direction of the y and z axes, see Fig. 1.5a) of the experimental setup cannot be expected to coincide with the orientation of the STL data, which is used in the simulations. Predictions corresponding to increasing levels of numerical refinement are included in the comparisons, and in line with the previous centerline figures, the predictions from the coarse grid are substantially off from the higher refined cases and also noticeably different from the measurements.

Beginning with Φ_z in Fig. 1.9, the computational results based on the Educated geometry match relatively well the experimental data. The overall trend is one of a broadening of the Φ_z profile as we move downstream. This is directly caused by the ongoing breakup and radial spreading of liquid elements. The new results corresponding to the Unprocessed geometry show a noticeable degree of discrepancy with measurements, which progressively becomes worse with increasing distance from the nozzle orifice. For instance, the level of disparity at $x = 6$ mm is substantial. In the near field, however, since the jet is largely intact, the three sets of predictions corresponding to the different injection configurations agree well with the experiments.

For the Φ_y profiles, included in Fig. 1.10, the qualitative trends are essentially the same as those for Φ_z. The notable difference is that the level of asymmetry of the results corresponding to the Unprocessed geometry is even more pronounced. For instance, the peak of the profile at $x =4$ mm is substantially removed from the centerline. At the farthest location reported, i.e., $x = 6\,\mathrm{mm}$, the spray has spread significantly. We note that there are only two computational curves at $x = 6\,\mathrm{mm}$, to reduce computational costs associated with running cases at the finest resolution this far from the near-nozzle region.

To quantify the error in the numerical results, a mean relative error, $\mathcal{E}_\Phi$, defined as

$$\mathcal{E}_\Phi = \frac{1}{N}\sum_{i=1}^{N}\frac{|\Phi_{num,i} - \Phi_{exp,i}|}{\Phi_{exp,x=0}}, \tag{1.16}$$

is reported in Table 1.5 for Φ_z and Table 1.6 for Φ_y. Here the subscript 'num' and 'exp' refers to numerical and experimental values, respectively, and N is the total number of data points.

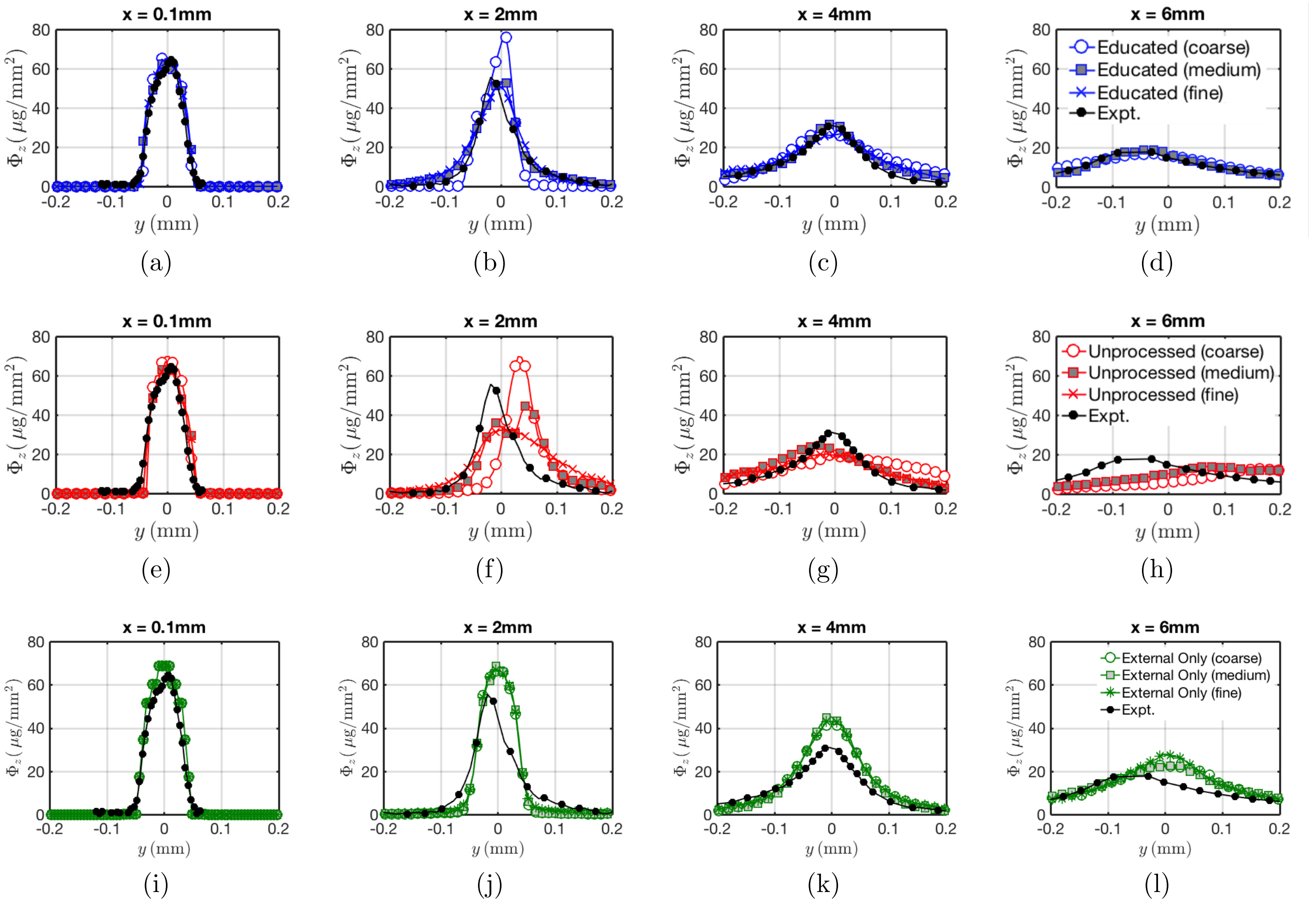

(a) (b) (c) (d)

(e) (f) (g) (h)

(i) (j) (k) (l)

Figure 1.9: The projected mass density, Φ_z, across the spray at four axial locations: Educated Spray A – (a) $x = 0.1\,\mathrm{mm}$, (b) $x = 2\,\mathrm{mm}$, (c) $x = 4\,\mathrm{mm}$ and (d) $x = 6\,\mathrm{mm}$; Unprocessed Spray A – (e) $x = 0.1\,\mathrm{mm}$, (f) $x = 2\,\mathrm{mm}$, (g) $x = 4\,\mathrm{mm}$ and (h) $x = 6\,\mathrm{mm}$; External Only – (i) $x = 0.1\,\mathrm{mm}$, (j) $x = 2\,\mathrm{mm}$, (k) $x = 4\,\mathrm{mm}$ and (l) $x = 6\,\mathrm{mm}$.

Predictions employing the Educated geometry show a consistent level of numerical convergence with the error being bounded by 6.5% for the medium and fine cases. For the Unprocessed configuration, the predictions do show a significant decrease in error from the coarse grid to the medium and fine grid calculations. However, the level of error is significantly larger than for the Educated geometry as previously discussed. Although the uncertainty in the associated experimental data has not been reported [34, 76], Kastengren et al. [33] indicate a standard deviation of up to 4% in their PMD data for similar measurements. Hence, the degree of error in the Spray A numerical predictions is

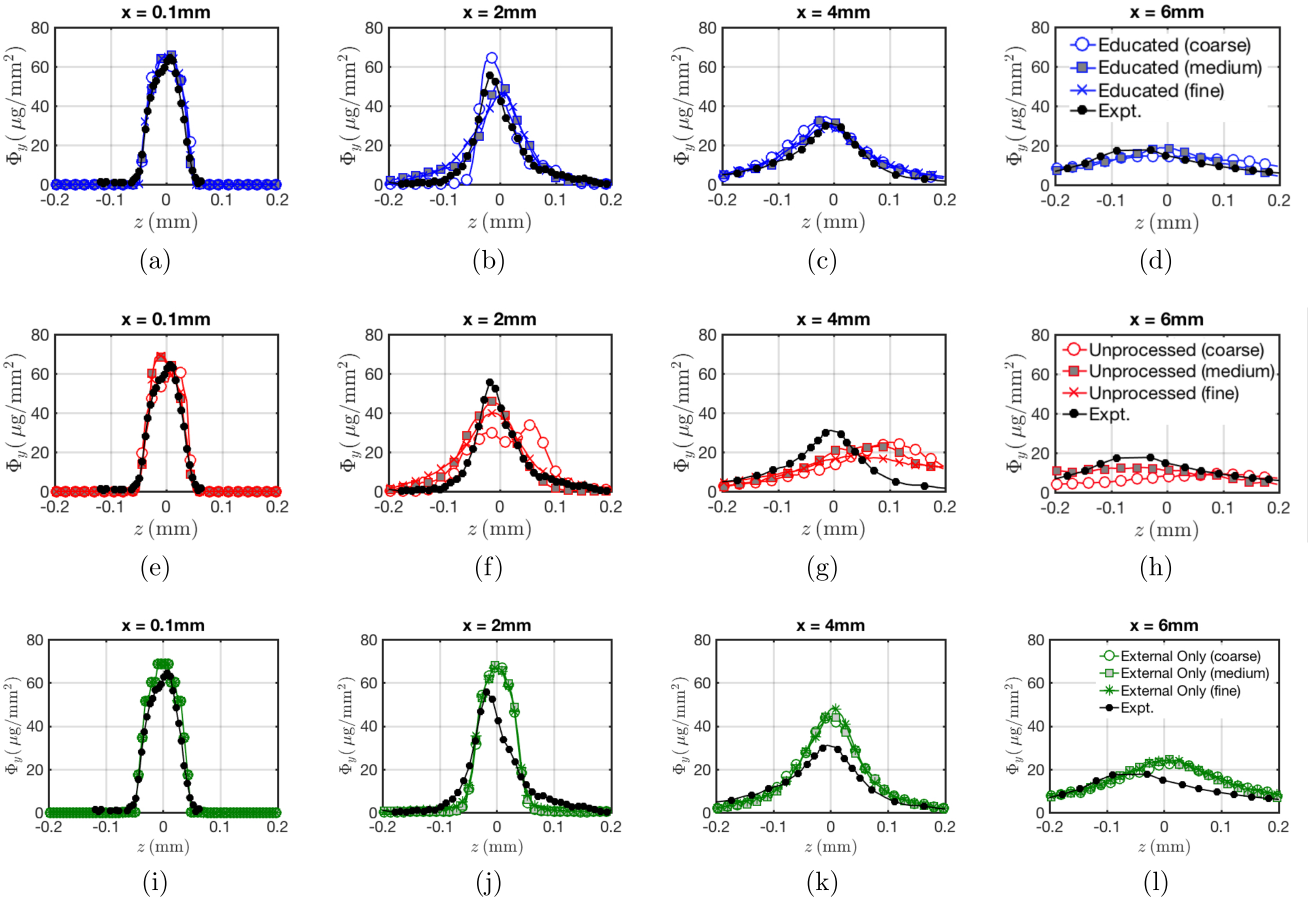

Figure 1.10: The projected mass density, Φ_y, across the spray at four axial locations: Educated Spray A – (a) $x = 0.1$ mm, (b) $x = 2$ mm, (c) $x = 4$ mm and (d) $x = 6$ mm; Unprocessed Spray A – (e) $x = 0.1$ mm, (f) $x = 2$ mm, (g) $x = 4$ mm and (h) $x = 6$ mm; External Only – (i) $x = 0.1$ mm, (j) $x = 2$ mm, (k) $x = 4$ mm and (l) $x = 6$ mm.

on the same order as this standard deviation. For the External-only configuration, the PMD curves do not vary much with respect to grid refinement, but they do not converge to the experimental curve (as expected since the internal flow is not simulated). Therefore, the error values remain consistent across the different grid levels.

Table 1.5: Relative error values, $\mathcal{E}_\Phi$, for the PMD curves in Fig. 1.8a and Fig. 1.9.

Configuration	Δx	Centerline Φ_z	Transverse (Φ_z)			
			x=0.1 mm	x=2 mm	x=4 mm	x=6 mm
Educated Spray A	Coarse	10.7%	4.7%	7.7%	5.2%	1.7%
	Medium	4.4%	3.8%	3.7%	2.5%	1.1%
	Fine	2.0%	3.9%	4.6%	4.0%	–
Unprocessed Spray A	Coarse	23.3%	6.0%	17.5%	7.4%	10.0%
	Medium	15.2%	4.3%	10.7%	5.6%	8.0%
	Fine	18.4%	4.6%	10.2%	5.0%	–
Only External	Coarse	16.9%	5.2%	8.4%	6.7%	5.4%
	Medium	17.5%	5.2%	8.4%	6.8%	4.9%
	Fine	19.5%	5.2%	7.8%	6.7%	6.4%

Table 1.6: Relative error values, $\mathcal{E}_\Phi$, for the PMD curves in Fig. 1.8b and Fig. 1.10.

Configuration	Δx	Centerline Φ_y	Transverse (Φ_y)			
			x=0.1 mm	x=2 mm	x=4 mm	x=6 mm
Educated Spray A	Coarse	7.3%	4.2%	4.5%	4.0%	3.7%
	Medium	3.5%	3.6%	6.5%	2.7%	3.0%
	Fine	5.0%	3.8%	6.1%	3.4%	-
Unprocessed Spray A	Coarse	22.0%	4.8%	8.8%	14.4%	7.3%
	Medium	8.7%	4.0%	5.7%	11.1%	3.9%
	Fine	10.9%	4.3%	6.6%	9.4%	-
Only External	Coarse	16.5%	5.2%	8.5%	6.8%	5.5%
	Medium	18.7%	5.2%	8.4%	6.8%	5.4%
	Fine	17.0%	5.2%	7.5%	6.2%	6.0%

1.6 Linear Stability Analysis – Underlying Assumptions

Most common breakup models are based on the KH framework. The theoretical underpinning of this framework, or of the more general Orr-Sommerfeld (OS) approach, lies in a linearized momentum equation. The most obvious departure from this treatment is the presence of the non-linear advection term. But in fact, there are more subtle implications of the KH or OS framework that also merit investigation. To see this more clearly we perform the typical base field (upper case) and perturbation field (lower case) decomposition [63]. For velocity we have

$$\tilde{\mathbf{U}}^q(\mathbf{x},t) = \mathbf{U}^q(\mathbf{x}) + \mathbf{u}^q(\mathbf{x},t), \tag{1.17}$$

and for pressure

$$\tilde{P}^q(\mathbf{x},t) = P^q(\mathbf{x}) + p^q(\mathbf{x},t), \tag{1.18}$$

where $(\tilde{\mathbf{U}}, \tilde{P})$ denote the instantaneous velocity and pressure fields, and the superscript q denotes either the liquid (L) or gas phase (G); $\mathbf{U} = (U, V, W)$; and $\mathbf{u} = (u, v, w)$. Furthermore, the velocity fields can be rewritten in terms of axial terms, along the x coordinate, and a non-axial component or orthogonal component, i.e. $\mathbf{u} = \mathbf{u}_\perp + u\mathbf{e}_x$, and $\mathbf{U} = \mathbf{U}_\perp + U\mathbf{e}_x$ ($\mathbf{e}_x$ is the unit vector in the x-direction).

Substituting the previous decomposition into the incompressible form of the Navier-Stokes equation and recognizing that the base flow field automatically satisfies this equation yields an expression for the perturbed fields,

$$\frac{\partial \mathbf{u}^q}{\partial t} + \underbrace{U^q \partial_x \mathbf{u}^q + \mathbf{u}^q_\perp \cdot \nabla \mathbf{U}^q}_{\substack{\text{advection terms present}\\ \text{in the convential system}}} + \underbrace{\overbrace{\mathbf{u}^q \cdot \nabla \mathbf{u}^q}^{\substack{\text{Non-Linear}\\ \text{Perturbation}}} + \overbrace{\mathbf{U}^q_\perp \cdot \nabla \mathbf{u}^q}^{\substack{\text{Non-Axial}\\ \text{Velocity}\\ \text{(Eq. (1.22))}}} + \overbrace{u^q \partial_x \mathbf{U}^q}^{\substack{\text{Axially Developing}\\ \text{Velocity}\\ \text{(Eq. (1.24))}}}}_{\text{advection terms ignored in the conventional system}} = -\frac{1}{\rho^q}\nabla p^q + \nu^q \nabla^2 \mathbf{u}^q, \tag{1.19}$$

where ν is the kinematic viscosity. This expression represents the full form of the governing equation for $(\mathbf{u}^q, p^q)$. In the governing equation commonly seen in linear-stability analyses [23, 63] many of the above terms are ignored (as indicated in Eq. (1.19)) resulting in the following reduced or conventional form for the PDE governing the perturbed fields

$$\frac{\partial \mathbf{u}^q}{\partial t} + U^q \partial_x \mathbf{u}^q + \mathbf{u}_\perp^q \cdot \nabla \mathbf{U}^q = -\frac{1}{\rho^q} \nabla p^q + \nu^q \nabla^2 \mathbf{u}^q. \tag{1.20}$$

Elaborating on the omitted terms from Eq. (1.19) as well as other assumptions employed in linear-stability analysis, we have the following:

A. **Non-linear advection**: The velocity perturbations are assumed to be small compared to the base velocity ($\mathcal{O}(u^q) \ll \mathcal{O}(U^q)$). Therefore, the non-linear perturbation terms are ignored. This is quantified in the present work with the following metric

$$\beta_{NL}(\mathbf{x}, t) = \frac{|\mathbf{u}^q \cdot \nabla \mathbf{u}^q|}{|U^q \partial_x \mathbf{u}^q + \mathbf{u}_\perp^q \cdot \nabla \mathbf{U}^q|}. \tag{1.21}$$

B. **Base velocity**: In the conventional interface instability analysis, the base velocity is assumed to be of the form $\mathbf{U}^q(\mathbf{x}) = U^q(y)\mathbf{e}_x$. This implies that:

   i. Non-axial components of the base velocity are zero, i.e. $V^q = W^q = 0$. Therefore, the following part of the advection terms reduces to

$$V^q \frac{\partial \mathbf{u}^q}{\partial y} + W^q \frac{\partial \mathbf{u}^q}{\partial z} = \mathbf{U}_\perp^q \cdot \nabla \mathbf{u}^q = \mathbf{0}. \tag{1.22}$$

   To quantity how well these terms remain at zero the following metric is employed:

$$\beta_{NA}(\mathbf{x}, t) = \frac{|\mathbf{U}_\perp^q \cdot \nabla \mathbf{u}^q|}{|U^q \partial_x \mathbf{u}^q + \mathbf{u}_\perp^q \cdot \nabla \mathbf{U}^q|}. \tag{1.23}$$

ii. Similarly, $\mathbf{U}^q(\mathbf{x})$ is assumed to be fully developed along the jet axis ($\mathbf{U}^q(\mathbf{x}) = \mathbf{U}^q(y,z)$). This implies that,

$$u^q \frac{\partial \mathbf{U}^q}{\partial x} = \mathbf{0}. \tag{1.24}$$

This assumption is also tested with

$$\beta_{NFD}(\mathbf{x},t) = \frac{|u^q \partial_x \mathbf{U}^q|}{|U^q \partial_x \mathbf{u}^q + \mathbf{u}_\perp^q \cdot \nabla \mathbf{U}^q|}. \tag{1.25}$$

C. **Interface shape**: For linear stability analysis, the interface is assumed to be described by the superposition of various modes having the following form [42]

$$\xi(x,t) = \sum_{k=-\infty}^{\infty} \xi_k \exp(\omega t + ikx). \tag{1.26}$$

This appearance is tested by inspection.

To evaluate the metrics defined above, $\mathbf{u}^q$ and $\mathbf{U}^q$ are required. Noting from Eq. (1.17) that the $\tilde{\mathbf{U}}^q(\mathbf{x},t)$ field can be decomposed as

$$\tilde{\mathbf{U}}^q(\mathbf{x},t) = \mathbf{U}^q(\mathbf{x}) + \mathbf{u}^q(\mathbf{x},t), \tag{1.27}$$

we perform an averaging operation, $\langle \dots \rangle$, to yield

$$\mathbf{U}^q(\mathbf{x}) = \langle \tilde{\mathbf{U}}^q(\mathbf{x},t) \rangle. \tag{1.28}$$

This expression along with Eq. (1.27) allows us to write

$$\mathbf{u}^q(\mathbf{x},t) = \tilde{\mathbf{U}}^q(\mathbf{x},t) - \langle \tilde{\mathbf{U}}^q(\mathbf{x},t) \rangle. \tag{1.29}$$

Together Eq. (1.21) through Eq. (1.25) provide for a pointwise determination of β_{NL}, β_{NA}, and β_{NFD}. To obtain a more global metric, these quantities are integrated and averaged over a cross-sectional slice of the jet, namely,

$$\overline{\beta_{NL}}(x,t) = \frac{1}{|\Omega_\beta^q|} \iint\limits_{\Omega_\beta^q} \beta_{NL}(\mathbf{x},t)\,\mathrm{d}y\mathrm{d}z, \tag{1.30a}$$

$$\overline{\beta_{NA}}(x,t) = \frac{1}{|\Omega_\beta^q|} \iint\limits_{\Omega_\beta^q} \beta_{NA}(\mathbf{x},t)\,\mathrm{d}y\mathrm{d}z, \tag{1.30b}$$

$$\overline{\beta_{NFD}}(x,t) = \frac{1}{|\Omega_\beta^q|} \iint_{\Omega_\beta^q} \beta_{NFD}(\mathbf{x},t)\mathrm{d}y\mathrm{d}z, \tag{1.30c}$$

where again $q = [L,G]$. The region Ω_β^L is a subset of the y-z plane that extends $3\Delta x$ into the liquid phase from the $\alpha = 0.5$ isoline. Analogously, the Ω_β^G also resides in y-z plane and extends $3\Delta x$ into the gas phase from the $\alpha = 0.5$ isoline. For the internal nozzle domain, Ω_β^L extends three cells from the wall.

Additionally, the metrics are time-averaged as,

$$\langle\overline{\beta_{NL}}\rangle(x) = \frac{1}{t_f - t_i}\int_{t_i}^{t_f} \overline{\beta_{NL}}(x,t)\,\mathrm{d}t, \tag{1.31a}$$

$$\langle\overline{\beta_{NA}}\rangle(x) = \frac{1}{t_f - t_i}\int_{t_i}^{t_f} \overline{\beta_{NA}}(x,t)\,\mathrm{d}t, \tag{1.31b}$$

$$\langle\overline{\beta_{NFD}}\rangle(x) = \frac{1}{t_f - t_i}\int_{t_i}^{t_f} \overline{\beta_{NFD}}(x,t)\,\mathrm{d}t, \tag{1.31c}$$

where t_f and t_i have the same values given in Section 1.5, namely $t_i = 25\,\mu$s and $t_f = 50\,\mu$s.

1.7 Results

In the results presented in the following subsections, the quasi-steady or statistically stationary portion of the injection event is exclusively considered. At the corresponding injection speeds considered in the present study, the initial transient period occupies a small fraction of the total injection duration; hence, most of the interesting injection processes, which occur within $x/d_0 \lesssim 50$, lie most of the time within the quasi-steady state.

1.7.1 Examining the Extent of Linear Theory Assumptions

We consider first the behavior of the underlying linear components of advection. These are presented as a function of distance from the orifice exit in Fig. 1.11 both inside the nozzle ($x < 0$) and outside the nozzle ($x > 0$) for the different grid resolution cases. Similar to the validation data presented in Section 1.5, results for $\Delta x = 5.9\,\mu$m are under-resolved and do not capture the dynamics recorded at the finer grid resolutions. Hence, we focus our discussions on the two finer cases ($\Delta x = 3.9\,\mu$m and $2.8\,\mu$m) for the evaluation of linear advection terms, β_{NL}, β_{NA}, and β_{NFD}. Due to the development of instabilities produced by the growing shear layer, the advection term is significantly affected. It shows an exponential dependence that is given by $|U^q \partial_x \mathbf{u}^q + \mathbf{u}_\perp^q \cdot \nabla \mathbf{U}^q| \cong C_1 e^{m(x/d_0)}$, where C_1 is a constant and $m = 0.89$ for the finest grid.

With respect to growth of the non-linear term, Fig. 1.12 shows the axial profile of β_{NL} (Eq. (1.21)) in both the liquid (Fig. 1.12a) and gas (Fig. 1.12b) phase. For the liquid phase, inside the nozzle ($x < 0$) the terms are $\mathcal{O}(10^{-2})$ and thus the advection is dominated by the linear components. In the external domain ($x > 0$), the relative magnitudes rapidly rise to $\mathcal{O}(10^{-1})$ by $x = 4d_0$. As the grid size is reduced, the trends show convergence. A similar behavior, but with higher magnitudes, is observed in the gas phase. This indicates that the linearity assumption becomes questionable beyond $x = 4d_0$. It will be shown in Section 1.7.2, that in the vicinity of this region, the associated growth of non-linearities is combined with the development of non-sinusoidal free surface

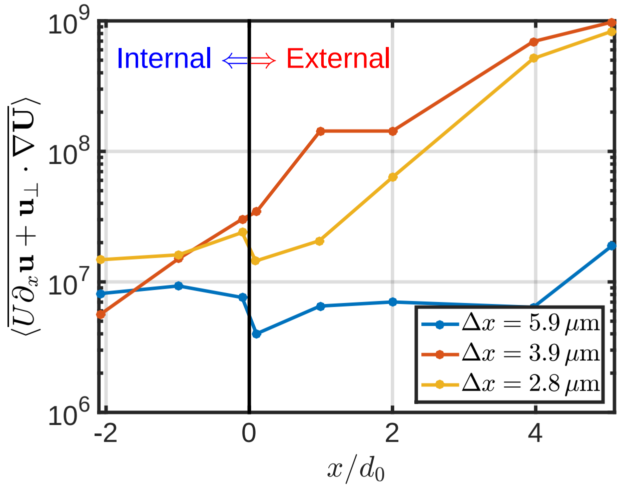

Figure 1.11: Magnitude of the advection terms in the linearized equation, $U\partial_x\mathbf{u} + \mathbf{u}_\perp \cdot \nabla\mathbf{U}$, corresponding to the liquid phase.

disturbances.

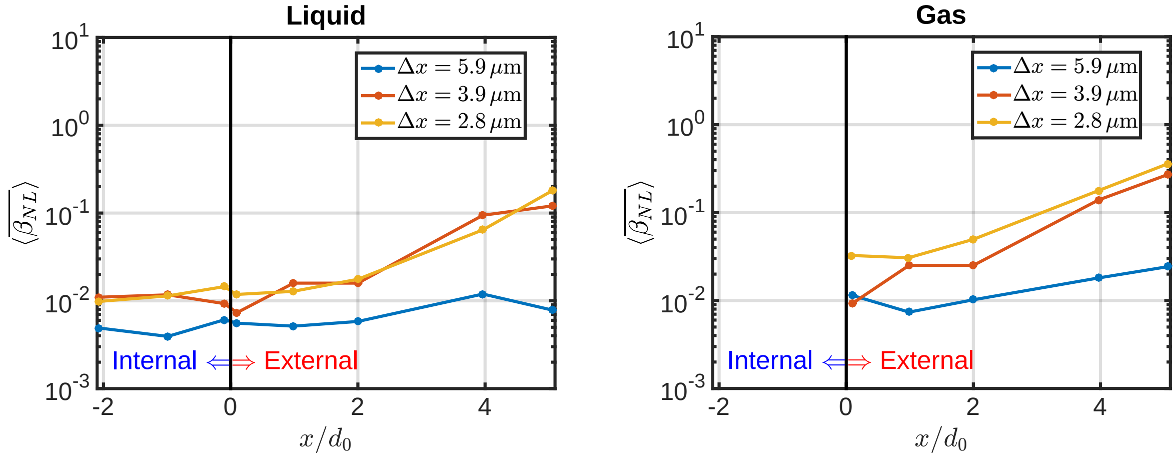

(a) (b)

Figure 1.12: Magnitude of non-linear perturbation in the (a) liquid phase and (b) gas phase.

The trends of the non-axial velocity terms quantified by β_{NA} are shown in Fig. 1.13 for the liquid and gas phases. Inside the nozzle β_{NA} is $\mathcal{O}(10^{-1})$ indicating that there is a notable non-axial component to the base velocity. This non-axial velocity component is attributed directly to the nozzle imperfections and asymmetries. At the orifice opening the β_{NA} field is large enough that ignoring its presence in linear stability analysis is questionable. Non-axial base velocity at the orifice leads to an asymmetric free surface disturbance, which consequently affects the spray formation. For the gas phase, the magnitude of β_{NA} (Fig. 1.13b) is higher than that of the liquid phase. β_{NA} remains relatively small through the near-field indicating that non-axial terms are secondary to the dominant growth of the non-linear terms.

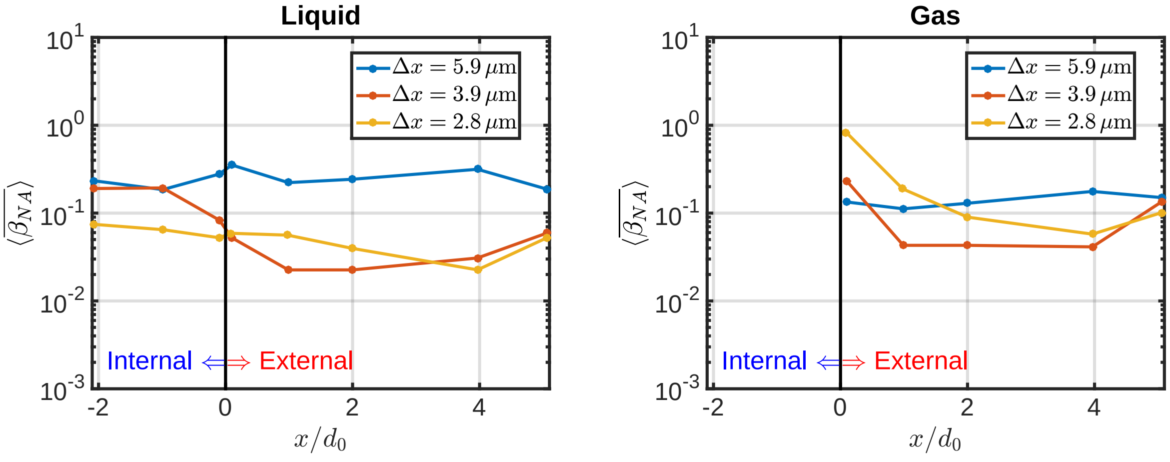

(a) (b)

Figure 1.13: Magnitude of non-axial velocity terms in the (a) liquid phase and (b) gas phase.

Lastly, the results concerning the non-fully developed terms measured by β_{NFD} are shown in Fig. 1.14 for both liquid and gas phases. At the orifice opening β_{NFD} is around $\mathcal{O}(10^{-1})$, especially for the gas phase (Fig. 1.14b). The axial gradient discontinuity at $x = 0$ (at the orifice) can be attributed to velocity profile relaxation. This relaxation is produced by a change from a no-slip to a slip boundary condition corresponding to a change from an internal wall-bounded flow to a free surface flow as the fluid travels out of the nozzle.

Downstream from the orifice opening β_{NFD} appears to decrease to $\mathcal{O}(10^{-2})$ for both liquid and gas phases. Similar to the non-axial terms, the axially developing terms are high enough at the orifice opening that ignoring them is questionable. This behavior is caused by significant gas entrainment in the near orifice region ($x < 2d_0$). Entrainment leads to non-zero gas velocities and velocity gradients. This is seen in the high magnitudes of the non-axial velocity terms, $\mathbf{U}_{\perp}^{(g)} \cdot \nabla \mathbf{u}^{(g)}$, and axially developing velocity terms, $u^{(g)}\partial_x \mathbf{U}^{(g)}$, in Fig. 1.13b and Fig. 1.14b, respectively. Beyond the immediate nozzle region, the magnitudes of β_{NFD} quickly relax to much lower values $\sim \mathcal{O}(10^{-2})$ indicating that from a linearly stability analysis perspective they can be neglected to a reasonable approximation. It is actually the non-linear term, which grows quickly and is *primarily responsible for invalidating* the assumptions employed in the stability analysis.

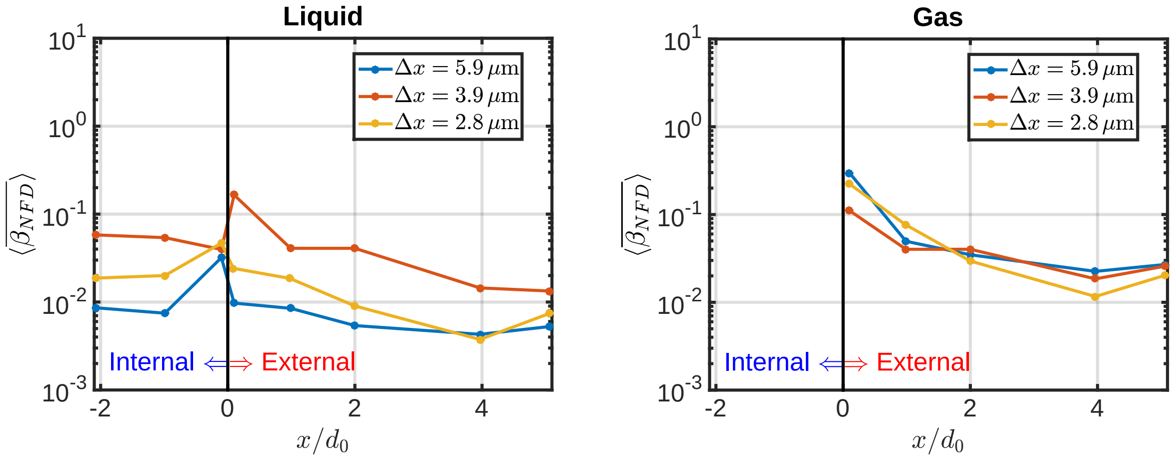

(a) (b)

Figure 1.14: Magnitude of axially-developing term in the (a) liquid phase and (b) gas phase.

1.7.2 Surface Disturbances

The conventional view of the spray formation process embodied in spray models [2, 14, 46, 68, 74, 77] consists of a liquid, which is initially perturbed by a multitude of infinitesimal axisymmetric perturbations, and where the fastest growing mode (governed by linear stability analysis) emerges to dominate the disturbances. This fastest and most violent mode grows beyond the initial sinusoidal characterization and is then responsible for the breakup of the liquid jet, i.e. it produces primary atomization. It is tacitly assumed that during this process of surface growth from sinusoidal to highly erratic surface shape, the underlying flow field is similarly undergoing a transition into the full non-linear regime.

We contrast this view by observing the results of simulations as depicted in Fig. 1.15 over four different axial orientations. Over a distance of approximately 5 diameters from the orifice, the surface disturbances are highly irregular with strong asymmetries, which are far from the expected axisymmetric normal mode [57]. However, the magnitude of these disturbances is significantly smaller than the jet diameter, and most of them are still single value functions of the radial coordinate (the interface has not folded over itself).

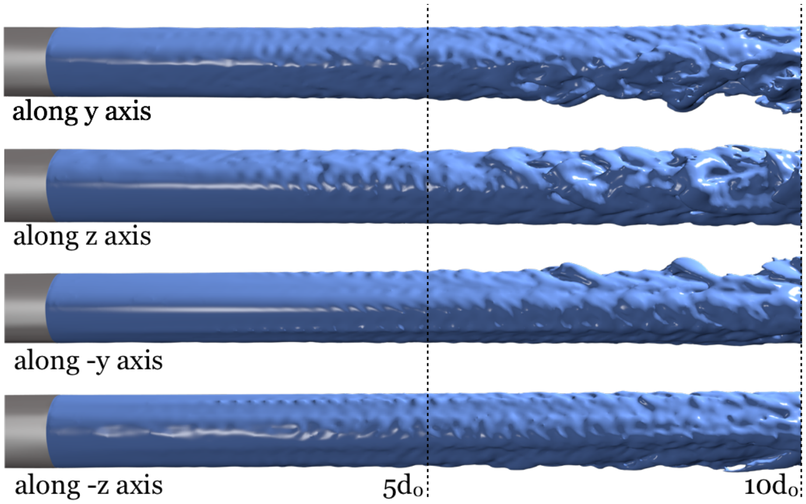

Figure 1.15: Near field (up to $x = 10d_0$) jet surface morphology from four different viewing orientations. A view along the y axis is shown at the top followed by three other views (sequential rotations of 90° about the x axis).

In the work of McCarthy and Molloy [45], it is discussed that as the flow exits the nozzle, thereby losing the wall constraint, turbulent lateral motion of the fluid leads to surface disturbances. In addition to the loss of the wall constraint, complex flow development inside the nozzle due to surface irregularities and non-symmetrical orifice shape are likely to blame for the observed level of interface irregularity. These near-nozzle irregularities have also been reported in recent experimental visualization as well [17, 26, 32]. The images in Fig. 1.15 reveal that the surface is characterized by the presence of disturbance streaks aligned along the streamwise direction. And that slightly beyond $x/d_0 = 5.5$, the surface show signs of developing lobes, which force the surface to fold over itself and become a multivalued function of the radial coordinate.

To visualize more clearly the evolving complexity of free surface disturbance within the range $4.5 < x/d_0 < 8$ in a cross-sectional x-y plane containing the centerline, the instantaneous free surface is compared to a Fourier fit (8 modes) in Fig. 1.16. While the surface remains a single value function of r at $x/d_0 < 5.5$, it distinctly loses this quality at $x/d_0 \approx 7.7$. Similar lobe structures have also been identified in the liquid jet and liquid sheet simulation work of Sirignano and co-workers [30, 78]. At $x/d_0 \simeq 5$, Section 1.7.1 has already established that the non-linearities have developed beyond 10% of its linear counterpart. We see that this departure coincides with a significant level of surface deformation, which is far more complex than the axi-symmetrical disturbances predicted by linear theory.

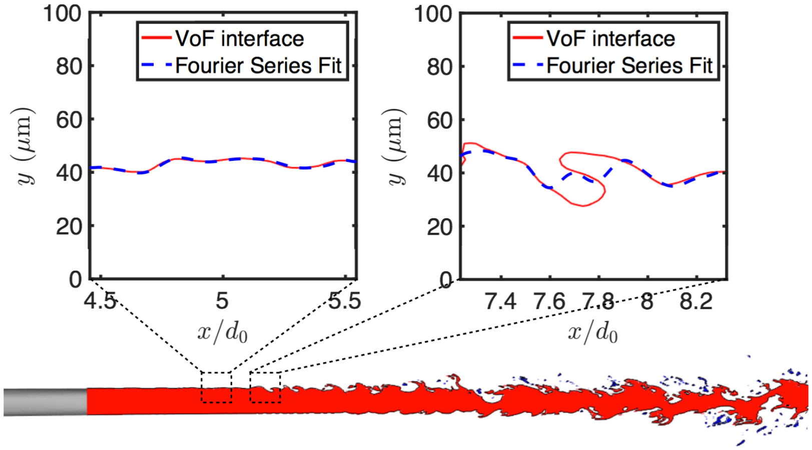

Figure 1.16: A cross sectional view of the near field is presented at the bottom. The two insets display the VoF interface at two axial locations along with a Fourier series fit (8 modes) through the interface data suggested by the mathematical form given in Eq. (1.26). In the first inset the wave amplitudes are small and the interface can be represented well by a sum of sinusoidal modes. As we move downstream the interface is no longer represented by a single-valued function of r.

1.7.3 Comparison between VoF and Linear Stability

Close to the injector orifice, specifically for $x/d_0 \leq 5$, the non-linearities are small enough that a comparison can be made between the VoF simulation results and those stemming from a linear stability analysis. It should be kept in mind that the complexity of the flow emanating from the nozzle after its passage through its interior is significantly more complex from the standard base flow fields presented in texts [23, 63] and subsequently analyzed via the Orr-Sommerfeld equation. Hence, we should not expect to arrive at a perfectly consistent comparison; nevertheless, for the sake of estimating the associated dominant wavelengths, it is instructive to perform this investigation.

The two-phase Orr-Sommerfeld solution is computed from a previously published procedure by Deshpande et al. [21], where all dynamic and kinematic interfacial conditions are enforced. Additionally, the base liquid and gas phase boundary layers are obtained from the current simulations. To allow for uncertainties between these boundary layer thickness values, different variations are considered, and the corresponding wavelengths for the most violent modes are presented in Table 1.7.

		δ_L		
		7 μm	10 μm	15 μm
δ_G	7 μm	40.8 μm	57.1 μm	81.6 μm
	10 μm	40.8 μm	58.3 μm	81.6 μm
	15 μm	40.8 μm	58.3 μm	87.4 μm

Table 1.7: Wavelenghts of most unstable modes from OS calculations.

To estimate the wavelengths of the surface disturbances from the VoF simulations, various probes are placed within $4 < x/d_0 < 5$. As seen in Fig. 1.15 and documented in Section 1.7.1, this region of the domain places the surface disturbances well within the linear regime. Time history of the interface perturbation is presented in Fig. 1.17. The interface perturbation, denoted as $\xi(x = 4d_0, z = 0)$ for instance, is the distance of the interface from its unperturbed location, $(x = 4d_0,\ y = 45\,\mu\text{m},\ z = 0)$. Similarly, $\xi(x = 4d_0, y = 0)$ is the distance of the interface from its unperturbed location, $(x = \ 4d_0,\ y = 0,\ z = 45\,\mu\text{m})$.

The $\xi(x, z = 0, t)$ and $\xi(x, y = 0, t)$ data is then analyzed in the frequency domain through a Fast Fourier Transform. The underlying flow field predictions from VoF are interrogated revealing that the surface disturbances are traveling at $U_\xi = 412$ ms^{-1}, and this velocity is largely constant in time. Therefore, the wavelengths associated with the frequencies are obtained as $\lambda = U_\xi/f$.

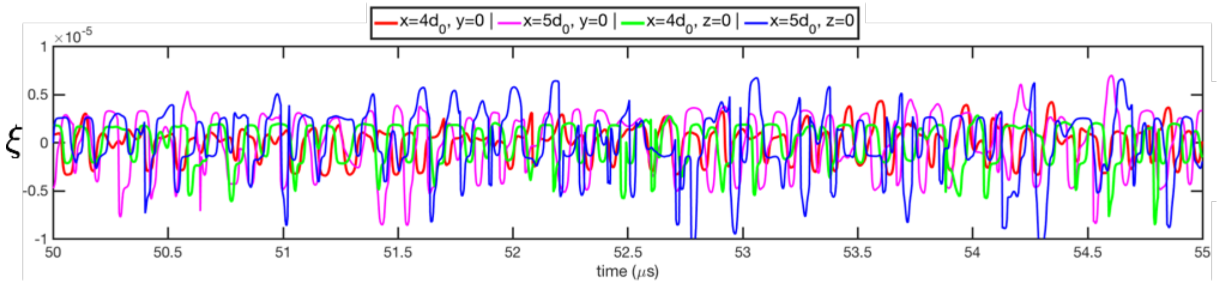

Figure 1.17: Interface perturbation, ξ, is presented as a function of time in the x-y plane and x-z plane, at two axial locations, $x = 4d_0$ and $x = 5d_0$.

The resulting wavelength spectra for the data is presented in Fig. 1.18. It is observed that the most dominant modes, defined here as the modes with amplitudes within 20% of the maximum amplitude, are in the range of $\lambda = 40.4\,\mu$m to $\lambda = 71.0\,\mu$m.

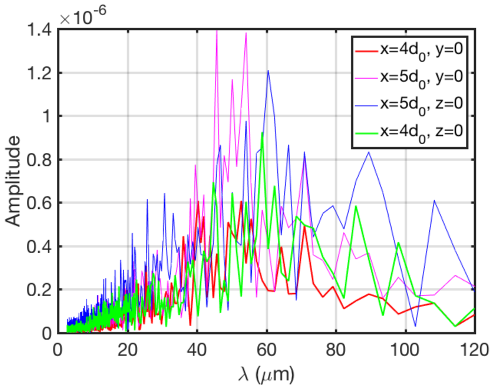

Figure 1.18: Frequency spectra for interface elevation data from $z = 0$ plane and $y = 0$ plane.

The Orr-Sommerfeld growth spectra, obtained as described in [21], are shown in Fig. 1.19. Dominant modes from the VoF simulations are overlaid on the plot as a band. The fastest growing modes from the OS calculation are in the range of $40.8\,\mu$m to $87.4\,\mu$m, and those from the VoF simulations are in the range of $40.4\,\mu$m to $71.0\,\mu$m. A strong overlap between the OS prediction and the simulation data indicates that linear stability theory predicts relatively well the wavelengths of the most unstable modes in a realistic liquid injection setup.

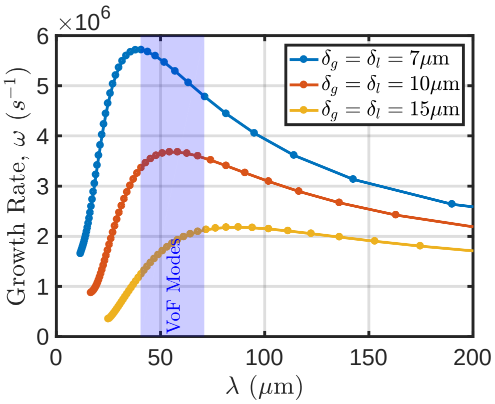

Figure 1.19: Orr-Sommerfeld growth spectra for 3 different velocity profiles, where δ_G and δ_L represent the gas and liquid boundary layer thicknesses, respectively. From Table 1.7, the O-S predicts that the most unstable modes lie between 40.8 μm to 87.4 μm. The most unstable modes detected in the VoF simulations lie in the region highlighted in blue.

1.7.4 Implications for Primary Atomization

To provide an insightful perspective of the internal structure of the liquid jet, various cross-sectional views of liquid fraction field (α) are displayed in Fig. 1.20. Each of these views corresponds to a plane that intersects the jet centerline. The images reveal that while the surface of the jet begins to display breakup at $x/d_0 \approx 7$, the underlying liquid core remains intact. Due to the asymmetric flow emanating from the nozzle, the level of surface disintegration is not uniform along the azimuthal coordinate with some sections of the jet showing more vigorous breakup than other sections at the same axial location. However, by $x/d_0 \approx\ 8$, the surface is already breaking up all around the jet. This relatively near nozzle location for breakup is much closer than the location where the entire jet breakups, or by definition the location of primary atomization. In Chapter 2, Fig. 2.10 presents a time history of the length of the intact liquid core for the different nozzle configurations, which provides instantaneous information of the primary atomization region. For the nozzle considered here, it lies approximately between $x/d_0 = 30$ and $x/d_0 = 40$, with a mean value of $\overline{x/d_0} = 37.8$.

The fact that the flow has become highly non-linear and that the surface of the jet undergoes breakup relatively close to the nozzle is in contrast with the fact that the liquid core remains intact

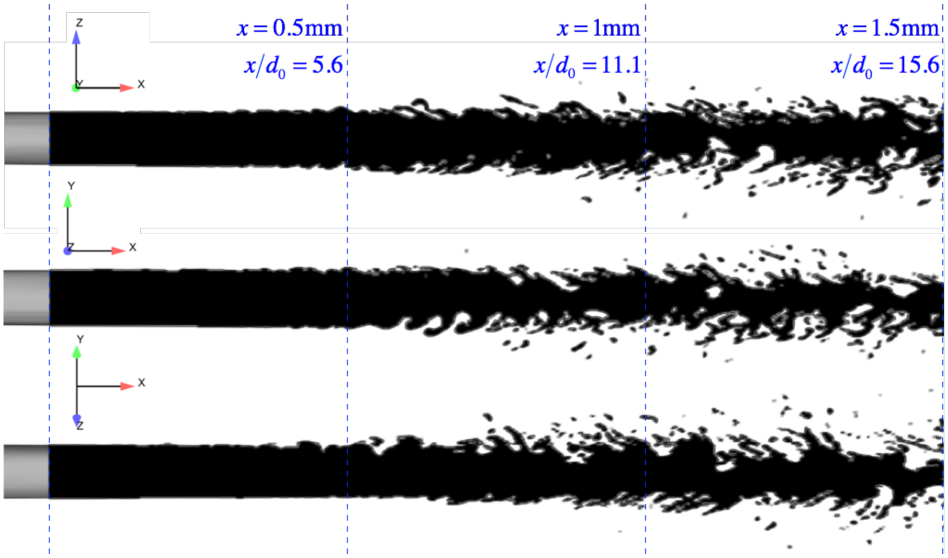

Figure 1.20: Computational images of the near-field jet breakup corresponding to orientations along the y-axis, z-axis, and midpoint point axis between the z and y axes. The images show surface breakup beginning at $x/d_0 \approx 7$.

until much further downstream. This observation calls to question the conventional view of the atomization process [41, 42, 58], inherited widely in spray models, where the most unstable mode predicted by linear stability analysis is viewed as the responsible agent for completely fragmenting the liquid jet.

The current simulations and analysis show that the most unstable modes do exist under the present conditions, but that their action is limited to the breakup of the surface of the jet, not in cutting it off completely. Hence, *they are not directly associated with primary atomization.* This is also in agreement with previous observations presented for the case of an injected liquid sheet [21], where it was reported that the most unstable OS modes have length scales that are two to three orders of magnitude smaller than the sheet thickness and are thus responsible for atomizing the surface of the sheet, but not the sheet itself. Similar findings have been reported by Marmottant and Villermaux [43] and Rayana [11], albeit under significantly different configurations. Marmottant and Villermaux employed a coaxial jet arrangement, and Rayana used an airblasted liquid sheet, but both reported an initial instability followed by a secondary one responsible for primary atomization.

Fig. 1.21 presents an illustration of the process.

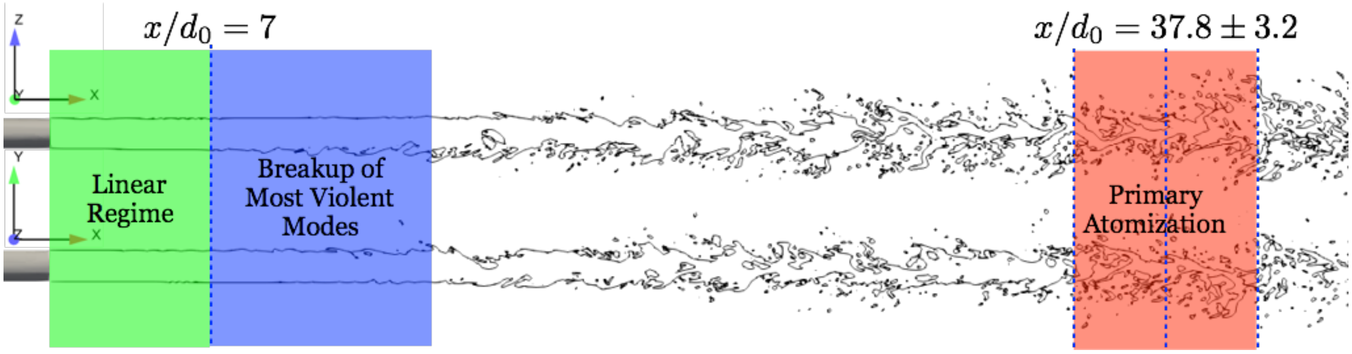

Figure 1.21: Two instantaneous images of the jet breakup, with viewing directions oriented along the y and the z axis, are presented here. The image highlights 3 distinct parts of the atomization process. Linear modes of the surface disturbances exist initially up to $x/d_0 = 7$. Further downstream, the dominant modes grow and breakup the surface, but the liquid core remains unpreturbed. Finally primary atomization, or the complete destruction of the liquid core is observed around $x/d_0 = 37.8$.

1.8 Conclusions

After successfully comparing high-resolution simulation data to recent X-ray radiography measurements [34, 76], the extent of the linearity treatment and accompanying assumptions in spray models is investigated. It is found that non-axial flow and non-fully developed conditions are present right at the orifice location, but that these do not show signs of significant growth (exponential). It is actually, the non-linear flow development that exhibits the greatest and sustained growth, where it is shown that at 4 diameters downstream, it is already approximately 10% of the linear advection part. Similarly, the conventionally assumed sinusoidal surface disturbances are largely absent, and the surface of the jet is irregularly distorted right from the start of the external domain. These disturbances lead to interface folding over itself at $x/d_0 \approx 7$ and subsequent formation of small ligaments and drops. Due to the real flow conditions emanating from the orifice, as opposed to idealistic conditions of steady and spatially uniform flow, these characteristics are expected.

Comparing the wavelength of the most unstable modes between the OS linear stability predictions and VoF simulations, the results show reasonably agreement being mindful of the fact that the real base flow field is not the same as the conventional one adopted in OS analysis. Even though these initial disturbance modes are clearly the most unstable, they are not sufficiently large to completely rupture the jet. Their impact is limited to stripping off the surface of the liquid jet, while the jet core remains unperturbed. This surface stripping is found to start somewhere between $x/d_0 = 7$ and $x/d_0 = 10$, whereas the jet core undergoes complete atomization at a mean value of $x/d_0 = 37.8$, i.e. approximately 30 diameters downstream. A subsequent mode develops once the flow has become fully-nonlinear, and it is this more violent process that leads to primary atomization. Similar observations have been reported in the literature for liquid sheet undergoing atomization [21] and for a liquid jet in a co-axial configuration exposed to a fast moving air stream [43].

A key outcome from this chapter questions the validity of the common spray model assumptions linking linear stability with primary atomization, at least for realistic cases such as the present one using Spray A. A related question centers on the level of agreement typically reported between spray model predictions and experiments concerning liquid penetration vs. time. This level of error is usually well below 5%, which would tend to confirm the applicability of linear stability theory. However, it should be kept in mind that the practical application of this theory is combined with the introduction of a good number of modeling constants [58], and that these constants have been fined-tuned over the years to match experimental data. Thus, the level of agreement reported is not really a validation of linear stability theory, but rather a confirmation that the constants have been appropriately optimized.

Similar conclusions questioning the validity of the linear stability rooted in the KH analysis and its adoption into breakup models have recently been presented by Kastengren et al. [32]. Their reasoning revolved around the absence of nano-scale droplet population in their measurements, which is predicted by KH. This extremely small droplet size distribution emanates from an infinitely sharp boundary layer at the interface, i.e., a discontinuous velocity field. In fact, predictions from the more general OS [21], which includes viscosity effects, reveal that as the boundary layer is thickened the length scale of the most unstable mode, and the associated droplets emanating from them, grow noticeably in size. Hence, we can have droplets of much larger size than the KH generated nano-droplets, but the dynamics can still be completely governed by the breakup of the most unstable modes of linear stability theory. What the present work suggests is that even these larger scales disturbances predicted by linear stability theory do not fracture the liquid core. Their influence is restricted to the surface.

Chapter 2

Effect of Internal Nozzle Flow on Primary Atomization

2.1 Background and Motivation

In liquid spray applications, flow development inside the injector nozzle is crucial to the spray dynamics, specifically to the breakup of the initially continuous liquid jet [45, 64]. However, the internal flow and its effect on the liquid breakup are not well understood due to complexities arising from nozzle geometry, needle motion, turbulence, and flow cavitation. Therefore, the study of nozzle effects on spray formation remains an active area of research [9, 19, 22, 52, 62].

Capturing all the details of in-nozzle turbulence is computationally challenging. While much of previous work has been done on tuning and evaluating the different turbulence models [12, 48, 62], fewer studies focus on characterizing or analyzing the turbulence itself, owing to the computational challenges. Among some recent studies, Jiao et al. [31] attempt to characterize and study the effect of nozzle turbulence by obtaining turbulence data from DNS simulations of fully developed pipe flow, and using the time-varying velocity data as input for their atomization simulations. They report three different types of liquid structures, namely, long, flat and curly, separating from the liquid jet at different axial locations. Moon et al. [47] show the effect of the orifice inlet geometry on the velocity gradients and the turbulence intensity inside the nozzle through X-ray-imaging data. They also establish connections between the velocity gradients and the turbulence intensity. They find that the spray deceleration is linked with the increase in turbulence intensity. Salvador et al. [61] provide hydraulic characterization with respect to different levels of needle lift through simulations of internal nozzle flow. They show how needle lift affects the turbulence development within the nozzle which impacts the subsequent breakup. Chouak et al. [15] have performed transient simulations and analysis with respect to continuous needle lift. They provide an explanation for hysteresis with respect to needle motion and find that needle motion is one of the most important factors that affects in-nozzle turbulence.

Among the studies that deal with in-nozzle cavitation, Lee & Reitz [40] show that fast closing of the needle can result in cavitation and conclude that there is some optimal lift profile in the needle movement through numerical investigation of injector nozzle flow. In their comparative experimental study across different nozzle geometries, Payri et al. [52] find that convergent nozzles do not present cavitation, and that the spray momentum is not affected by cavitation. Arienti & Sussman [8, 9] demonstrate an effect similar to cavitation via computations. They find that the ambient gas is ingested into the nozzle before the start of injection. This leads to a non-uniform filling of liquid inside the nozzle and impacts atomization behavior.

Although much of the literature [22, 45, 64] has established that internal nozzle flow is critical to the disturbance and subsequent breakup of the issuing liquid jet, very little work, if any, has reported on the effect of nozzle asymmetries and surface imperfections on primary atomization. The present work is aimed at addressing these open questions by first providing a quantitative characterization of the nozzle surface geometry. This is followed by detailed Volume-of-Fluid (VoF) simulations where the internal and external flow is fully-coupled. This is in contrast to the decoupled simulations where internal nozzle flow is computed and provided as an inflow boundary condition to the spray simulation [31]. The goal is to demonstrate the sensitivity of internal nozzle flow characteristics, near field liquid jet characteristics, and primary atomization behavior to differences in the nozzle surface features. Our scope is within the quasi-steady period of injection, i.e., beyond the initial transient. We additionally employ an incompressible strategy in simulating the fluid mechanics. While this imposes some degree of inaccuracy in the simulations under the present conditions, our present objective is to take an initial step in analyzing the fluid mechanics and atomization at the current level of detail before embarking in more general approaches. An important discovery from the present work concerns the significant role that the mean non-axial flow (inside the nozzle) plays in the atomization characteristics. While some studies have tried to characterize the axial flow profiles [12, 15, 62], no studies to the author's knowledge investigate the non-axial velocity components.

An important discovery from the present work is regarding the significant role the steady (non-fluctuating) flow, specifically the steady non-axial flow, inside the nozzle plays in the atomization characteristics. While some studies have tried to characterize the axial flow profiles [12, 15, 62], no studies to the author's knowledge investigate the non-axial velocity components. We find that the steady non-axial velocity components are small in magnitude but have a significant impact on atomization.

2.2 Results

The results are presented in five parts. Section 2.2.1 discusses the mean velocity profiles inside the nozzle, and Section 2.2.2 examines the growth of disturbances on the liquid surface as the fluid moves downstream from the nozzle orifice. The turbulent kinetic energy and the magnitude of the transverse velocity is discussed in Section 2.2.3. In Section 2.2.4 we describe the bulk atomization characteristics through a characterization of the liquid core fragmentation. Finally, in Section 2.2.5 we formally examine the grid convergence characteristics for the metrics provided in this chapter.

2.2.1 Internal Flow

The instantaneous velocity can be decomposed into a mean velocity and a perturbation velocity given respectively by $\mathbf{u} = \langle \mathbf{u} \rangle + \mathbf{u}'$ according to the standard Reynolds decomposition. While the flow is predominantly along the nozzle axis, it is helpful to isolate the non-axial component, namely

$$\mathbf{u}_\perp = \mathbf{u} \cdot (\mathbf{I} - \mathbf{e}_x \mathbf{e}_x), \tag{2.1}$$

where $\mathbf{e}_x$ is a unit vector along the axial direction. Results for $\langle \mathbf{u}_\perp \rangle$ at the finest grid resolution are presented in Fig. 2.1a and Fig. 2.1b at the orifice exit plane ($x = 0$) for the Spray A geometries. There is a striking difference between the flow in the Educated and the Unprocessed Spray A; higher magnitudes of $\langle \mathbf{u}_\perp \rangle$ are observed in the Unprocessed Spray A. These higher magnitudes are concentrated near the nozzle walls mainly because the flow in this region is susceptible to small but abrupt changes in direction. Due to the high-speed velocity in the axial direction, a non-negligible change in the flow direction due to nozzle surface features leads to an appreciable non-axial velocity component. Additionally, the flow asymmetry further accentuates this process.

Moreover, it is observed that there are discernible flow structures in the averaged velocity field. It should be emphasized that these flow features represent *converged temporal averages*; these are *not* instantaneous structures. The implication is that regardless of the turbulent fluctuations, the underlying velocity field itself departs significantly from the canonical symmetric profile in a purely circular inlet. Persistent (time-invariant) and organized flow structures are set up inside the nozzle. To illustrate the complexity of the flow, color maps of vorticity are also shown in Fig. 2.1c and Fig. 2.1d to display the degree of structure that the internal flow has at the nozzle exit. This data is also presented at the finest grid resolution.

As the jet exits the nozzle, the velocity component normal to the interface plays a direct role in the subsequent atomization behavior. For canonical flows such as the external-only case considered, that velocity component normal to the interface is zero. However, for more realistic flow cases,

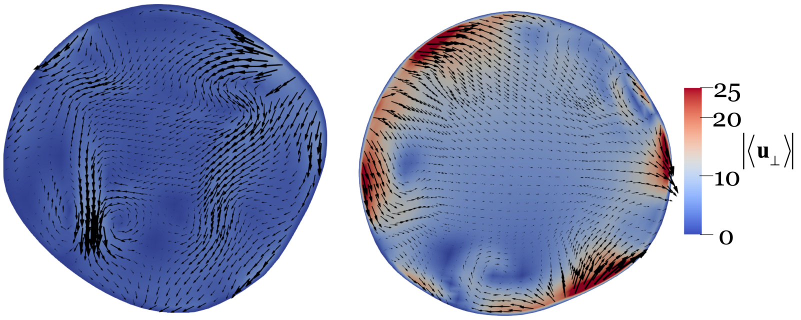

(a) $\langle \mathbf{u}_{\perp} \rangle$ for Educated Spray A

(b) $\langle \mathbf{u}_{\perp} \rangle$ for Unprocessed Spray A

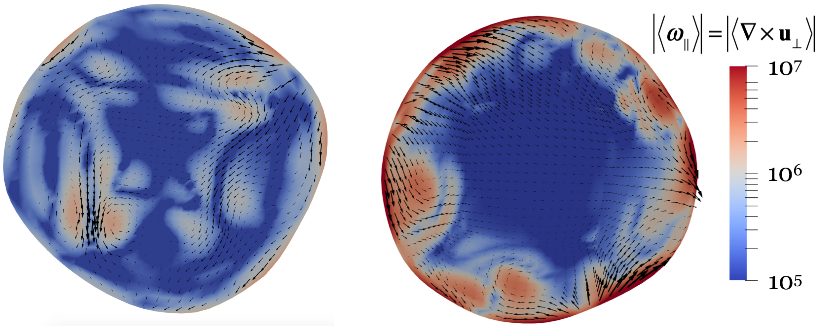

(c) $|\langle \boldsymbol{\omega}_{\parallel} \rangle|$ for Educated Spray A

(d) $|\langle \boldsymbol{\omega}_{\parallel} \rangle|$ for Unprocessed Spray A

Figure 2.1: Contours of the time averaged, transverse velocity magnitude, $\langle \mathbf{u}_{\perp} \rangle$ and the time averaged vorticity magnitude $|\langle \boldsymbol{\omega}_{\parallel} \rangle|$ are presented at the orifice opening ($x = 0$) for the two Spray A geometries. The color bars appear in SI units. The vector arrows represent the $\langle \mathbf{u}_{\perp} \rangle$ vectors.

such as the Unprocessed and Educated geometries this component is not zero and represents an instantaneous protrusion of liquid, which directly influences atomization. The contributions from this non-axial component can be approximated very well by the radial velocity, u_r, since the orifice opening is sufficiently close to circular for both the Educated and Unprocessed geometries.

To get a sense of the radial velocity characteristics, $\langle \mathbf{u}_r \rangle$, Fig. 2.2 plots the distribution of $\langle u_r \rangle$ across the $x = 0$ plane, where $u_r = \mathbf{u}_r \cdot \mathbf{e}_r$. The Unprocessed Spray A nozzle has a wider distribution, i.e., exhibits higher magnitude values of $\langle u_r \rangle$ supporting the observations from Fig. 2.1.

Fig. 2.3 shows the $\langle \mathbf{u}_{\perp} \rangle$ contours inside the nozzle at different axial locations, along with the liquid jet emerging from the nozzle. While the velocity field shown here is time-averaged, the

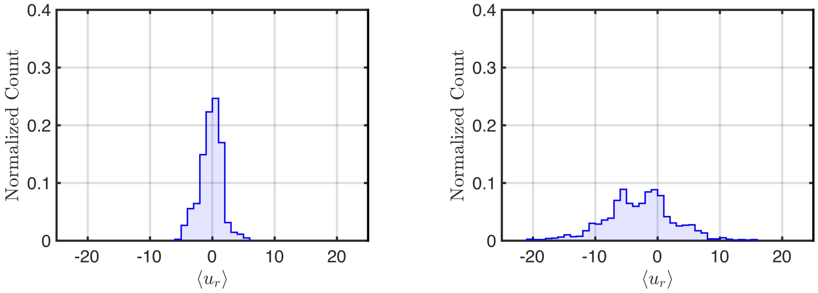

(a) Educated Spray A (b) Unprocessed Spray A

Figure 2.2: The time averaged, radial velocity component, $\langle u_r \rangle$, at the exit of the orifice is presented as probability distributions for the two Spray A configurations at the finest resolution. The velocities are shown in m/s units. Higher magnitudes of $\langle u_r \rangle$ are observed in the Unprocessed Spray A geometry.

liquid-gas interface presented is instantaneous for ease of interpretation (the time-averaged liquid distribution is presented subsequently in Fig. 2.6). We find that this pattern of a larger magnitude of the non-axial velocity in the Unprocessed Spray A nozzle holds further upstream as well, i.e., into the nozzle. Concerning the liquid surface, apart from the surface fluctuations that grow along the flow direction, an interesting feature is the presence of protrusions or striations along the liquid jet. Production of these striations is most pronounced in the Unprocessed Spray A geometry followed by the Educated Spray A geometry. The external-only flow has no non-axial velocity component at the orifice opening, therefore, no such protrusions are recorded in this case, as expected.

To examine the connection between the mean internal flow and the liquid surface striations, we consider two (Lagrangian) fluid particles located on the intersection of the nozzle exit plane and the gas-liquid interface at precisely the source of two striations, respectively. This is illustrated in Fig. 2.4. The motion of these fluid particles is described by,

$$\frac{\mathrm{d}\mathbf{X}(t)}{\mathrm{d}t} = \mathbf{u}(\mathbf{X}_\Gamma(t), t), \tag{2.2}$$

where the subscript, Γ, denotes interface location. Since we are interested in the protrusion of liquid

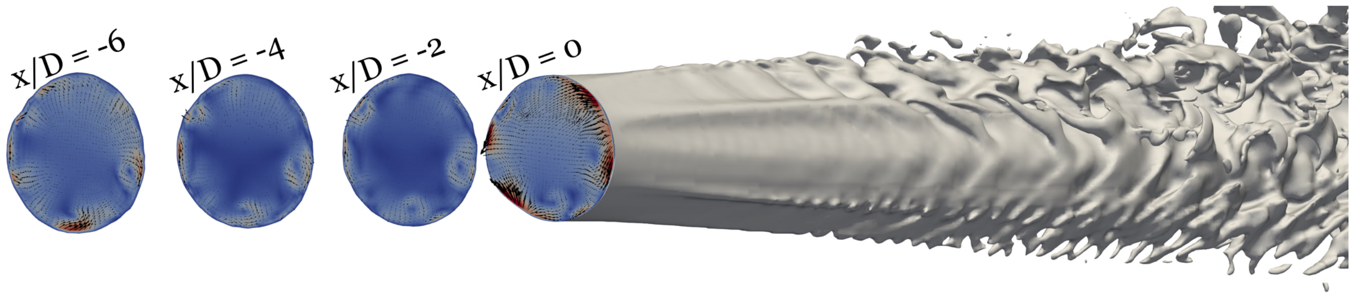

(a) Unprocessed Spray A

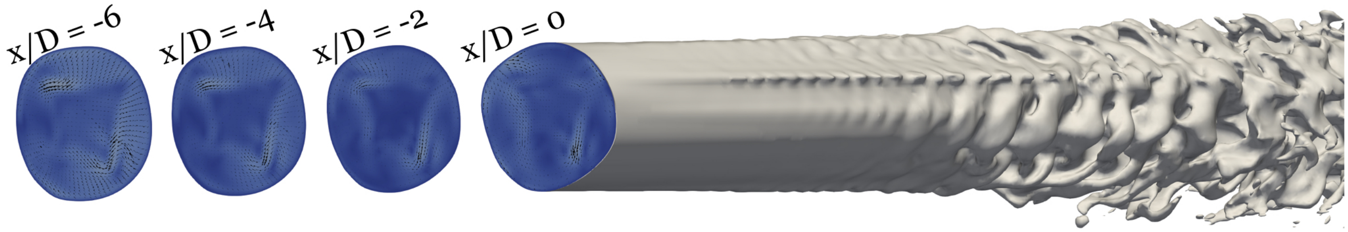

(b) Educated Spray A

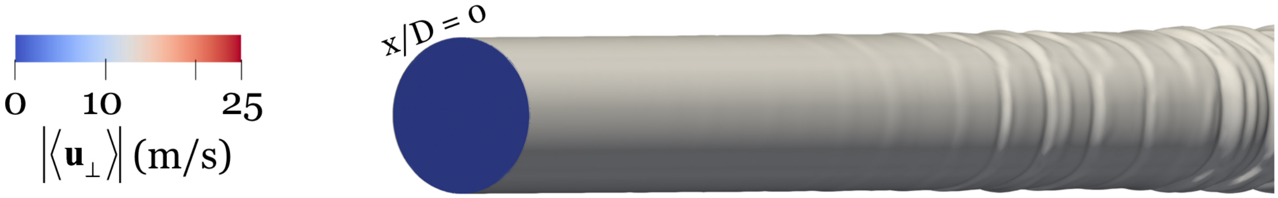

(c) External-only

Figure 2.3: Contours of the time averaged, non-axial velocity, $\langle \mathbf{u}_\perp \rangle$, are shown at different locations inside the nozzle orifice along with a part of the liquid jet surface. The differences between the internal flow and the liquid surface shape between the configurations is evident. The higher magnitudes of $\langle \mathbf{u}_\perp \rangle$ lead to prominent striations on the liquid jet surface.

at this location, the radial component is isolated from the previous expression giving

$$\frac{\mathrm{d}R(t)}{\mathrm{d}t} = u_{r,\Gamma}(\mathbf{X}(t), t). \tag{2.3}$$

The motion of two fluid particles, α_1 and α_2, is highlighted in Fig. 2.4. At t_0 both particles start at the orifice opening and their locations are shown at two subsequent times, t_1 and t_2. A dotted line is added to the figure to indicate the respective particle paths. The motion of these particles normal to the liquid surface, i.e., motion in the radial direction, leads to a displacement of the liquid surface.

Further downstream, these striations appear to coalesce producing an even more pronounced radial displacement. While fluctuations are present in the disruption of the liquid jet surface, the fact that a significant part of this motion stems from an averaged flow field underscores the importance that mean quantities have in creating liquid jet asymmetries and in the overall breakup behavior as examined in the following sections.

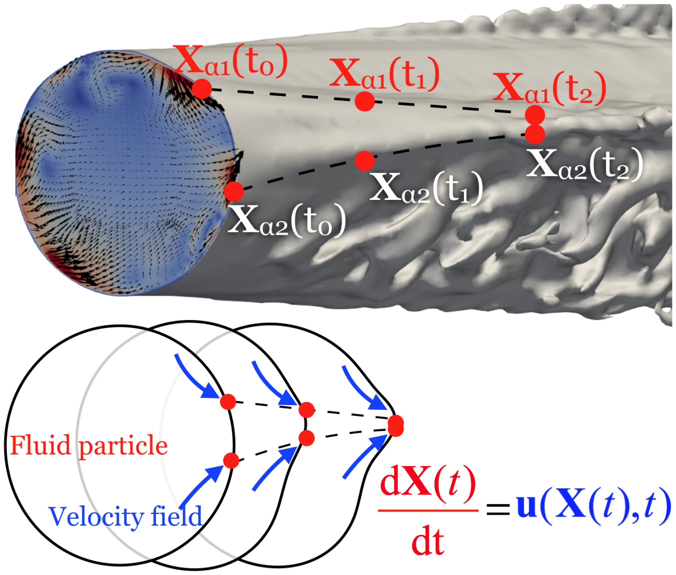

Figure 2.4: An illustration of the formation of striations on the liquid jet surface. The passive Lagrangian trackers are shown by the red dots and their trajectories are marked by the dotted lines. The underlying velocity field is shown by the blue arrows. An initially circular liquid jet deforms under the action of the non-axial velocity component and permanent striations appear on the liquid surface.

2.2.2 Interface Displacement From Base Shape

Fig. 2.5 and Fig. 2.6 provide a visualization of the near field liquid distribution using the instantaneous liquid fraction (α) contours and the time-averaged liquid fraction ($\langle\alpha\rangle$) contours, respectively. Inside the nozzle ($x < 0$) the mean values for the non-axial velocity, $|\langle\mathbf{u}_\perp\rangle|$ are presented in both figures. The data is presented for the finest grid resolution cases. The smearing of the $\langle\alpha\rangle$ contours in Fig. 2.6 corresponds to the degree of fluctuation of the liquid surface. Significant differences are observed among the three configurations in both figures. More importantly, in Fig. 2.6 the more disturbed flow field corresponding to the Unprocessed geometry shows a larger degree of liquid core disintegration even as close as $x/D_0 = 8$. The disturbance of the liquid core is also observed for the Educated Spray A nozzle but to a lesser extent. This behavior is consistent with the striations on the surface observed earlier. For the external-only flow, where $\mathbf{u}_\perp = \mathbf{0}$ at the inlet plane, the liquid mass distribution remains largely cylindrical.

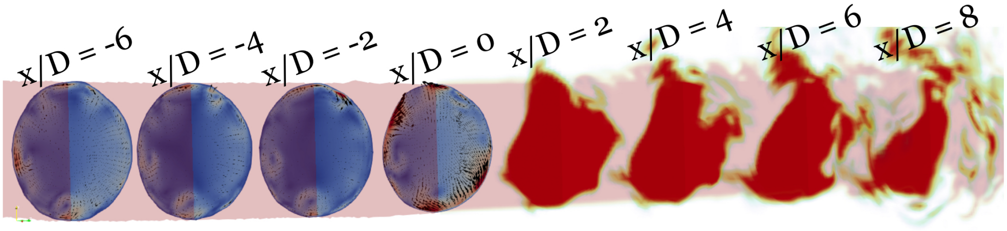

(a) Unprocessed Spray A

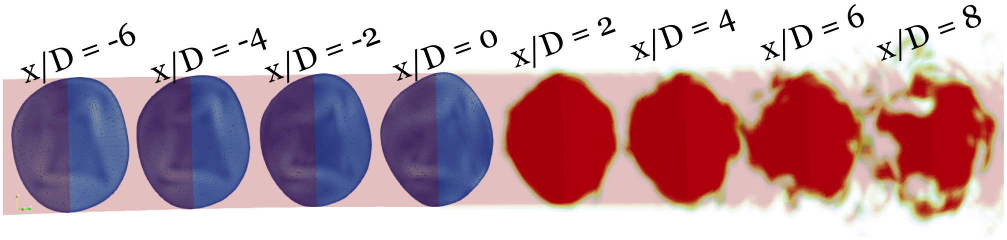

(b) Educated Spray A

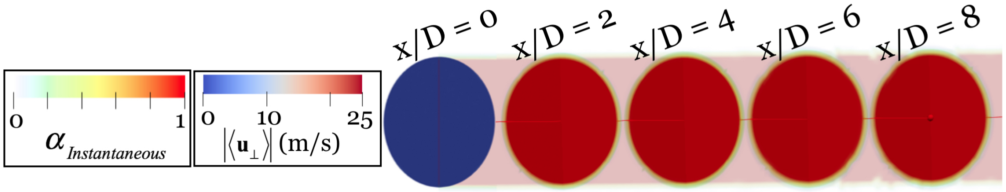

(c) External-only

Figure 2.5: Contours of the instantaneous, liquid volume fraction field α, are shown at different locations in the external flow region ($x > 0$) and contours of the time averaged, non-axial velocity, $\langle \mathbf{u}_\perp \rangle$, are shown at different locations inside the nozzle orifice ($x < 0$). Significant differences are observed in the liquid distribution among the three configurations.

To quantify the degree of surface perturbation, we define the radial location of the jet, $R(\theta, x, t)$, as the distance between a point on the surface of the jet along a line of constant θ and the axis of the jet at the same axial location x. At the base of the jet, i.e., $x = 0$, this radial location is not a

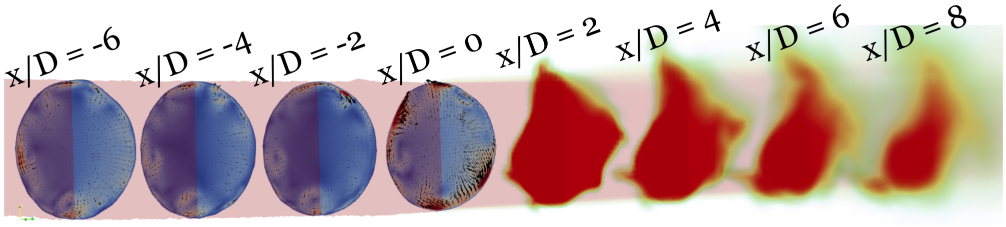

(a) Unprocessed Spray A

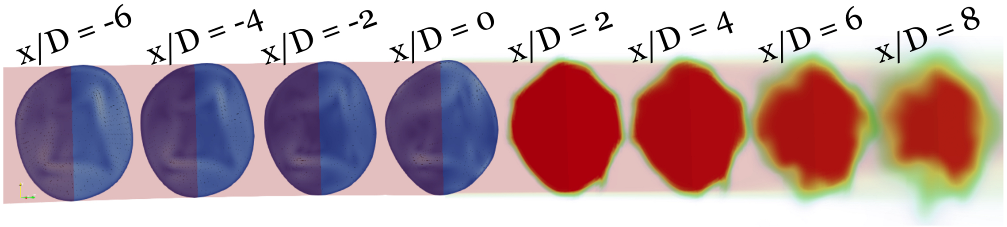

(b) Educated Spray A

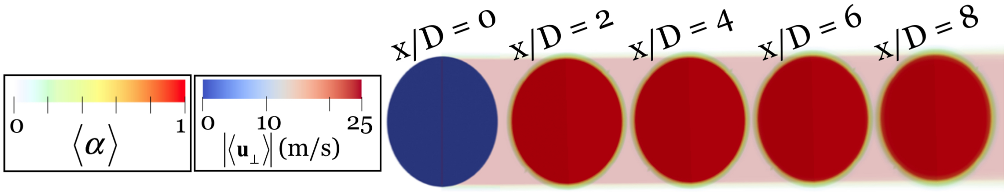

(c) External-only

Figure 2.6: Contours of the time averaged, liquid volume fraction field $\langle\alpha\rangle$, are shown at different locations in the external flow region ($x > 0$) and contours of the time averaged, non-axial velocity, $\langle\mathbf{u}_\perp\rangle$, are shown at different locations inside the nozzle orifice ($x < 0$). Significant differences are observed in the liquid distribution among the three configurations.

function of time since the surface of the jet coincides directly with the nozzle orifice, and the flow exiting is 100% liquid. We denote this base shape as $R_o(\theta)$, which can be subsequently employed to calculate a surface displacement as

$$\xi(\theta, x, t) = |R(\theta, x, t) - R_o(\theta)|. \tag{2.4}$$

Some representative results are shown in Fig. 2.7 at $t = 50\,\mu$s, where the jet surface is colored by $|\xi(\theta_i, x_j, t = 50\,\mu\text{s})|$. The inset shows a single slice of this jet at $x = 3.3D_0$. This image illustrates the level of disturbance in the liquid surface as a function of the axial coordinate, x, and the azimuthal angle, θ. To calculate an overall rate of displacement from the base shape, we discretize the spatial variables and compute the temporally and azimuthally averaged value as

$$\overline{\langle \xi(x_j) \rangle} = \frac{1}{n_\theta} \sum_{i=1}^{n_\theta} \langle \xi(x_j, \theta_i) \rangle \,. \tag{2.5}$$

In the case where more than one interfacial point is encountered along the constant θ line, the point recorded in this calculation corresponds to the closest one to the jet axis.

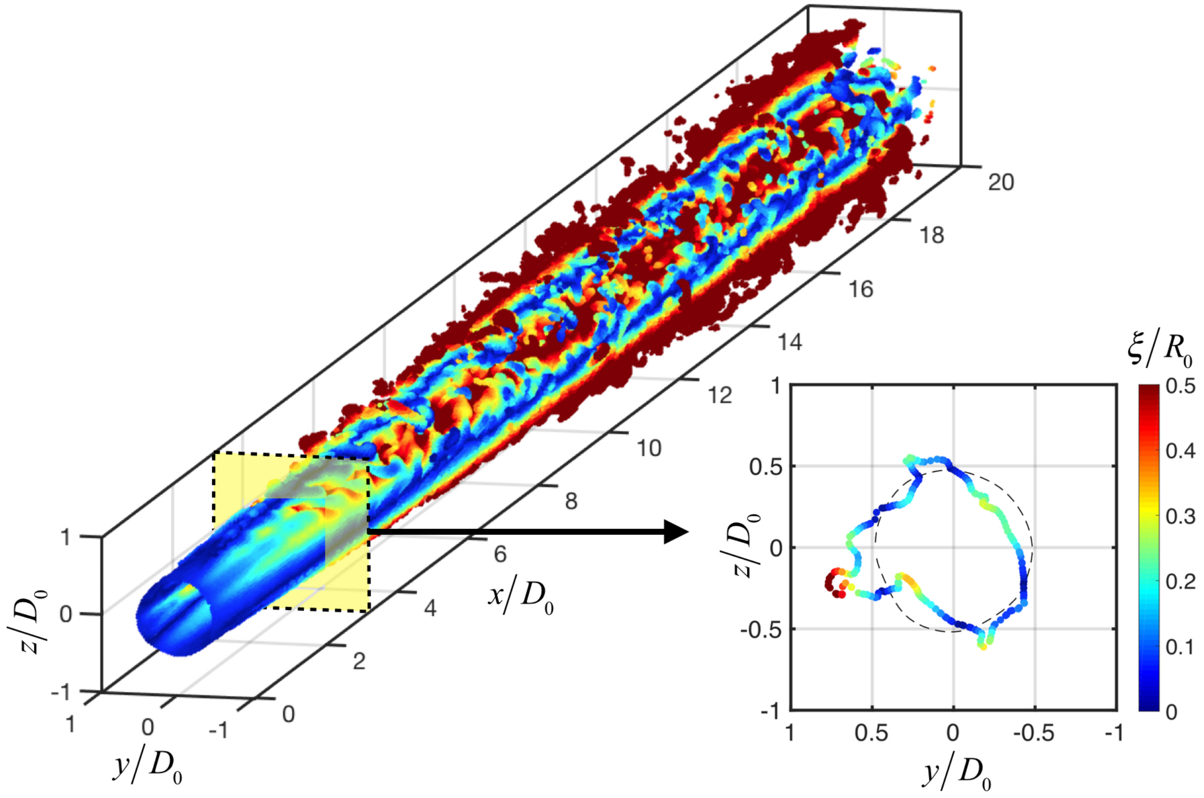

Figure 2.7: The surface of the liquid spray for the Unprocessed Spray A configuration is shown to the left. A slice of this surface at $x/D_0 = 3.3$ is shown in the inset. The dashed line in the inset represents the base surface, $R(x = 0, \theta)$, i.e. the shape of the orifice opening. ξ is the distance of the surface points from this base surface. The liquid surface points are colored by the magnitude of the disturbance, ξ.

The $\overline{\langle \xi(x_j) \rangle}$ trends for the different cases are shown in Fig. 2.8, which display a nearly linear increase in the mean displacement with distance downstream. The values of $\overline{\langle \xi(x_j) \rangle}$ among the different grid levels for the same nozzle configuration are found to be close to each other indicating that for this metric numerical convergence is largely achieved. Consistent with the larger non-axial velocity observed for the Unprocessed Spray A nozzle flow, the corresponding interface displacement follows the same trend. The mean displacement values for the Educated nozzle geometry are milder and the external-only case is significantly lower than both nozzle cases.

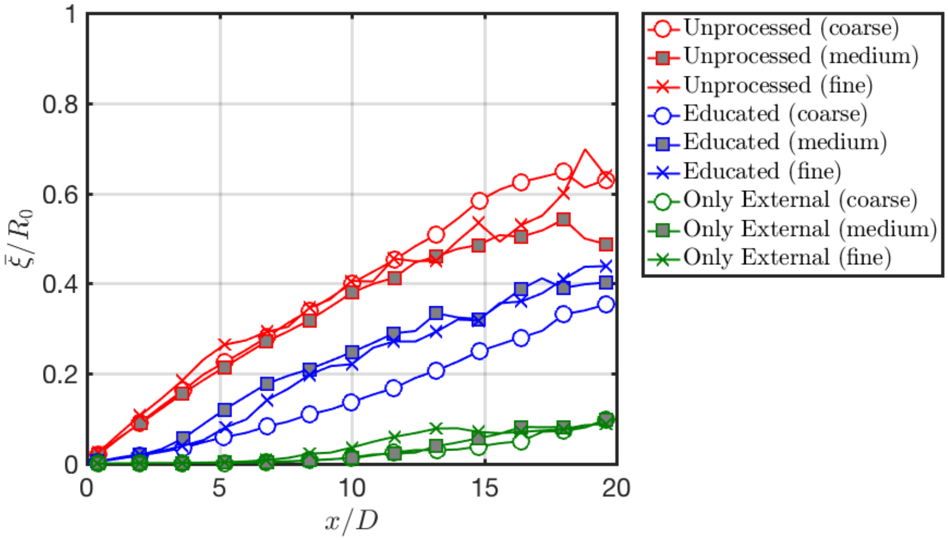

Figure 2.8: The averaged disturbance values, $\langle\bar{\xi}\rangle$, are shown as a function of the axial location, x, for the different spray configurations.

2.2.3 Turbulent Kinetic Energy and Transverse Velocity Magnitude

As the injected liquid is the primary source of momentum in the present study, the turbulent kinetic energy (k_L) of the liquid phase is considered here. This turbulent kinetic energy is obtained from

$$k_L(\mathbf{x}) = \frac{1}{2}\langle\alpha(\mathbf{u}' \cdot \mathbf{u}')\rangle, \tag{2.6}$$

where $\mathbf{u}' = (\mathbf{u} - \langle\mathbf{u}\rangle)$ is the perturbation velocity, and k_L is weighted by the local liquid volume fraction, α, to isolate the liquid phase. This calculation of the TKE is directly based on the resolved velocity field and is free of turbulence modeling approaches. Its grid sensitivity is examined in Section 2.2.5.

To gauge the progression of TKE as the liquid undergoes passage through the nozzle, exits the internal domain, and is subsequently atomized, it is presented in terms of a planar average, namely

$$\overline{k_L(x)} = \frac{\int_{y=-L_y/2}^{y=L_y/2} \int_{z=-L_z/2}^{z=L_z/2} k_L(x,y,z) \mathrm{d}y\mathrm{d}z}{\int_{y=-L_y/2}^{y=L_y/2} \int_{z=-L_z/2}^{z=L_z/2} \langle \alpha \rangle \, \mathrm{d}y\mathrm{d}z}. \tag{2.7}$$

This quantity is normalized by the time-averaged amount of liquid in any cross-sectional plane at some axial distance x from the nozzle exit.

The $\overline{k_L}$ profiles are presented on a log-linear plot in Fig. 2.9 for the different injection configurations. Similar to the earlier figures, curves pertaining to a given geometry are given the same color and within each color different markers are employed for the various levels of numerical resolution. The first observation regarding the results of Fig. 2.9 concern the much larger levels of turbulence for both nozzle configurations in contrast to the external-only geometry. This level of turbulence is caused mostly by the various asymmetries and imperfections of the nozzle surface features. It should be noted that there is no k_L at the inlet plane for both nozzle geometries. These inlet planes displayed in Fig. 1.1 are assigned a steady and spatially uniform velocity (note, the inlet plane location is $x/D_0 = -19.9$, which is far from the range shown in Fig. 2.9). As the flow transitions from wall-bounded flow to the external domain, there is a sharp change in the slope of $\overline{k_L}$. This is a direct result of the interfacial instabilities and hydrodynamic breakup occurring in the external domain. It is interesting to see that this level of growth, i.e., $d\overline{k_L}/dx$, is similar in all configurations, even though $\overline{k_L}$ it approximately two orders of magnitude lower for the external-only cases.

A second observation concerns the higher level of $\overline{k_L}$ for the Unprocessed geometry inside the nozzle. Having already observed a larger degree of non-axial velocity components for the mean velocity field in conjunction with the much rougher nozzle surface, this is not surprising. However, beyond the confinement of the nozzle, the level of turbulence is remarkably similar for the

Unprocessed and Educated geometry cases. This implies that the $\overline{k_L}$ differences observed between these two geometries inside the nozzle do not translate to much greater differences in the external domain. In the work of Chouak et al. [15], the authors reached a similar conclusion with regards to the effects of nozzle geometry on turbulence intensity.

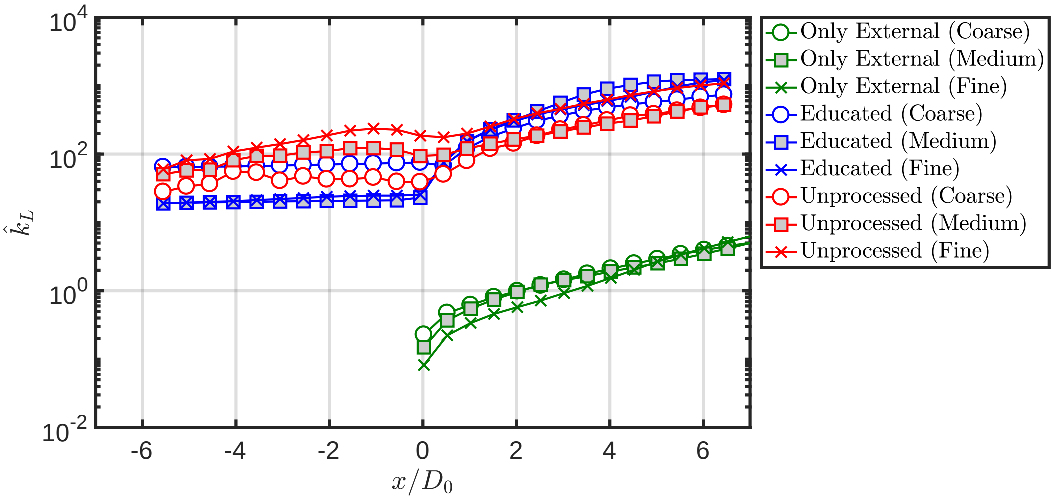

Figure 2.9: The mean liquid TKE, $\overline{k_L}$, is presented as a function of the axial distance.

To further illustrate the importance of the steady transverse velocity as compared to the turbulent fluctuations, we compare the magnitude of the non-axial velocity component, $|\langle \mathbf{u}_\perp \rangle|$, and the perturbation velocity component, $|\mathbf{u}'|$. We focus on a $5\,\mu$m-thick band at the wall at the orifice opening adjacent to the interface. As demonstrated in Section 2.2.1, the velocity profile in this region is important as it directly impacts the liquid jet surface. The average values of the velocity components are documented in Table 2.1. For the Unprocessed geometry the $|\langle \mathbf{u}_\perp \rangle|$ is higher than $|\mathbf{u}'|$ by an order of magnitude. For the Educated geometry, however, these magnitudes are comparable. This demonstrates that the effect of surface roughness is not confined to merely augmenting turbulence. It also leads to the creation of a steady non-axial velocity component, $|\langle \mathbf{u}_\perp \rangle|$.

Table 2.1: The steady non-axial velocity component, $|\langle \mathbf{u}_\perp \rangle|$, and the perturbation velocity component, $|\mathbf{u}'|$, are compared for the two Spray A configurations. The values reported have been averaged over a $5\,\mu$m-thick band near the wall at the orifice opening.

Geometry	$\lvert\langle \mathbf{u}_\perp \rangle\rvert$ (m/s)	$\lvert\mathbf{u}'\rvert$ (m/s)
Spray A (Unprocessed)	10.3	1.7
Spray A (Educated)	2.1	2.6

2.2.4 Length of Liquid Core

Having established the higher level of surface disturbance produced by flow in the Unprocessed geometry, as well as the significant effect the internal flow has on the destabilizing the liquid in the near field, the final comparison is made with regards to the length of the liquid that is topologically connected to the nozzle, simply referred to as the intact liquid core. Time histories of this intact liquid core are presented in Fig. 2.10. The instantaneous liquid length values are shown with lighter lines in the figure. At the start of injection, the length of the liquid core increases linearly for all the nozzle configurations. At some point in time (between $5\,\mu$s to $17\,\mu$s depending on the nozzle configuration) hydrodynamic breakup begins, and the length of the liquid core fluctuates about a mean value. The time series beyond the breakup point are included here to give a sense of the magnitude of the liquid core fluctuations. Additionally, a moving average of the instantaneous data starting at $t = 20\,\mu$s is presented by the darker lines with the markers. The averaged values quickly converge to a specific value for each of the cases, which corresponds to the reported mean breakup lengths documented in Table 2.2. For the same nozzle configuration, the values of the mean liquid core length among the different grid levels are similar suggesting numerical convergence.

Table 2.2: Intact core lengths for the different spray configurations and grid resolution levels.

Geometry	Coarse	Medium	Fine
Spray A (Educated)	$35.7D_0$	$37.8D_0$	$35.7D_0$
Spray A (Unprocessed)	$23.4D_0$	$25.6D_0$	$20.4D_0$
External-only	$46.5D_0$	$49.2D_0$	$51.9D_0$

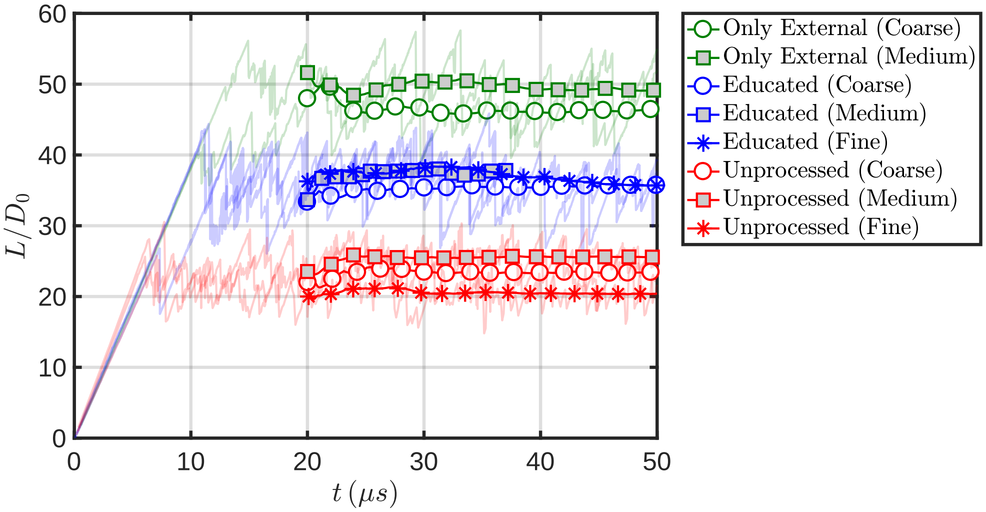

Figure 2.10: The length of the intact liquid core as a function of time for the different configurations. The instantaneous liquid length values are represented with the lighter lines and the moving average of the data is represented by the darker lines with the markers.

There is a clear trend across the different nozzle configurations; the Unprocessed Spray A configuration has the shortest liquid core length followed by the Educated Spray A configuration and the longest core length is observed for the external-only flow configuration. Through reconstructions of ensemble-averaged X-ray radiography data, Pickett et al. [53] estimate the intact liquid core length to be approximately 2.5 mm or $27.7D_0$. In the present simulations, there is an apparent sensitivity of the breakup lengths to the nozzle surface features resulting in the experimentally estimated length being somewhere in between the lengths reported for the two Spray A nozzles. The larger magnitudes for surface features corresponding to the Unprocessed geometry, which produce similarly larger values for radial (non-axial) velocity components and larger surface displacements, lead naturally to a shorter intact liquid core.

2.2.5 Grid Convergence

In this section we provide a detailed assessment of the numerical convergence of the data presented in this chapter. While at the current flow conditions (Re_L, We_L), we do not have access to sufficient resources such that numerical error can be shown to be approximately zero as $\Delta x \to 0$, we can definitely quantify the degree of convergence for key metrics of the problem.

The central idea of the present analysis is to verify whether the error reduces progressively as we refined the grid from the coarse level (Δx_1), to the medium level (Δx_2), and ultimately to the fine level (Δx_3). This is captured in the convergence ratio metric, $\mathcal{C}$, which is defined as

$$\mathcal{C} = \frac{\epsilon_1}{\epsilon_2} = \frac{\mathrm{mean}(|f_{\Delta x_1} - f_{\Delta x_2}|)}{\mathrm{mean}(|f_{\Delta x_2} - f_{\Delta x_3}|)}. \tag{2.8}$$

where the ϵ values are computed as

$$\begin{aligned} \epsilon_1 &= \mathrm{mean}(|f_{\Delta x_1} - f_{\Delta x_2}|) \\ &= \frac{1}{n_x} \sum_{i=1}^{n_x} |f_{\Delta x_1}(x_i) - f_{\Delta x_2}(x_i)|. \end{aligned} \tag{2.9}$$

Here n_x is the number of discrete x_i points on which the error is evaluated. If $\mathcal{C} > 1$, then the absolute difference between the medium and fine grid is smaller than the absolute difference between the coarse and medium grids. Under these conditions, we interpret the results as indicating convergence, since the difference between grid levels is decreasing as we reduce Δx.

With respect to the key parameters characterizing this work, we chose the PMD (Φ_z and Φ_y) since the prediction of mass distribution in the near-field region is a fundamental quantity characterizing atomization characteristics. Additionally, we consider the departure from base shape, $\overline{\langle \xi \rangle}/R_0$, since this is a key characteristics that quantifies the degree of atomization and how it changes between the two nozzle configurations. A standard metric is also the TKE. Since it is the liquid that dominates the source of energy owing to its larger density and higher velocity, we consider the liquid TKE. Finally, the overall metric that quantifies breakup is the intact liquid core length, and this is also considered.

The results are presented in Table 2.3, which show converging trends for the majority of metrics. One notable exception corresponds to the external-only configuration, where for this geometry all of the predictions are already relatively close to each other. For instance, $\text{mean}|\overline{k_{L}}_{\Delta x_2} - \overline{k_{L}}_{\Delta x_3}|/\text{mean}|\overline{k_{L}}_{\Delta x_3}| = 0.03$. This implies that while convergence is not indicated by $\mathcal{C}$, it is expected based on the small displacement between predictions corresponding to different grid levels. This can be seen in Figures 1.8–1.10, 2.7, 2.9. As more powerful computational resources become available, these calculations will be revisited at lower values for Δx.

Table 2.3: Grid convergence metrics for data presented in Figures 1.8, 2.7, 2.9 and 2.10.

Geometry	Φ_z Fig. 1.8a	Φ_y Fig. 1.8b	$\overline{\langle\xi\rangle}/R_0$ Fig. 2.7	$\overline{k_L}$ Fig. 2.9	L/D_0 Fig. 2.10
Spray A (Educated)	2.81	0.82	3.53	2.52	2.50
Spray A (Unprocessed)	4.51	3.76	1.27	0.20	0.43
External-only	0.69	0.59	0.48	0.51	1.38

2.3 Conclusions

The first conclusion from the present chapter concerns the large change in intact liquid core length by $\mathcal{O}(1)$ mm in addition to substantial changes in gas-liquid interface disturbances as a result of $\mathcal{O}(1)$ μm variations in internal nozzle surface features corresponding to a change from the Educated geometry to the Unprocessed geometry. It is truly surprising to see this level of sensitivity to such a small change in the internal nozzle surface morphology. Since the injection velocities are high in the axial direction, small changes in this velocity direction caused by small nozzle surface features lead to relatively high non-axial velocity magnitudes. These effects amplify the near-field surface characteristics leading to an earlier fragmentation of the liquid core.

The second conclusion draws attention to the conditioning of the flow as a result of its passage through the internal geometry. It is well established in the community that such an internal flow inevitably augments the turbulence leading to more interfacial disturbances in the spray near-field and more atomization. A new aspect introduced in the present chapter is that this flow conditioning is not simply an augmentation in turbulence but also a creation of persistent and organized flow structures in the internal nozzle flow. It is these structures that are significant contributors to the disturbances occurring in the near-field, which eventually lead to accelerated atomization. In the case of the Unprocessed Spray A, these flow structures are an order of magnitude larger than the turbulent velocity fluctuations.

Chapter 3

Evaluating Surface Tension Schemes with Respect to High-Fidelity Atomization Simulations

3.1 Background & Motivation

In high-speed liquid injection, as the atomization process happens, liquid away from the intact core appears in the form of smaller ligaments and droplets, which move at relatively lower speeds. As a result of the smaller sizes and speeds, surface tension force dominates the dynamics of these liquid structures. Processes like breakup of ligaments, and motion and collision of droplets are surface tension dominated. Accurately computing the surface tension force in the simulations is therefore important.

The Volume of Fluid (VoF) method is a robust method well suited for atomization simulations, especially because of its mass conserving properties [20]. Poor calculation of surface tension has been the only major weakness of the method [20, 54, 55]. This arises because of the poor accuracy of curvature calculations made based on second order derivates of the sharply varying volume fraction field. A variety of novel methods have tried to address this problem. Martinez et al. [44] proposed an improved method to compute the curvature based on a piecewise linear interface construction (PLIC). They report reduction in spurious currents through their method, but only simple 2D tests have been presented. Popinet [54] presents an improvement on the height function method. This results in better performance in the low-resolution limit, a major weakness of the standard height-function method [18]. This method was tested in some 2D and 3D tests. In the standard height-function method, the underlying grid is used to compute the height function. As an improvement over this, Owkes and Desjardins [50] present a variation where the height function calculation is decoupled from the underlying grid, it is instead computed on columns that are not aligned with the grid. Up to second order convergence is reported for well-resolved interfaces in static 2D and 3D test setups and approximately first order convergence is reported for a 2D capillary wave setup. Wenzel and Garrick [75] evaluate finite particle methods for curvature and report an order of magnitude improvement for static 3D sphere tests when a smoothed volume fraction field is used. Owkes et al. [49] propose a polynomial fit to the VoF interface over an adjustable lengthscale. They present 2D tests like the standing capillary wave and a 2D oscillating droplet.

Popinet [55] summarizes the recent developments in surface tension modeling and note the marked improvement in the methods over the last 20 years. He points out the need for stanardized, non-trivial test cases. Cummins et al. [18] compare the curvature computation performance for a convolved-VoF based method, a distance function based method and a height function method. They have presented static, canonical test cases. Vachaparambil and Einarsrud [72] compare three different surface tension models – continuum surface force, smoothed continuum surface force and sharp surface force, but their tests are also limited to simple 2D problems.

A common trend is that new methods in general add complexity to the curvature calculation in order to improve the accuracy. Two questions, however, arise through these developments. The first is regarding the applicability of the methods for realistic flow problems. As summarized above, the tests presented with every new method are limited to simple, canonical test problems that do not always represent realistic, atomization-elevant flow situations. The second is regarding the extent to which the improvements in surface tension computations matter in atomization type simulations with multiple, complex phenomena occurring simultaneously.

In the present work we address these two questions. The `interFoam` solver, based on the VoF framework has been employed here. This solver is robust and fairly accurate, has been characterized in detail [20], and has been used in several atomization studies [3, 4, 21, 69]. As pointed out earlier, a shortcoming of the solver, and the VoF method in general, is the curvature calculation. There is a need for an improved surface tension computation in the solver. Here we investigate three potential methods towards this. The first is a standard calculation based on the liquid volume fraction field, the second is based on a diffused volume fraction field and the third is based on a signed distance function. The basic motivation for the second and third methods is to base the curvature calculation on a smoothly varying and more spread out function, instead of the sharply varying liquid fraction field which is used in the standard calculation.

The present chapter is a first step towards assessing the effect of curvature schemes in full atomization simulations. The contents are organized as follows. Section 3.2 describes the three numerical schemes and their implementation. We introduce a novel method to compute the signed distance function from the underlying volume fraction field. Section 3.3 focuses on systematic testing and analysis of the methods using increasingly complex tests – starting from a canonical 2D droplet test and building up to more complex 3D cases like Rayleigh breakup of a liquid column and up to full atomization cases.

3.2 Numerical Methods

Similar to the earlier chapters, the Volume-of-Fluid (VoF) simulations reported in this chapter are performed with an algebraic solver, `interFoam`. The `interFoam` solver forms a part of a larger open-source distribution of computational mechanics solvers and C++ libraries of OpenFOAM, which is designed for finite volume discretization on collocated grids for the solution of two-phase incompressible flows and is benefited from various discretization strategies. A brief description of the solver was provided in Section 1.2. Here we only describe the surface tension computation in the solver.

The liquid volume fraction, α, represents the volume fraction of liquid occupying a given computational cell. The volume of fluid method relies on the advection of the α-field to keep track of the liquid-gas distribution. Based on the α-field the thermophysical properties (ρ, μ) are determined in the domain and the momentum equation is solved, thus updating the velocity and pressure fields.

The surface tension force typically appears in the momentum equation as a boundary force. In the present formulation the boundary force is converted to a volume force by employing the Continuum Surface Force method [13]. Namely, the surface integral over the interface is expressed as a volume integral as,

$$\int_{\Gamma\cap\Omega_i} \sigma\kappa\delta(\mathbf{x}-\mathbf{x}_s)\mathbf{n}d\Gamma(\mathbf{x}_s) = \int_{\Omega_i} \sigma\kappa\nabla\alpha dV, \tag{3.1}$$

where the local curvature is given by κ, the surface tension coefficient by σ, the gas-liquid interface by $\Gamma(t)$, the 3D Dirac Delta function by $\delta(\mathbf{x}-\mathbf{x}_s)$, $\mathbf{x}_s$ is the integration variable over $\Gamma(t)$ and Ω_i denotes a cell in the domain.

The focus of the present work is calculation of the κ. The three schemes used to compute the curvature are briefly described in the following subsections.

3.2.1 Standard Calculation (α-based)

The local curvature is the divergence of the normal vectors to the interface. The simplest way to compute κ is therefore given as

$$\kappa = \nabla \cdot \frac{\nabla \alpha}{|\nabla \alpha|}, \tag{3.2}$$

since the interface normal is given by $\hat{\mathbf{n}} = \frac{\nabla \alpha}{|\nabla \alpha|}$.

In the present finite volume framework this is computed by interpolating the cell-centered normal vectors to the faces, $\hat{\mathbf{n}} \rightarrow \hat{\mathbf{n}}_f$, and then performing the divergence operation within each cell, i.e., $\kappa = \nabla \cdot \hat{\mathbf{n}}_f$.

3.2.2 Diffused α-Based Calculation ($\tilde{\alpha}$-based)

The α-field is sharply varying at the interface, therefore, the numerical derivatives have high error magnitudes. One way to mitigate this is to base the curvature calculations on a smoother α-field, represented as $\tilde{\alpha}$ here. This also reduces the high-frequency noise from the α-field. In the present method the $\tilde{\alpha}$ is computed using a diffusion operation on α.

$\tilde{\alpha}$ is initialized as $\tilde{\alpha} = \alpha$ and then updated through an unsteady diffusion operation as,

$$\frac{\partial \tilde{\alpha}}{\partial \tau} = D \nabla^2 \tilde{\alpha}, \tag{3.3}$$

where τ is the pseudo time, and D is the diffusion constant ($D = 1$ here). This is solved for a set number of $\Delta\tau$ steps to reach a desired diffusion length scale. Here, we pick the diffusion length scale to be $1\Delta x$. The curvature is then calculated as,

$$\kappa = \nabla \cdot \frac{\nabla \tilde{\alpha}}{|\nabla \tilde{\alpha}|}. \tag{3.4}$$

The numerical implementation of Eq. (3.4) is the same as the one described for the standard calculation.

3.2.3 Distance-Based Calculation (ϕ-based)

Signed-distance functions are routinely used in level-set methods to represent the interface [5, 6]. The zero level-set of the function represents the interface. The signed-distance function, ϕ, represents the shortest distance from the interface, and ϕ is set to be positive in liquid and negative in gas. By definition, ϕ varies linearly as we move normal to the interface. This leads to a smoothly varying gradient field which can be advantageous in curvature computations. Therefore, in this method, the curvature is computed from the ϕ-field. The challenge however is to obtain an accurate ϕ based on the discrete α-field.

Here we propose a novel method to construct the ϕ-field. The construction is done in two steps, initialization and propagation, as outlined here:

A. Initialization - handled geometrically

   In this step, a piecewise-linear interface is constructed in the interfacial cells, and for these cells the distance is computed geometrically from the cell center to the interface center. This is described briefly here. More details can be found in [60].

   i. The cell-based α values are interpolated to cell vertices using linear interpolation.

   ii. Interface points, $\mathbf{x}_{e,j}$, defined as locations where $\alpha = 0.5$, are identified along the cell edges. Linear interpolation is used for this step. The subscript e signifies that these points are on the edges, and the subscript j is the index of the points.

   iii. If a cell has at least 3 interfacial points then it is tagged as an interfacial cell (since in 3D a plane needs at least 3 points).

   iv. Construct interface plane, i.e., identify interface center, $\mathbf{x}_c$, and interface area vector $\mathbf{A}$

- Set one interface point, say $\mathbf{x}_{e,1}$ as the origin. Sort points $\mathbf{x}_{e,j}$ in cyclical order using the shoelace formula [60]

- Compute interface center as,

$$\mathbf{x}_c = \sum_{j=1}^{N_p} \mathbf{x}_{e,j} \tag{3.5}$$

- Compute area vector as,

$$\mathbf{A} = \sum_{j=1}^{N_p} \frac{1}{2} \left((\mathbf{x}_{e,j} - \mathbf{x}_{e,1}) \times (\mathbf{x}_{e,j+1} - \mathbf{x}_{e,1}) \right) \tag{3.6}$$

To ensure that the area vector points from the liquid to the gas in all cells,

$$\text{if } \nabla\alpha \cdot \mathbf{A} > 0, \text{ then } \mathbf{A} \text{ is set to} - \mathbf{A} \tag{3.7}$$

v. Compute perpendicular distance, $d_\perp$, from cell center to interface as,

$$d_\perp = \mathbf{r} \cdot \hat{\mathbf{n}} = \frac{\mathbf{r} \cdot \mathbf{A}}{|\mathbf{A}|}, \tag{3.8}$$

where $\mathbf{r} = \mathbf{x}_c - \mathbf{x}_{\text{cell cent.}}$, and $\hat{\mathbf{n}}$ is the interface normal. This expression is simply a projection of the $\mathbf{r}$ vector along the interface normal.

vi. For the interfacial cells, ϕ is initialized as $\phi = d_\perp$. The non-interfacial cells are initialized as $\phi = (\alpha - 0.5)\Delta x$, i.e., $\phi = \Delta x/2$ in liquid cells and $-\Delta x/2$ in gas cells.

B. Propagation - handled algebraically

In the first step, ϕ values were assigned to interfacial cells, but the rest of the cells the ϕ values are not yet assigned. To correctly assign these values we rely on the Hamilton-Jacobi equation, which is commonly used for reinitializing level-set functions [5],

$$\frac{\partial \phi}{\partial \tau} = S(\phi_0)\left(1 - |\nabla \phi|\right), \tag{3.9}$$

where $S()$ denotes a sign-function. This equation is solved using an explicit time-stepping and an upwind discretization of $\nabla\phi$. To identify the upwinding velocity, Eq. (3.9) can be expressed in like an advection equation as,

$$\frac{\partial \phi}{\partial \tau} + \underbrace{\left[S(\phi_0)\frac{\nabla \phi}{|\nabla \phi|}\right]}_{\mathbf{v}_p} \cdot \nabla \phi = S(\phi_0), \tag{3.10}$$

where $\mathbf{v}_p$ is the velocity at which the solution propagates, i.e., the upwinding velocity.

As per the CSF formulation the surface tension force is active only in cells where $|\nabla\alpha| \neq 0$, i.e., a few cells around the interface. So the κ (and ϕ) values are needed in a few cells around the interface. In the solution of Eq. (3.9), the final stopping pseudo-time determines the extent of propagation of the ϕ solution. Here we propagate the ϕ solution to 4 cells away from the interface, in both, gas and liquid, i.e., a 9-cell band around the interface. The pseudo-time step, $\Delta\tau$ is set as $0.2\Delta x$ and the solution is evaluated up to 20 pseudo-time steps.

At this point we have a signed distance field, ϕ. Now, the curvature is computed as,

$$\kappa = \nabla \cdot \frac{\nabla \phi}{|\nabla \phi|}. \tag{3.11}$$

Once again, the numerical implementation of Eq. (3.11) is the same as the one described for the standard calculation.

3.3 Results

In this section we present 5 test cases, starting with a simple 2D circular droplet and building up to a full atomization case. We present results from the three methods across a range of numerical resolutions, and flow parameters.

3.3.1 2D Circular Droplet

A commonly used test problem is the 2D circular droplet test. Here a circular liquid droplet in gas is used to test the performance of the different schemes against analytical values. The setup is shown in Fig. 3.1. Analytical values of the curvature and the pressure jump across the interface are available for this simple setup. The curvature in 2D is given simply by $\kappa = 1/r$, where r is the local radius of curvature. In this setup we have $R = 1/4$m, therefore the analytical curvature value at the interface is $\kappa_0 = 4\ \mathrm{m}^{-1}$. Numerically obtained curvature values are presented for three grid levels in Fig. 3.2.

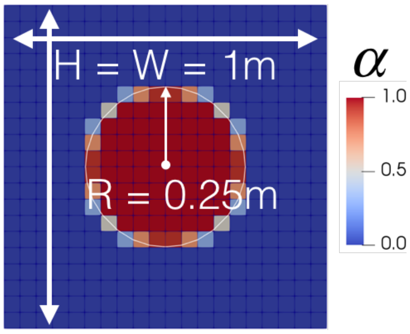

Figure 3.1: An illustration of the 2D circular droplet setup test. The liquid-gas interface is shown along with the initial discrete α-field.

The mean error in the κ values in a 6-cell wide band around the interface are presented in Fig. 3.3 along with a $c\Delta x$ reference line. The error is very different for the three methods. The ϕ-based method weakly follows a first order convergence and the standard α-based method appears to diverge. The $\tilde{\alpha}$-based results are in between the two.

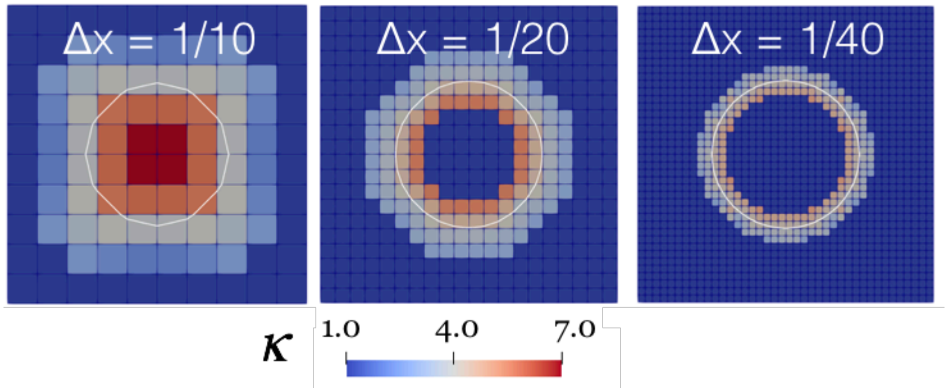

Figure 3.2: The κ values near the interface are demonstrated for three different grid resolutions, $\Delta\ x\ =\ 1/10,\ 1/20$ and $1/40$.

The curvature affects the surface tension force contribution which leads to the pressure jump in this setup. A higher pressure is expected inside the liquid droplet as compared to the outside. The pressure jump is given by the Young-Laplace equation as $\Delta p = \sigma\kappa = 4$. Here, the fluid properties are $\rho_l = \rho_g = 10^4$, $\mu_l = \mu_g = 1$ and $\sigma = 1$. The computations are run up to $t = 125$ consistent with previous studies in literature [20, 28]. The pressure data obtained along the centerline of the setup is shown in Fig. 3.4 for the three different schemes. Along with data for the three grid levels, the analytically expected pressure curve is also shown in the plots.

The pressure data from the standard computation is shown in Fig. 3.4a. It can be seen that upon refinement the pressure inside the liquid converges to a value lower than the analytical value. This is a direct result of the poorer curvature values. The pressure values improve for the other two methods as seen in Fig. 3.4b and 3.4c. For the $\tilde{\alpha}$ computation, the coarse case performs relatively poorly as seen in Fig. 3.4b. Upon refining the grid the pressure values converge to the analytical values. We observe a similar trend for the ϕ-based computation where the values converge to the analytical value upon grid refinement.

The error in the pressure jump across the interface is presented in Fig. 3.5 as a function of Δx for the three different methods on a log-linear scale. Two reference lines corresponding to first and second order convergence are included as well. There is clear second order convergence in

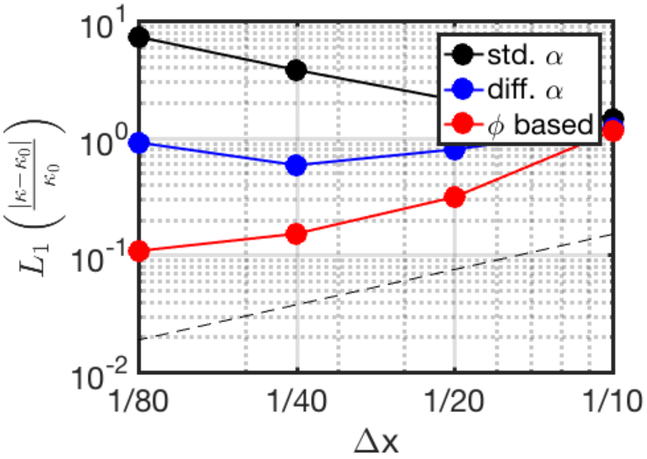

Figure 3.3: The mean error in the κ-field is presented for the different methods with respect to varying grid resolutions on a log-linear scale. The dotted line represents a cΔx-trend line.

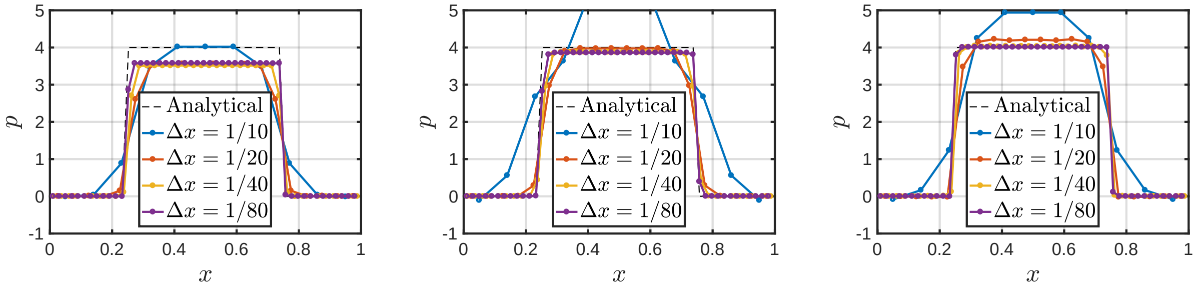

(a) Standard α computation

(b) $\tilde{\alpha}$-based computation

(c) ϕ-based computation

Figure 3.4: Pressure distribution along the centerline is presented for the three different schemes at four different grid resolutions each. The dotted line in the figures represents the analytical pressure value.

the data from the ϕ-based method. The diffused α-based method exhibits mixed results, where the convergence trend is unclear but the error magnitudes are smaller than those from the α-based method. The error from the α-based method appears to saturate and does not reduce upon refinement.

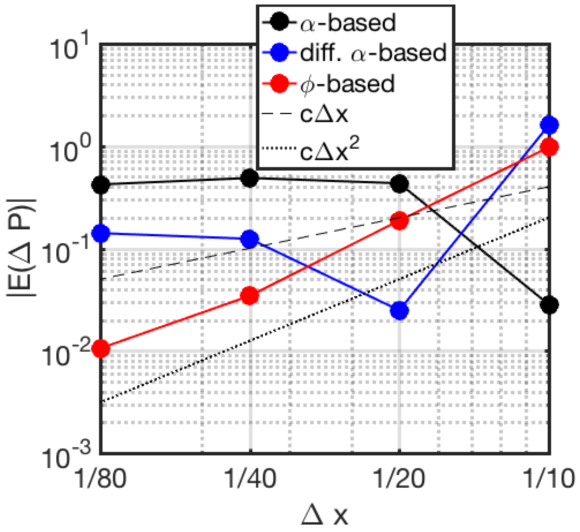

Figure 3.5: Mean error in the pressure jump is presented here on a log-log plot for the three methods for four different grid levels.

3.3.2 3D Oscillating Droplet

In this test an initially spherical droplet is perturbed with a small perturbation and the oscillation is observed. The motion of the droplet is driven by surface tension and inertia. The oscillations are eventually damped out by viscosity.

The initial shape of the perturbed droplet is given as,

$$R = R_0 \left[1 + \eta P_2 \left(cos\theta\right)\right], \tag{3.12}$$

where $R_0 = 1$m is the unperturbed radius, η is the magnitude of perturbation, set as 0.04, P_2 represents the Legendre polynomial of second order, and θ is the polar angle. This is set up in a $[4R_0 \times 4R_0 \times 4R_0]$ domain with no-slip boundaries. The physical properties of the liquid and gas are as follows: density $\rho_l = 1$, $\rho_g = 0.01\,\mathrm{kg\ m^{-3}}$; viscosity $\mu_l = 0.01$, $\mu_g = 0.0001\,\mathrm{Pa\cdot\ s}$ and surface tension $\sigma = 1\,\mathrm{Nm^{-1}}$. This setup is the same as the one used by Patel et al. [51].

For this setup Lamb [38] has given the analytical expression for the motion of the interface as,

$$r(t) = \eta \exp\left(-t\frac{5\mu_l}{\rho_l R_0^2}\right) \cos\left(t\sqrt{\frac{24\sigma}{R_0^3[3\rho_l + 2\rho_g]}}\right). \tag{3.13}$$

We compare our simulation data against this expression. Fig. 3.6 shows the location of the top point of the droplet for the three different schemes. In each of the plots we show data for three different grid resolutions. The analytical result from Eq. (3.13) is provided for comparison.

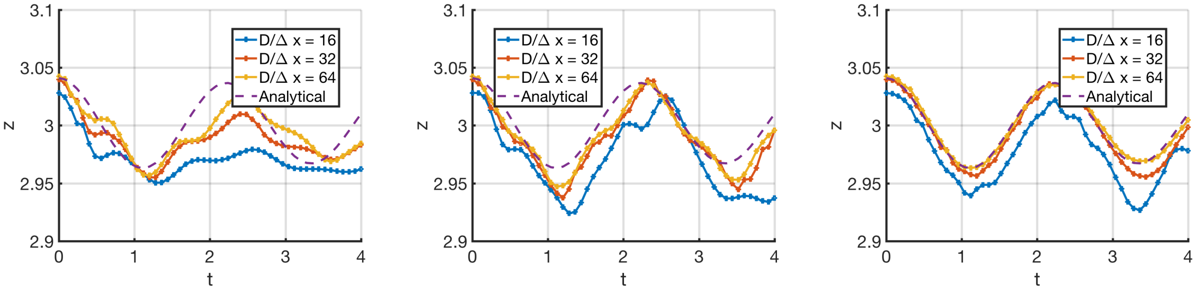

(a) Standard α computation (b) $\tilde{\alpha}$-based computation (c) ϕ-based computation

Figure 3.6: The position of the topmost point of the droplet is presented as a function of time along with the analytically expected trend. Three different grid resolutions are presented for each of the methods.

It can be seen that for all the three methods the results move closer to the analytical expression upon refinement of the grid. The results from the ϕ-based method (Fig. 3.6c) appear to outperform the other methods.

The mean error in this data is shown in Fig. 3.7. Error data for the three methods is presented as a function of the grid resolution and a first order reference line ($c\Delta x$) is provided. It can clearly be seen that the ϕ-based method has a lower error magnitude as compared to the other methods. However, the rate of convergence of the errors is the same across the three methods. The data roughly follows a 1^{st} order convergence for the three methods.

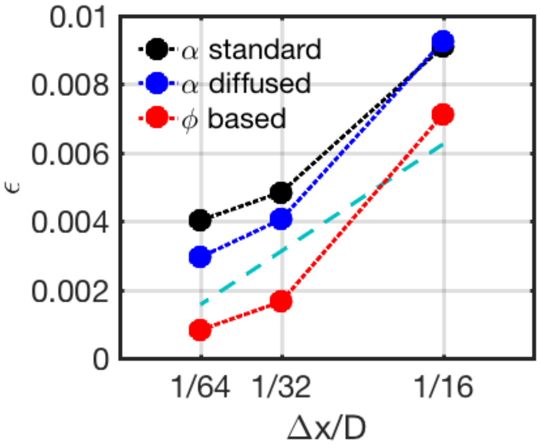

Figure 3.7: The mean error in the positions presented in Fig. 3.6 is presented here along with a $c\Delta x$ reference line.

3.3.3 Rayleigh Breakup of Liquid Column

In this test we consider the classic Rayleigh breakup of a laminar liquid jet [56]. This is a surface tension-driven flow pertinent to liquid breakup simulations. Here we begin with a liquid column with a varicose sinusoidal perturbation imposed on its surface as seen in Fig. 3.8a. This perturbation grows and eventually disintegrates the liquid column, as seen in Fig. 3.8b and Fig. 3.8c. The breakup usually leads to the formation of two structures, a large 'main' droplet at the boundary of the domain and a smaller 'satellite' droplet near the middle. These droplets are labelled in Fig. 3.8c. The periodic nature of the simulation domain means that the main droplet is continuous across the top and the bottom faces of the domain.

Lafrance [37] provides a detailed analysis, accounting for non-linear effects, and predictions for the sizes of the resulting droplets. Their experiments are in agreement with these predictions. In this section we compare the present results against these theoretical predictions.

All simulations are performed on a water jet of $R_0 = 17.5 \times 10^{-6}\,\mathrm{m}$ with $\rho = 1000\,\mathrm{kg\,m^{-3}}$, $\mu = 10^{-3}\mathrm{N\,s\,m^{-2}}$ and $\sigma = 0.073\,\mathrm{N\,m^{-1}}$. $\Delta x = 1.3\mu\mathrm{m}$ in the region surrounding the liquid jet. Away from the jet a coarser grid is employed. The initial perturbation is given by $r = R_0 + A\cos\left(k\frac{z}{R_0}\right)$,

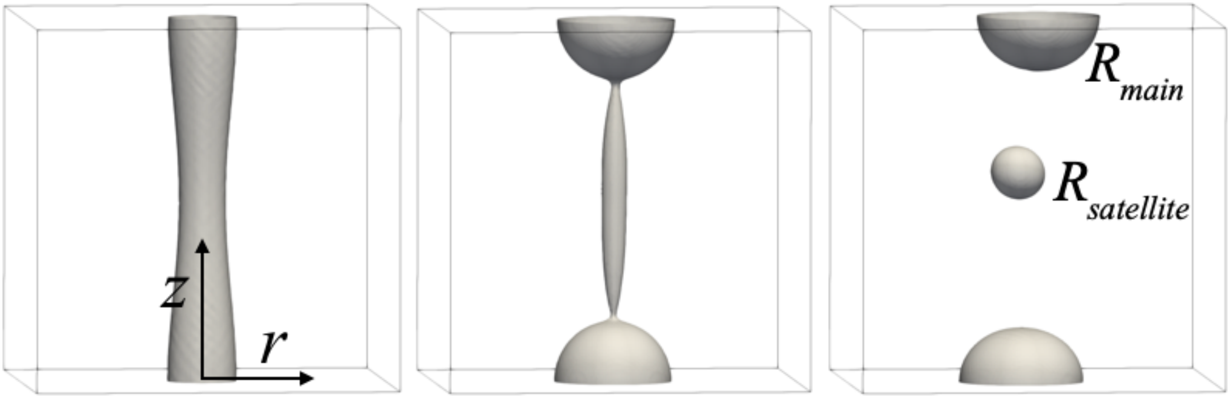

(a) Initial setup (b) Growth of perturbation (c) After disintegration

Figure 3.8: The evolution of the Rayleigh breakup of a liquid column is illustrated here through three different time snapshots. The final configuration has two droplets - the main droplet is continuous across the periodic boundary condition on the top and bottom faces.

where $A = 0.15R_0$ and k is the perturbation wavenumber. Simulations with $k = 0.5, 0.6$ and 0.75 are performed for each of the three curvature methods.

The radii of the resulting droplets are presented in Fig. 3.9 along with the theoretical predictions [37]. Data in red represents the main droplet size and data in blue represents the satellite droplet size. The theoretical predictions are shown using dotted lines, and the simulation results are shown with the different markers. Overall, the agreement with the theoretical predictions is good for the three methods. The error in the satellite droplet sizes is higher than the error in the main droplet sizes. The main droplet sizes for the three methods are close enough to each other that the markers in the plot appear to overlap. The differences are more apparent in the satellite droplet data. Among the three methods, the ϕ-based computation leads to the best droplet sizes. This is especially evident for $k = 0.5$. The droplet sizes predicted by the standard α and the $\tilde{\alpha}$-based methods are close to each other and it cannot be said which method performs better than the other. However, we observe that the satellite droplet from the $\tilde{\alpha}$-based simulation breaks up into smaller droplets. So while the droplet sizes are relatively accurate, the dynamics of the resulting droplets are not predicted well by the $\tilde{\alpha}$-based computation.

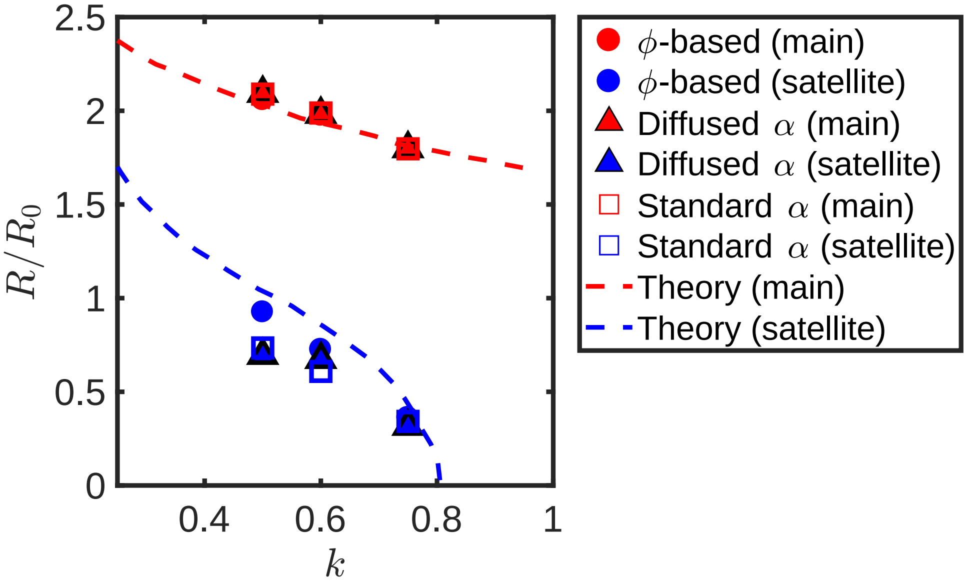

Figure 3.9: The radii of the two droplets after the breakup of the liquid column are presented here for the three different schemes at three different perturbation wavenumbers. Theoretically expected radii are represented using the dashed lines. The data in red represents the main droplet and the data in blue represents the satellite droplet.

3.3.4 Shear Layer: Growth of Interfacial Instability

In this test the growth of the instability on a two-phase shear layer setup is examined. The setup is illustrated in Fig. 3.10. There is gas on top and liquid on the bottom. The gas is moving to the right, and the liquid is moving to the left. This interface is unstable. In this setup this flow is perturbed initially and the perturbation is allowed to grow.

The fluid properties are as follows: $\rho_l = 1, \rho_g = 0.1\,\mathrm{kg\,m^{-3}}, \mu_l = 5.05 \times 10^{-5}, \mu_g = 5 \times 10^{-5}\mathrm{N\,s\,m^{-2}}$. Two values of σ are used here, $\sigma = 0.01\,\mathrm{N\,m^{-1}}$ and $\sigma = 0.1\,\mathrm{N\,m^{-1}}$. These correspond to two different Weber numbers, $We = \frac{\rho L U}{\sigma}$. A lower We implies a stronger contribution of the surface tension force. The Δx is set to $0.011\,\mathrm{m}$ to ensure that the small initial perturbation is sufficiently resolved.

The perturbation kinetic energy, $KE_{pert.}$, is tracked to track the growth rate of the instability.

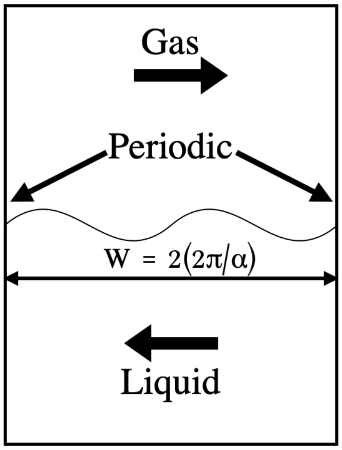

Figure 3.10: An illustration of the shear layer setup. The two phases are shown separated by the interface which has an initial sinusoidal perturbation on it.

The total $KE_{pert.}$ is computed as,

$$KE_{pert.} = \int \frac{\rho}{2} \left(\mathbf{U} - \langle \mathbf{U} \rangle\right) \cdot \left(\mathbf{U} - \langle \mathbf{U} \rangle\right) dV, \tag{3.14}$$

where $\langle \mathbf{U} \rangle$ is the base velocity and $\mathbf{U}$ is the instantaneous velocity.

As an example, the growth of $KE_{pert.}$ as a function of time is presented in Fig. 3.11 on a log-linear plot for the ϕ-based method. Here, we test 5 different wave numbers, specified by α. For $\alpha < \pi$ the growth is clearly exponential.

The $KE_{pert.}$ is expected to grow as $KE_{pert.} = A\exp(2\omega t)$. Based on this, the growth rate, ω, is extracted from the $KE_{pert.}$ data and presented in Fig. 3.12. The two subplots correspond to the two different Weber numbers. In these plots we present the growth rates for the five different wavenumbers for the three methods along with the analytically expected growth rate curve. The theoretical solution has been described by Deshpande et al. [21]. The code for this semi-analytical solution has been provided by Suraj Deshpande.

Overall we see very good agreement between the simulation results and the theoretical prediction across the three methods. From the two plots we can also see that the growth rates are

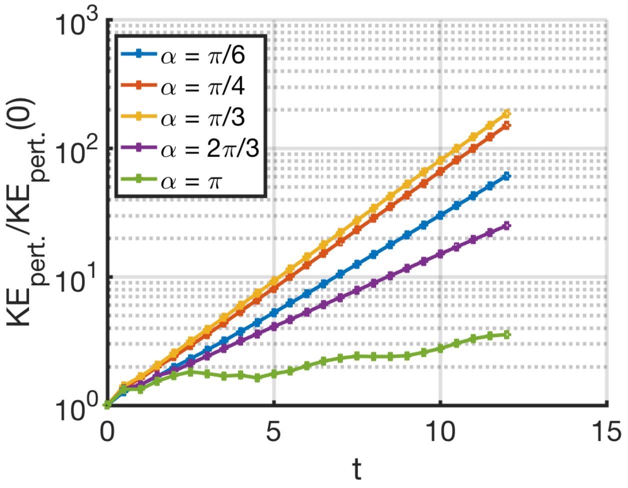

Figure 3.11: The perturbation kinetic energy, $KE_{pert.}$, as a function of time is presented for the ϕ-based method as an example of typical $KE_{pert.}$ growth. The 5 different curves correspond to 5 different wavenumbers, α.

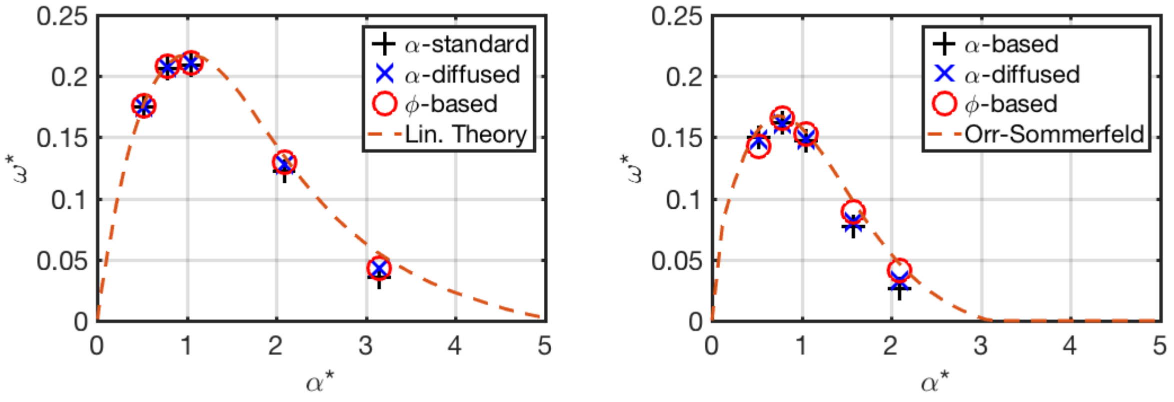

(a) We = 100

(b) We = 10

Figure 3.12: The growth rate of the shear-layer instability is presented for the different methods and cases along with analytically expected results.

lower for the lower We cases. This is to be expected as the surface tension is a stabilizing force here. Upon closer examination, it appears that the ϕ-based method slightly outperforms the other methods when the We is reduced to 10 (see Fig. 3.12b). This is especially seen when the growth rates are lower, for example at $\alpha = 2\pi/3$.

3.3.5 Retraction of Liquid Column

In this test a perfectly cylindrical liquid column, which is initially stationary, is allowed to retract under the action of surface tension. This test has been performed by Umemura [71] and Deshpande et al. [20].

The liquid is SF_6 ($\rho_l = 1460\text{kg m}^{-3}$, $\mu_l = 1.1 \times 10^{-3}\,\text{N}\,\text{s}\,\text{m}^{-2}$) and the gas is pressurized nitrogen ($\rho_g = 79.1\,\text{kg m}^{-3}$, $\mu_g = 1.76 \times 10^{-5}\,\text{N}\,\text{s}\,\text{m}^{-2}$). The surface tension constant here is $1.605 \times 10^{-3}\,\text{N}\,\text{m}^{-1}$. The simulations are performed on a uniform mesh with the finest resolution being $\Delta x = 7.8\,\mu\text{m}$ with 32 grid cells across the jet diameter. The time-step size is constant at $\Delta t = 2\mu\text{s}$. The non-dimensionalized time, t^*, is given by $t^* = t\frac{1}{R}\sqrt{\frac{\sigma}{\rho_l R}}$, where R is the radius of the cylinder.

Fig. 3.13 shows the evolution of the column at three different times for the three methods. The perfectly cylindrical liquid column at $t^* = 0$ starts retracting and a bulb and a neck are formed at the end of the column as seen in Fig. 3.14a. The contraction further continues as the surface tension tries to reduce the overall surface area and at $t^* = 18.9$ the bulb appears much larger. At this point subtle differences in the shapes of the columns across the three methods start emerging. The bulb for the $\tilde{\alpha}$ implementation appears flatter than the one from standard α. This evolution continues and at $t^* = 30$ a difference in the length of the liquid column also emerges.

The lengths of the columns are presented as a function of time in Fig. 3.14. Three figures are presented for the three methods. In each of the plots data for three different grid resolutions is presented. The strong overlap of the data as the grid is refined means that the grid is sufficiently resolved. The lengths follow the same pattern in all of the cases. At first the length is constant - this is when the liquid is still connected to the face on the right. The shape of the liquid cylinder starts to deform but the length remains equal to the length of the domain. At some point the liquid snaps off from the right face and the column starts retracting. The length varies linearly with time, implying that the retraction speed is constant.

Fig. 3.15 shows the length data for the finest cases of the three methods together. The lengths

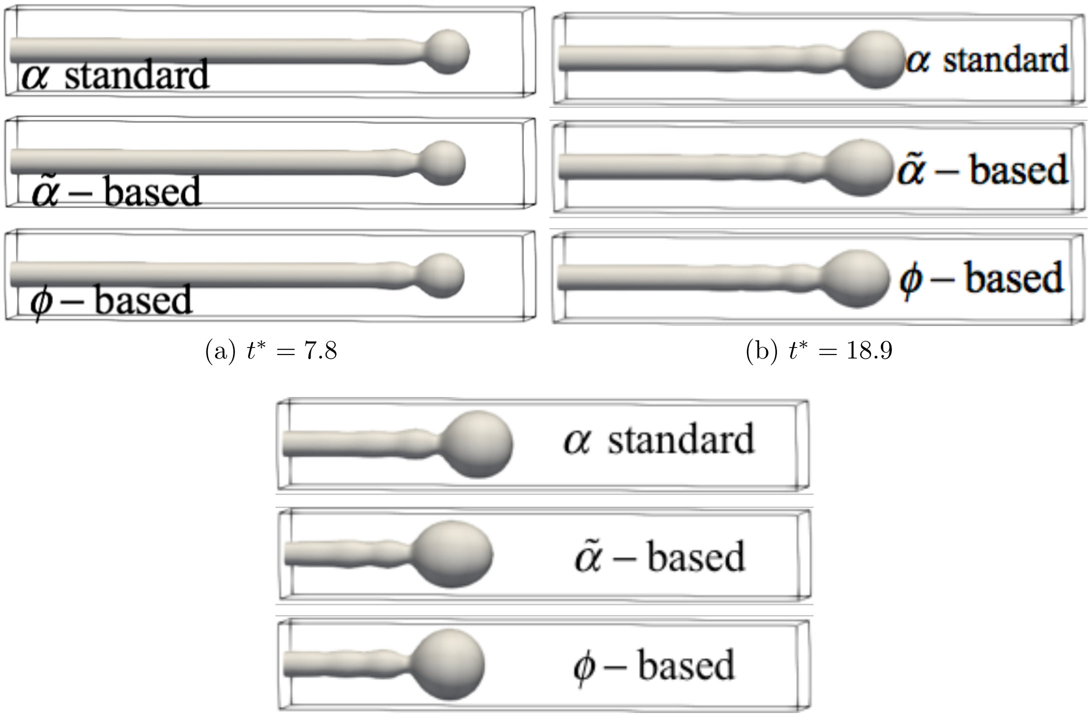

(a) $t^* = 7.8$

(b) $t^* = 18.9$

(c) $t^* = 30.0$

Figure 3.13: The evolution of the retracting liquid column for the three curvature schemes is illustrated through three time snapshots.

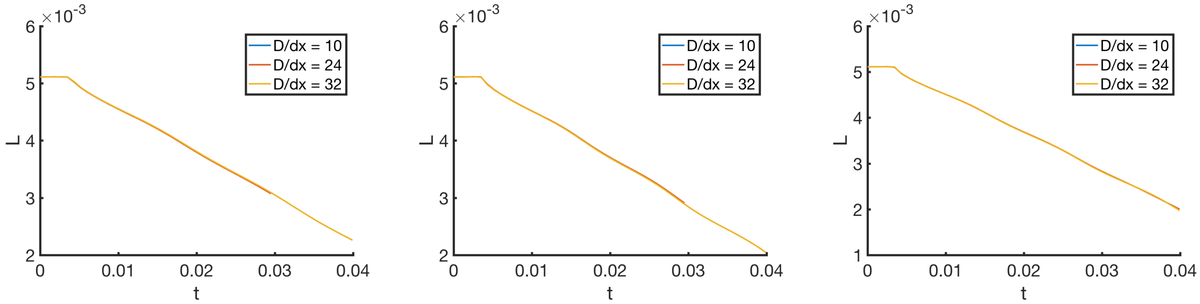

(a) α-based

(b) $\hat{\alpha}$-based

(c) ϕ-based

Figure 3.14: The length of the liquid column is presented as a function of time for the different methods. In each of the plots data from three different grid resolutions is presented. All data is in SI units.

from the diffused-α based method and the ϕ-based method are almost identical, and are slightly different from the α-based computation. This is evident from Fig. 3.13 as well.

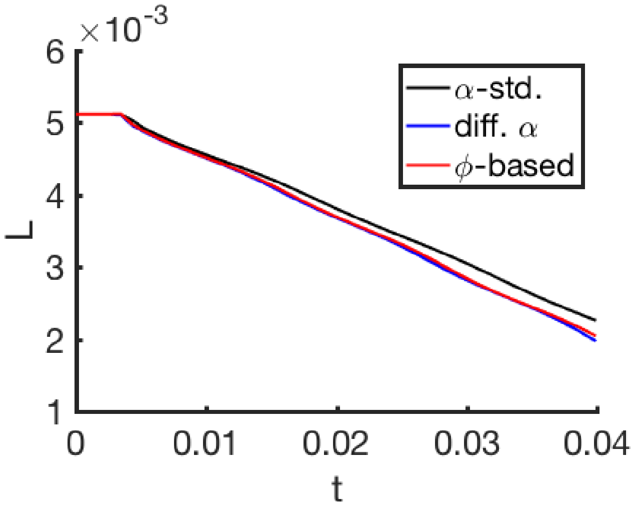

Figure 3.15: The time evolution of the column lengths for the finest cases from all three methods are presented. All data is in SI units.

For this test we do not have any quantitative experimental or theoretical benchmarking data. Here, we only compare the results from the three methods against each other. While subtle differences emerge in the shapes of the bulbs and the lengths of the liquid columns from the three methods, the differences in the overall dynamics appear minor. An improved curvature scheme does not impact the results in a significant way.

3.3.6 Co-Flow Atomization

Here we look at a full atomization problem. The physical setup consists of a water jet injected through a cylindrical nozzle of diameter D, surrounded by a co-flowing streaming of air. This test has been discussed in experimental [24] and computational [21, 69] work in literature.

The speed of the liquid is set at $U_l = 1.4\text{ms}^{-1}$, and the gas speed is varied to give varying relative speeds $U_{rel.} = U_g - U_l$. The key non-dimensional number here is the Weber number, $We = \frac{\rho_l D U_{rel.}}{\sigma}$. Here we consider four cases with $We = 26, 50, 100$ and 126. In all these cases $D/\Delta x = 28$ is used in the near field of the liquid jet to allow sufficient grid convergence.

In this test we consider the length of the intact liquid core, similar to the tests seen earlier in Section 2.2.4. The intact liquid core lengths are presented in Fig. 3.16 as a function of time for the cases considered here.

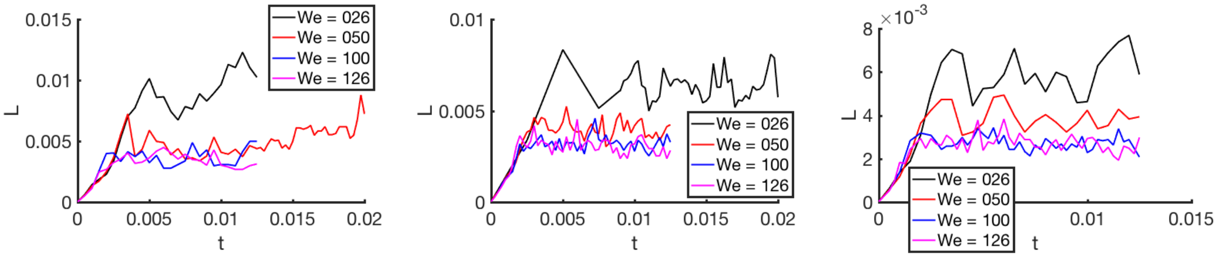

(a) α-based (b) $\hat{\alpha}$-based (c) ϕ-based

Figure 3.16: The length of the intact liquid core is presented as a function of time for the co-flow atomization cases. All data is in SI units.

For all the cases a few common observations can be made. First, the lengths of the liquid core increases linearly at first and then the lengths start fluctuating once atomization commences. The other observation is that as the We increases, the intact liquid length reduces. The simulations are run till the length data is statistically steady, i.e., the moving average of the data becomes constant. For some of the cases here with low We values, i.e., longer intact liquid lengths, the simulations are run for a longer time duration to ensure this convergence.

The mean length values for the three methods are presented in Fig. 3.17 along with some other benchmarking data. The experimental fit of Eroglu et al. [24] is presented with a dotted line. Computational data by Deshpande et al.[21] and Trujillo et al.[69], that employs the α-based method is also presented.

Broadly, the present computational results from the three methods agree fairly well with the experimental and computational results from literature, especially for the higher We cases. For the lower We cases, the differences in the data start appearing with the α-based method outperforming the other methods. The results from the diffused α-based method and the ϕ-based method are in close agreement throughout.

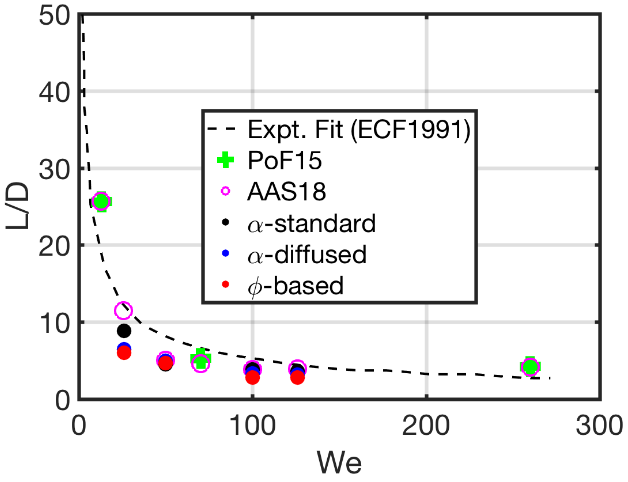

Figure 3.17: The mean value of the liquid core lengths as a function of We for the three methods along with computational and experimental benchmarking data. The legend entry ECF1991 refers to the experimental fit of Eroglu et al. [24], PoF15 refers to computational data by Deshpande et al. [21] and AAS18 refers to data by Trujillo et al. [69].

3.4 Conclusions

The work in this chapter is a first step towards evaluating different curvature schemes for realistic atomization-relevant problems, and assessing the importance of curvature schemes in atomization-type problems. In the first part we describe three viable curvature schemes and their implementation in the `interFoam` solver. A novel method for constructing a signed distance function for an arbitrary interface in the Volume-of-Fluid framework was also presented.

The results from the test cases are summarized in Table 3.1. In the 2D droplet test case a clear difference in the performance of the different schemes was noted. We observe a strong $O(\Delta x^2)$ convergence for the ϕ-based scheme, a weaker convergence trend for the $\tilde{\alpha}$ scheme and no convergence for the standard α-based scheme. In the 3D oscillating droplet test, we find that all the methods show a $O(\Delta x^1)$ convergence, but the error magnitude from the ϕ-based scheme is lower. In the Rayleigh breakup of the liquid column all the three methods perform fairly well with respect to the droplet sizes. The ϕ-based scheme, however, slightly outperforms the other two. In the shear-

Table 3.1: Summary of the curvature tests presented in Section 3.3

2D Circle (Section 3.3.1)	Very different performance across 3 methods: ϕ-based - 2^{nd} order, α - no convergence
3D Oscillating Droplet (Section 3.3.2)	ϕ-based clearly outperforms other methods; 1^{st} order performance across the 3 methods
Rayleigh Breakup (Section 3.3.3)	ϕ-based slightly outperforms other methods
Shear Layer (Section 3.3.4)	ϕ-based slightly outperforms other methods in some cases, rest of cases have similar performance
Liquid Column Retraction (Section 3.3.5)	Similar performance. Some qualitative differences in shape of bulb.
Co-Flow Atomization (Section 3.3.6)	Similar performance across methods for a range of We

layer test, the ϕ-based method slightly outperforms the other methods in some of the cases. The methods exhibit almost identical performance in most cases. In the liquid column retraction test, the performance is similar across the methods with some small qualitative differences in the shape of the resulting ligament and bulb. In the final atomization test, we find that results are identical across the methods for the high We cases, and in the small We cases, the standard α-based method shows a slightly better result as compared to the other schemes.

Overall, we see that in canonical test cases, which are completely surface tension dominated the performance of the methods is starkly different. However, as we add complexity in the tests in the form of complex interfaces, and forces like inertia and viscosity the differences in dynamics across the schemes become quite minor. A takeaway from the current work is that adding significant complexity in the curvature schemes may not lead to meaningful improvements in realistic flow simulations.

A potential next step in the work is to make the implementation of the schemes even more robust to be able to accommodate irregular cell shapes, and continue testing the schemes in more extreme flows like engine-relevant sprays.

Bibliography

[1] Openfoam user guide, the open source CFD toolbox user guide, version 1.5. openCFD limited. 2008.

[2] N Abani, S Kokjohn, SW Park, M Bergin, A Munnannur, W Ning, Y Sun, and Rolf D Reitz. An improved spray model for reducing numerical parameter dependencies in diesel engine CFD simulations. Technical report, SAE Technical Paper, 2008.

[3] Arpit Agarwal and Mario F Trujillo. A closer look at linear stability theory in modeling spray atomization. International Journal of Multiphase Flow, 109:1–13, 2018.

[4] Arpit Agarwal and Mario F Trujillo. The effect of nozzle internal flow on spray atomization. International Journal of Engine Research, 21(1):55–72, 2020.

[5] Lakshman Anumolu and Mario F Trujillo. Gradient augmented reinitialization scheme for the level set method. International Journal for Numerical Methods in Fluids, 73(12):1011–1041, 2013.

[6] Lakshman Anumolu and Mario F Trujillo. Gradient augmented level set method for phase change simulations. Journal of Computational Physics, 353:377–406, 2018.

[7] Marco Arienti and M Sussman. An embedded level set method for sharp-interface multiphase simulations of diesel injectors. International Journal of Multiphase Flow, 59:1–14, 2014.

[8] Marco Arienti and Mark Sussman. A high-fidelity study of high-pressure diesel injection. Technical report, SAE Technical Paper, 2015.

[9] Marco Arienti and Mark Sussman. A numerical study of the thermal transient in high-pressure diesel injection. International Journal of Multiphase Flow, 88:205–221, 2017.

[10] Jennifer C Beale and Rolf D Reitz. Modeling spray atomization with the Kelvin-Helmholtz/Rayleigh-Taylor hybrid model. Atomization and Sprays, 9(6), 1999.

[11] F Ben Rayana. Étude des instabilités interfaciales liquide-gaz en atomisation assistée et tailles de gouttes. PhD Thesis Institute National Polytechnique de Grenoble, 2007.

[12] Mathis Bode, Felix Diewald, David Oliver Broll, Jan Felix Heyse, Vincent Le Chenadec, and Heinz Pitsch. Influence of the injector geometry on primary breakup in diesel injector systems. Technical report, SAE Technical Paper, 2014.

[13] JU Brackbill, Douglas B Kothe, and Charles Zemach. A continuum method for modeling surface tension. Journal of Computational Physics, 100(2):335–354, 1992.

[14] Zheng Chen, Zhenkuo Wu, Jingping Liu, and Chiafon Lee. Combustion and emissions characteristics of high n-butanol/diesel ratio blend in a heavy-duty diesel engine and EGR impact. Energy Conversion and Management, 78:787–795, 2014.

[15] Mohamed Chouak, Alexandre Mousseau, Damien Reveillon, Louis Dufresne, and Patrice Seers. Study of transient effects in the internal flow of a diesel fuel injector. Technical report, SAE Technical Paper, 2015.

[16] Flavio DF Chuahy and Sage L Kokjohn. Effects of the direct-injected fuel's physical and chemical properties on dual-fuel combustion. Fuel, 2017.

[17] Cyril Crua, Morgan R Heikal, and Martin R Gold. Microscopic imaging of the initial stage of diesel spray formation. Fuel, 157:140–150, 2015.

[18] Sharen J Cummins, Marianne M Francois, and Douglas B Kothe. Estimating curvature from volume fractions. Computers & structures, 83(6-7):425–434, 2005.

[19] JM Desantes, JM García-Oliver, JM Pastor, A Pandal, E Baldwin, and DP Schmidt. Coupled/decoupled spray simulation comparison of the ECN spray A condition with the Σ-Y eulerian atomization model. International Journal of Multiphase Flow, 80:89–99, 2016.

[20] Suraj S Deshpande, Lakshman Anumolu, and Mario F Trujillo. Evaluating the performance of the two-phase flow solver interfoam. Computational Science & Discovery, 5(1):014016, 2012.

[21] Suraj S Deshpande, Soumil R Gurjar, and Mario F Trujillo. A computational study of an atomizing liquid sheet. Physics of Fluids, 27(8):082108, 2015.

[22] Olivier Desjardins, Jeremy McCaslin, Mark Owkes, and Peter Brady. Direct numerical and large-eddy simulation of primary atomization in complex geometries. Atomization and Sprays, 23(11), 2013.

[23] Philip G Drazin and William Hill Reid. Hydrodynamic Stability. Cambridge university press, 2004.

[24] Hasan Eroglu, Norman Chigier, and Zoltan Farago. Coaxial atomizer liquid intact lengths. Physics of Fluids A: Fluid Dynamics, 3(2):303–308, 1991.

[25] Marianne M Francois, Sharen J Cummins, Edward D Dendy, Douglas B Kothe, James M Sicilian, and Matthew W Williams. A balanced-force algorithm for continuous and sharp interfacial surface tension models within a volume tracking framework. Journal of Computational Physics, 213(1):141–173, 2006.

[26] M Ghiji, L Goldsworthy, PA Brandner, V Garaniya, and P Hield. Analysis of diesel spray dynamics using a compressible Eulerian/VOF/LES model and microscopic shadowgraphy. Fuel, 188:352–366, 2017.

[27] Mikhael Gorokhovski and Marcus Herrmann. Modeling primary atomization. Annu. Rev. Fluid Mech., 40:343–366, 2008.

[28] S Hysing. A new implicit surface tension implementation for interfacial flows. International Journal for Numerical Methods in Fluids, 51(6):659–672, 2006.

[29] Raad I Issa. Solution of the implicitly discretised fluid flow equations by operator-splitting. Journal of Computational Physics, 62(1):40–65, 1986.

[30] D. Jarrahbashi and W.A. Sirignano. Vorticity dynamics for transient high-pressure liquid injection. Physics of Fluids, 26(101304):1–52, 2014.

[31] Daokuan Jiao, Fan Zhang, Qing Du, Zhiqiang Niu, and Kui Jiao. Direct numerical simulation of near nozzle diesel jet evolution with full temporal-spatial turbulence inlet profile. Fuel, 207:22–32, 2017.

[32] A Kastengren, J Ilavsky, Juan Pablo Viera, Raul Payri, DJ Duke, A Swantek, F Zak Tilocco, N Sovis, and CF Powell. Measurements of droplet size in shear-driven atomization using ultra-small angle X-ray scattering. International Journal of Multiphase Flow, 92:131–139, 2017.

[33] AL Kastengren, CF Powell, T Riedel, S-K Cheong, K-S Im, Xin Liu, YJ Wang, and J Wang. Nozzle geometry and injection duration effects on diesel sprays measured by x-ray radiography. Journal of Fluids Engineering, 130(4):041301, 2008.

[34] Alan L Kastengren, F Zak Tilocco, Daniel J Duke, Christopher F Powell, Xusheng Zhang, and Seoksu Moon. Time-resolved x-ray radiography of sprays from engine combustion network spray a diesel injectors. Atomization and Sprays, 24(3), 2014.

[35] Alan L Kastengren, F Zak Tilocco, Christopher F Powell, Julien Manin, Lyle M Pickett, Raul Payri, Tim Bazyn, et al. Engine combustion network (ECN): measurements of nozzle geometry and hydraulic behavior. Atomization and Sprays, 22(12):1011–1052, 2012.

[36] Chaitanya Kavuri and Sage L Kokjohn. Computational optimization of a reactivity controlled compression ignition (RCCI) combustion system considering performance at multiple modes simultaneously. Fuel, 2017.

[37] Pierre Lafrance. Nonlinear breakup of a laminar liquid jet. The Physics of Fluids, 18(4):428–432, 1975.

[38] Horace Lamb. Hydrodynamics. University Press, 1924.

[39] Romain Lebas, Thibault Menard, Pierre-Arnaud Beau, Alain Berlemont, and François-Xavier Demoulin. Numerical simulation of primary break-up and atomization: Dns and modelling study. International Journal of Multiphase Flow, 35(3):247–260, 2009.

[40] Won Geun Lee and Rolf D Reitz. A numerical investigation of transient flow and cavitation within minisac and valve-covered orifice diesel injector nozzles. Journal of Engineering for Gas Turbines and Power, 132(5):052802, 2010.

[41] Arthur H Lefebvre and Vincent G McDonell. Atomization and Sprays. CRC press, 2017.

[42] SP Lin and RD Reitz. Drop and spray formation from a liquid jet. Annual Review of Fluid Mechanics, 30(1):85–105, 1998.

[43] Philippe Marmottant and Emmanuel Villermaux. On spray formation. Journal of fluid mechanics, 498:73–111, 2004.

[44] JM Martinez, X Chesneau, and B Zeghmati. A new curvature technique calculation for surface tension contribution in plic-vof method. Computational Mechanics, 37(2):182–193, 2006.

[45] MJ McCarthy and NA Molloy. Review of stability of liquid jets and the influence of nozzle design. The Chemical Engineering Journal, 7(1):1–20, 1974.

[46] Balaji Mohan, Wenming Yang, and Siaw kiang Chou. Development of an accurate cavitation coupled spray model for diesel engine simulation. Energy Conversion and Management, 77:269–277, 2014.

[47] Seoksu Moon, Yuan Gao, Jin Wang, Kamel Fezzaa, and Taku Tsujimura. Near-field dynamics of high-speed diesel sprays: Effects of orifice inlet geometry and injection pressure. Fuel, 133:299–309, 2014.

[48] Joseph Oefelein, Rainer Dahms, and Guilhem Lacaze. Detailed modeling and simulation of high-pressure fuel injection processes in diesel engines. SAE International Journal of Engines, 5(3):1410–1419, 2012.

[49] Mark Owkes, Eric Cauble, Jacob Senecal, and Robert A Currie. Importance of curvature evaluation scale for predictive simulations of dynamic gas–liquid interfaces. Journal of Computational Physics, 365:37–55, 2018.

[50] Mark Owkes and Olivier Desjardins. A mesh-decoupled height function method for computing interface curvature. Journal of Computational Physics, 281:285–300, 2015.

[51] HV Patel, JAM Kuipers, and EAJF Peters. Computing interface curvature from volume fractions: A hybrid approach. Computers & Fluids, 161:74–88, 2018.

[52] R Payri, J Gimeno, J Cuisano, and Javier Arco. Hydraulic characterization of diesel engine single-hole injectors. Fuel, 180:357–366, 2016.

[53] Lyle M Pickett, Julien Manin, Alan Kastengren, and Christopher Powell. Comparison of near-field structure and growth of a diesel spray using light-based optical microscopy and x-ray radiography. SAE International Journal of Engines, 7(2):1044–1053, 2014.

[54] Stéphane Popinet. An accurate adaptive solver for surface-tension-driven interfacial flows. Journal of Computational Physics, 228(16):5838–5866, 2009.

[55] Stéphane Popinet. Numerical models of surface tension. Annual Review of Fluid Mechanics, 50:49–75, 2018.

[56] Lord Rayleigh. On the instability of jets. Proceedings of the London mathematical society, 1(1):4–13, 1878.

[57] Rolf Reitz. Modeling atomization processes in high-pressure vaporizing sprays. Atomisation and Spray Technology, 3(4):309–337, 1987.

[58] Rolf Reitz, Lyle Pickett, and Mario Trujillo. Fuel introduction. Encyclopedia of Automotive Engineering, 2014.

[59] Henrik Rusche. Computational fluid dynamics of dispersed two-phase flows at high phase fractions. PhD dissertation, Imperial College London (University of London), 2003.

[60] Douglas Thomas Ryddner. Advection of a Reconstructed aVoF Method with Phase Change. PhD thesis, University of Wisconsin - Madison, 2018.

[61] FJ Salvador, Jorge Martínez-López, M Caballer, and C De Alfonso. Study of the influence of the needle lift on the internal flow and cavitation phenomenon in diesel injector nozzles by CFD using RANS methods. Energy conversion and management, 66:246–256, 2013.

[62] Francisco Javier Salvador, Jaime Gimeno, José Manuel Pastor, and Pedro Martí-Aldaraví. Effect of turbulence model and inlet boundary condition on the diesel spray behavior simulated by an Eulerian Spray Atomization (ESA) model. International Journal of Multiphase Flow, 65:108–116, 2014.

[63] Peter J Schmid and Dan S Henningson. Stability and transition in shear flows, volume 142. Springer Science & Business Media, 2012.

[64] David P Schmidt and ML Corradini. The internal flow of diesel fuel injector nozzles: a review. International Journal of Engine Research, 2(1):1–22, 2001.

[65] J Shinjo and A Umemura. Simulation of liquid jet primary breakup: dynamics of ligament and droplet formation. International Journal of Multiphase Flow, 36(7):513–532, 2010.

[66] J Shinjo and A Umemura. Detailed simulation of primary atomization mechanisms in diesel jet sprays (isolated identification of liquid jet tip effects). Proceedings of the Combustion Institute, 33(2):2089–2097, 2011.

[67] J Shinjo and A Umemura. Surface instability and primary atomization characteristics of straight liquid jet sprays. International Journal of Multiphase Flow, 37(10):1294–1304, 2011.

[68] S Som and Suresh K Aggarwal. Effects of primary breakup modeling on spray and combustion characteristics of compression ignition engines. Combustion and Flame, 157(6):1179–1193, 2010.

[69] Mario F Trujillo, Soumil Gurjar, Michael Mason, and Arpit Agarwal. Global characterization of the spray formation process. Atomization and Sprays, 28(9), 2018.

[70] O Ubbink and RI Issa. A method for capturing sharp fluid interfaces on arbitrary meshes. Journal of Computational Physics, 153(1):26–50, 1999.

[71] Akira Umemura. Self-destabilizing mechanism of a laminar inviscid liquid jet issuing from a circular nozzle. Physical Review E, 83(4):046307, 2011.

[72] Kurian J Vachaparambil and Kristian Etienne Einarsrud. Comparison of surface tension models for the volume of fluid method. Processes, 7(8):542, 2019.

[73] Bram Van Leer. Towards the ultimate conservative difference scheme. ii. monotonicity and conservation combined in a second-order scheme. Journal of Computational Physics, 14(4):361–370, 1974.

[74] Hu Wang, Rolf Deneys Reitz, Mingfa Yao, Binbin Yang, Qi Jiao, and Lu Qiu. Development of an n-heptane-n-butanol-pah mechanism and its application for combustion and soot prediction. Combustion and Flame, 160(3):504–519, 2013.

[75] Everett A Wenzel and Sean C Garrick. Finite particle methods for computing interfacial curvature in volume of fluid simulations. Atomization and Sprays, 28(2), 2018.

[76] Q Xue, M Battistoni, CF Powell, DE Longman, SP Quan, E Pomraning, PK Senecal, DP Schmidt, and S Som. An eulerian CFD model and x-ray radiography for coupled nozzle flow and spray in internal combustion engines. International Journal of Multiphase Flow, 70:77–88, 2015.

[77] Binbin Yang, Mingfa Yao, Wai K Cheng, Yu Li, Zunqing Zheng, and Shanju Li. Experimental and numerical study on different dual-fuel combustion modes fuelled with gasoline and diesel. Applied Energy, 113:722–733, 2014.

[78] A. Zandian, W.A Sirignano, and F. Hussain. Planar liquid jet: Early deformation and atomization cascades. Physics of Fluids, 29(062109):1–20, 2017.